SONDERPUBLIKATION

Nr. 004

Feasability of high frequency multibeam snippet backscatter ammunition detection and evaluation of their position accuracy

Tina Kunde

DHyG-Sonderpublikation
Nr. 004
November 2021

Herausgeber:
Deutsche Hydrographische Gesellschaft e. V. (DHyG)

DOI: 10.23784/DHyG-SP_004

DHyG-SONDERPUBLIKATION

Nr. 004

Feasability of high frequency multibeam snippet backscatter ammunition detection and evaluation of their position accuracy

Tina Kunde

Contents

List of Figures

List of Tables

List of Abbreviations

ARA	Angle vs. Range Analysis
ARTK	Advanced Real Time Kinematic
AUV	Autonomous Underwater Vehicle
AVG	Angle Varying Gain
BAAINBw	Federal Office Bundeswehr Equipment, Information Technology and In-Service Support
BALTEX	Baltic Sea Experiment
CEP	Circular Error Probable
CTD	Conductivity, Temperature, and Depth
DGNSS	Differential Global Navigation Satellite System
DTM	Digital Terrain Model
ETRS89	European Terrestrial Reference System 1989
GNSS	Global Navigation Satellite System
GPS	Global Positioning System
GRS80	Geodetic Reference System 1980
HDOP	Horizontal Dilution of Precision
IHO	International Hydrographic Organization
IMU	Inertial Measurement Unit
INS	Inertial Navigation System
MBES	Multibeam Echosounder
MELUR	Ministry of Energy, Agriculture, the Environment ans Rural Areas
NHN	Normal Height Null
PDOP	Positional Dilution of Precision
RINEX	Receiver Independant Exchange Format
RV	Research Vessel
SAPOS	Satellite Positioning Service
SAS	Synthetic Aperture Sonar
SBES	Singlebeam Echosounder
SBP	Sub-bottom Profiler
SIS	Seafloor Information System

SSS	Sidescan Sonar
SVP	Sound Velocity Profile
TPU	Total Propagated Uncertainty
TVG	Time Varying Gain
WGS84	World Geodetic System 1984
WSA	Waterways and Shipping Administration
WTD71	Bundeswehr Technical Center for Ships ans Naval Weapons, Maritime Technology and Research

The important facts in brief

With the end of the Second World War in 1945, the German coastal waters became a large dumping ground for various warfare agents. Even if designated areas were established for the disposal of the ammunition bodies, the dumping processes itself were unsupervised. As a result, the shallow coastal areas of the Baltic Sea and also some parts of the North Sea are highly contaminated with different kind of ammunition which poses a hazard both for the economic development and the responsible ecological interactions.

Within the present baseline study conducted in the area Kolberger Heide in the Bay of Kiel, snippet backscatter information gathered with the high frequency MBES EM 2040C from Kongsberg Maritime AS are evaluated due to their usability to detect the mentioned ammunition bodies. In comparison to already implemented detection applications like towed sonar and magnetometer or AUVs equipped with high-resolution sonar instruments, the investigated technique has the advantage of using GNSS positioning to increase the attainable horizontal positioning accuracy. Especially with regard to cleaning strategies and the monitoring of the environmental health, this can be a promising prospective method applicable for research and practice.

The evaluation of the GNSS positioning information was done with a manufacturer specific software. Besides the actual data, also different sets of correction data provided by the German satellite positioning service SAPOS® were investigated to point out possibilities for increasing the accuracy of the horizontal position. The processing of the snippet backscatter information was performed using the software Fledermaus Geocoder 7.3.6 provided by QPS. For comparison, the Tactical Map administrated by the German Navy was consulted as a reference.

Already during the acquisition of data, the snippet backscatter information seems to be promising. These positive impressions are confirmed by the advancing evaluation, even if the quality of the created mosaic images provides the possibility for further improvements. It is possible to verify the detected suspicious objects using the official and therefore assumed to be trustworthy information of the Tactical Map. Comparing the location of the objects, an explicit deviation is detected which is caused by the improvable positioning technique. In that regard, the evaluation shows a significant improvement of the attainable accuracy when using DGNSS. Based on the results presented in this thesis, the vessel-based detection of dumped ammunition bodies can be assumed as a promising alternative for future tasks.

1 Introduction

Hydrography as a scientific discipline of Geomatics has a broad range of thematic fields concerning the earth's waters as Schiller (2012) has already pointed out. With regard to the rapid advancement in both ecology and economy, the aim of knowledge enhancement when dealing with all kind of waters is becoming increasingly important and hence the tasks covered by Hydrography do. The main duties as stated by the International Hydrographic Organization (subsequently referred to as IHO) (2009) can be summarized to the assurance of the safety of navigation and the support of all marine activities assigned to different subject areas such as economic developments and the environmental protection. In particular, the economic development of renewable energies and the utilization of water areas for offshore wind turbines and transoceanic cables is more and more moving to the center of public attention. However, construction processes have to be delayed repeatedly due to the unexpected detection of dumped ammunition bodies.

As explained in Böttcher et al. (2015), areas used for offshore wind turbines and subsequently related cable routes need to be examined in advance to preclude the occurrence of ammunition bodies. In case of the discovery of suspicious objects, private companies specified for the clearance of explosive ordnance have to be engaged. This approach required in accordance with the German Industrial Standard DIN 4020 is not just highly time-consuming, but also very cost-intensive as it can be seen in the case of the wind farm Riffgat and the related cable route supplied by TenneT TSO GmbH in the southern North Sea 15 km off the isle of Borkum. According to the official press release of February 11, 2014, almost 30 tons of old ammunition were detected and recovered within 18 month. Ammunition clearance and time delay entailed additional costs amounting to almost 100 million Euro[1] which was only just below the project expenses (TenneT TSO GmbH, 2014).

Dumped ammunition bodies effect not only construction projects as described previously. Due to their mostly toxic constituents and the progressive corrosion of the outer sheath, they represent a high ecological risk for the marine life. The individual components such as white phosphorus, gun cotton, or sulphur yperite can poison fish and mussel farms which will affect the fishery industry. As confirmed by laboratory tests conducted within the CHEMSEA[2]

[1] The distribution of the additional costs amounts to 57 million Euro for the clean-up operations and 43 million Euro for compensation payments due to the delay (TenneT TSO GmbH, 2014).

[2] The three-year CHEMSEA project was funded by the European Union Baltic Sea Region Programme. Coordinated by the Polish Institute of Oceanology, the project covers the search and assessment of chemical munitions in the Baltic Sea to evolve guidelines and emergency plans for the handling of the mentioned chemical warfare ammunition (Böttcher et al., 2015).

project, specific degradation products were proven in codfish and for the first time it was evinced that mussels are able to absorb and accumulate these degradation products (Böttcher et al., 2015). Furthermore, the constituents can be washed up to the coasts and cause serious accidents. Year after year, white phosphorus causes severe burns on the Baltic beaches due to a confusion with amber[3] (Böttcher et al., 2011).

Up to now, the localization of possible ammunition bodies was performed by using high resolution sidescan or synthetic aperture sonars (subsequently referred to as SSS respectively SAS) or magnetometer systems. Due to the fact, that the dumped ammunition bodies are spatially distributed over large areas, both SSS and SAS are mounted preferentially on autonomous underwater vehicles (subsequently referred to as AUV) which can operate in variable depth. However, the usage as a towed device or mounted on an AUV does not affect the associated costs and complexity which are accompanied by both variants. In addition, the two mentioned methods require complex underwater positioning solutions and suffer, in comparison to a direct position determination using the global navigation satellite system (subsequently referred to as GNSS), from an improvable horizontal positioning accuracy. With the increasing improvement of multibeam echosounder (subsequently referred to as MBES) systems during the last years, the simultaneously gathered snippet backscatter information may offer a new possibility for precisely horizontal positioned ammunition detection in shallow coastal areas.

1.1 Objectives

The aim of the baseline study regarded in this thesis is to analyze high frequency MBES bathymetric data with a special focus on snippet backscatter information due to their usability to detect ammunition bodies of different sizes. In the course of this analysis, the attainable horizontal positioning accuracy using different GNSS solutions is compared to give evidence of possible accuracy increases. The area Kolberger Heide in the Bay of Kiel is served as a case study for this work as there is an existing ammunition dumping site designated by the German Navy which is under discussion to be enlarged.
To provide a general overview, a characterization of the considered area is given. This includes the formation processes of the Baltic Sea basin as well as the prevailing geological conditions within the study site to indicate particularities which should be implied to the data processing. In addition, the historical wartime events are introduced as the necessity of

[3]Some incidents are documented in Böttcher et al. (2015) or in appropriate media reports which can be viewed at `http://www.schleswig-holstein.de/DE/UXO/Strandfunde/_documents/strand_Phosphor.html`.

these kind of investigations is justified in these incidents. To illustrate the distinctive role of the considered marine area, an insight to the historical events that occurred especially during and after the Second World War is given.

In the second chapter of this thesis, the basic principles this work is referring to, are pointed out. Besides an oceanographic introduction, the general procedure of GNSS positioning for a vessel in motion is presented as a basis for the later on post-processing. Last but not least, a general introduction to the topic of underwater acoustics is given including the fundamental functionality of a MBES and the theory of snippet backscatter data is explained. In conclusion, the principle of sub-bottom profiling is briefly introduced.

Since a set of data collected during the research cruise AL447 forms the basis for this work, the third chapter introduces the systems which were installed on RV ALKOR for acquisition purposes. Preceding the description of the hydrographic instruments, an overview of the geographical extend of the investigated area is given. Of special importance for the quality of the gathered data is the calibration of the inertial navigation system (subsequently referred to as INS) and the MBES prior to the beginning of the survey. For this purpose, the calibration procedures for both systems and their results are explained further.

The evaluation of the data is structured in three thematic areas whereas the key focus lays on the hydrographic data processing. The consideration of the water level data collected by three tide gauge stations next to the observed area provides an additional oceanographic scope for further analysis. Apart from the evaluation of different arrangements of position data using a company-specific software solution, also the general post-processing procedure the conducted evaluation is based on is introduced. To achieve a positive result both for the bathymetry and the imagery data, the processing workflows and settings are introduced. The same applies to the evaluation of the seafloor sediments.

Before the consideration of the results and the formulation of an outlook is given, the processed data needs to be interpreted. The emphasis is on the analysis and comparison of the snippet backscatter imagery data with exemplary objects taken from the Tactical Map of the German Navy to highlight the requirements for ammunition detection using a high frequency MBES. Based on these results, a comparative analysis of alternative measuring methods as SAS, SSS, and magnetometer is made. Likewise, the assessment of the different GNSS solutions is part of the discussion. The interpretation of bathymetric data in connection with the seafloor sediments is performed as well to give evidence of the plausibility of sedimentation processes which may affect the ammunition bodies on the seafloor in the near future.

1.2 Characterization of the considered area

The study site Kolberger Heide is situated in the western Baltic Sea at the end of the Kiel Fjord off the coast of Schleswig-Holstein and is characterized by its shallow water with a depth range between 5 m up to 18 m. In comparison to the rest of the Baltic Sea, this part does not even exist for 400 years. Due to a storm surge at February 10, 1625, the former land area was flooded, declined, and is nowadays characterized by its shallow water depth (NABU Schleswig-Holstein, 2016). The area shows similar sedimentary characteristics as the adjacent coastal area, but this is not just caused by the sinking of the land mass.

According to Spielhagen (2012), the subsoil of the Baltic Sea consists of various sedimentary rocks, granites, and gneisses and is therefore more similar to the land surface then to the oceans. This is justified by the geological formation of the Baltic Sea basin. Three fundamental processes played a decisive role during this development. Besides eustatic sea level changes which are caused by global climatic changes, also isostatic sea level changes due to the discharge of continental land masses took place. Thirdly, waves and current activities led to sediment dynamic changes of the coast line (Lemke, 2005).

20,000 years before present, the Baltic Sea area was covered by an ice shield originating in Scandinavia which forged further ahead to the south. This moving Weichselian glacier caused the formation of the subsequent Baltic Sea basin. The loose material consisting of sediments and rocks were pushed forward up to the present eastern and southern part of the Baltic Sea. 12,000 years before present, the commencing global warming caused glacial melting which led to the formation of small melt water lakes. These lakes merged into the Baltic Ice Lake (Spielhagen, 2012). Within this fresh water lake, the sediment load of the glacier was deposited depending on the season which formed a layered structure of coarse and fine sediments (Leipe et al., 2011). Caused by the continuing global warming 10,300 years before present, the melting water drained into the Skagerrak by forming out a channel passing through Mid Sweden. This led to a rise of the North Sea water level which in turn used the connection to flow into the Baltic Ice Lake basin to form out the Yoldia Sea 300 years later (Spielhagen, 2012). The change from fresh to sea water also effected the density of the sediments by the charge of magnetic minerals (Leipe et al., 2011). The progressive eustatic sea level rise caused by the glacial melting induced the isostatic rise of Mid Sweden. 9,500 years before present, the channel connecting the North Sea with the Yoldia Sea was closed again and the brackish Ancylus Lake was formed from the former shelf sea. As the water level of the North Sea was still rising, the Ancylus Lake was washed up with sea water flowing in through the Kattegat. According to Lemke (2005), this influx led to a renewed intense transformation of the coast line. Caused by the constant rise of the continental areas due to eustatic processes and the increasing water level due to the influx of sea water coming from the North Sea and fresh water from merging rivers, the Ancylus Lake finally get brackish ans the Litorina Sea was formed. As well as all previous changes could be established in the sediments, the change to brackish water also influenced the layered structure which was fine grained due to a constant water density. This final stage of development occurred 8,000 years before present and is said to be the predecessor of the Baltic Sea in its actual shape and properties, even if the Litorina Sea probably consisted of more sea water than the Baltic Sea today (Leipe et al., 2011).

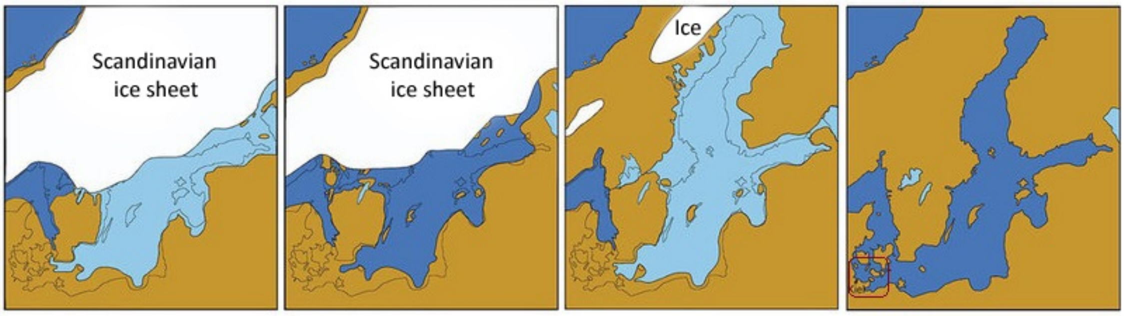

Figure 1.1: Formation phases of the Baltic Sea. Light blue surfaces indicate fresh, dark blue surfaces sea water. Development stages from left to right: Baltic Ice Lake, Yoldia Sea, Ancylus Lake, and Baltic Sea in its present shape. The red framed area indicates the study site (according to Spielhagen, 2011).

The individual stages of development as previously described are depicted in Figure 1.1 for a comprehensive review of the genesis. In conclusion, the present Baltic Sea is quite young in comparison to the oceans covering the earth surface, but nevertheless of great historical significance as introduced in the following section.

1.3 Historical background

In course of the Torstensson War between Sweden and Denmark in the 17th century, the area around the Kolberger Heide has been the scene of a naval battle between the fleets of both countries. 1644, only 19 years after the devastating storm surge and the flooding of the former land area, more than 70 vessels fought with cannons for the predominance in the western Baltic Sea (Robl Matzen, 2010).

In the following decades, the Baltic Sea acted as a theater of war again and again. Within the scope of residual ammunition, the time frame beginning in the 1870's is mostly important. Due to the constant technical progress, the established German Navy started to use grenades, torpedos, mines and other marine weapons for training purposes in specific military training areas. In the same time, the naval ports were secured by mines and permanently ordnance. Ammunition which was no longer in use was systematically dumped into the sea to render them unusable. Shortly before the beginning of the First World War, bombs were implemented to the warfare and, similar to the other ammunition which was no longer required, dumped into the sea ate the end of all military operations (Böttcher et al., 2011). During the First World War, a lot of mine barriers consisting of tethered or bottom mines were installed. After the war ended in 1918, the remaining barriers were cleared away. With the beginning of the Second World War in 1939, the old mine barriers were reactivated and reinstalled. In addition, warplanes start to drop bombs, missiles, naval mines, and gun ammunition into the sea (Böttcher et al., 2011). In total, 3,896 mines were dropped in the Kiel Bay[4] by the allies to block the sea routes as they were highly frequented. 119 of them missed their target and landed onshore, only 95 led to the damage or sinking of hostile vessels. For instance, the Royal Air Force dropped bottom mines along sea route which, apart from that, had to be kept free of mines (Böttcher et al., 2015).

Until the end of the Second World War, Schleswig-Holstein was the only territory which was not occupied by the allies. This special characteristic made it appealing for the German Armed Forces to transport all warfare ammunition out of their stocks to the intact harbors where they were loaded onto vessels and shipped to the fjords and bays to be systematically dumped into the sea. One of these officially determined dumping sites was the area of Kolberger Heide as indicated in Figure 1.2 and Figure 1.3. In order to prevent these ammunition transports, the allies used bombardments and mining operations to block rail and road networks as well as the sea routes. After Germany's surrender in May 1945, the occupying forces started to dump all of the captured ammunition to the sea to disable them. Just in the case study area Kolberger Heide, the inventories of a German naval arsenal comprising up to 8,000 torpedo heads and 10,000 naval mines of different types were dumped. The systematical dumping of the ammunition residuals was controlled by the allies, but nevertheless, some of the vessels start to throw the ammunition bodies overboard even before the Kolberger Heide dumping site was reached. All of the described dumping activities took place in the shallower coastal waters. Within the exclusive economic zone it was more uncommon to get rid of ammunition bodies due to the long and unsafe distance the vessels have to cover (Böttcher et al., 2015). The only exception was the disposal of chemical weapons which were predominantly dumped in offshore areas (Böttcher et al., 2011).

[4] The stated numbers refer to the period from April 11, 1940 to April 25, 1945 and are based on precious inquiries (Böttcher et al., 2015).

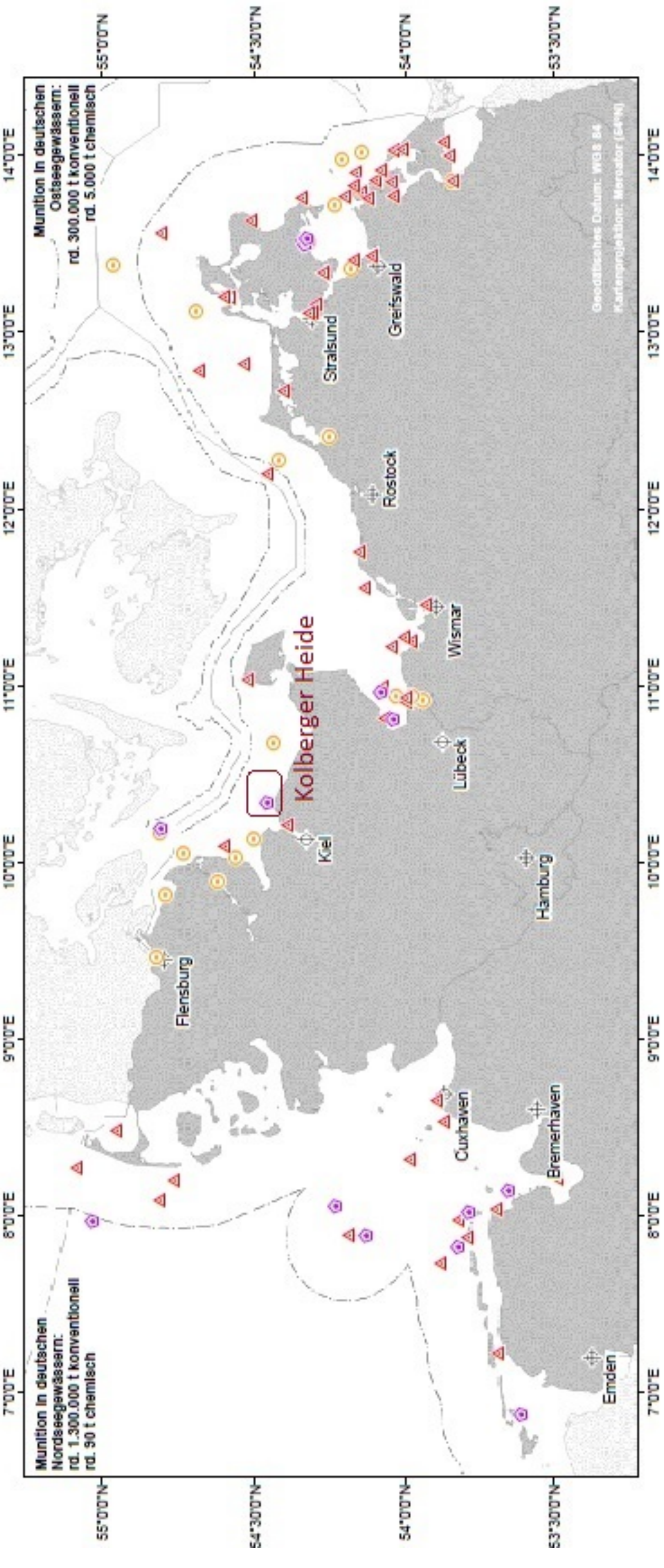

Figure 1.2: Simplified overview of contaminated areas in German marine waters. Magenta pentagon: ammunition dumping site, red triangle: contaminated area, yellow circle: potentially contaminated area. Continuous line: exclusive economic zone, dotdashed line: territorial sea boundary. Geographical data provided by `http://www.gadm.org`. The full size figure can be found in Appendix A (according to Böttcher et al., 2011).

These measures led to the present ammunition findings both in the North and in the Baltic Sea. Figure 1.2 provides a simplified overview of the contaminated areas in German marine waters, Figure 1.3 illustrates the contaminated areas in the Kiel Bay. The classification was done on the basis of historical information or contexts researched in the military archive in Freiburg. In the maps, a distinction between official dumping sites (magenta), contaminated areas (red), and potentially contaminated areas (yellow) is made. Some of these areas cover frequently used sea routes as the traffic separation scheme Kiel Lighthouse which is problematic with regard to possible ammunition displacements caused by trawl nets. This may lead to a difference between the documented and the present location of the ammunition bodies (Böttcher et al., 2015). However, the actual horizontal position is of great importance for hazard assessments and disposal operations as not all ammunition bodies are dumped without an intact ignator. This fact emphatically highlights the necessity and importance of the conducted baseline study.

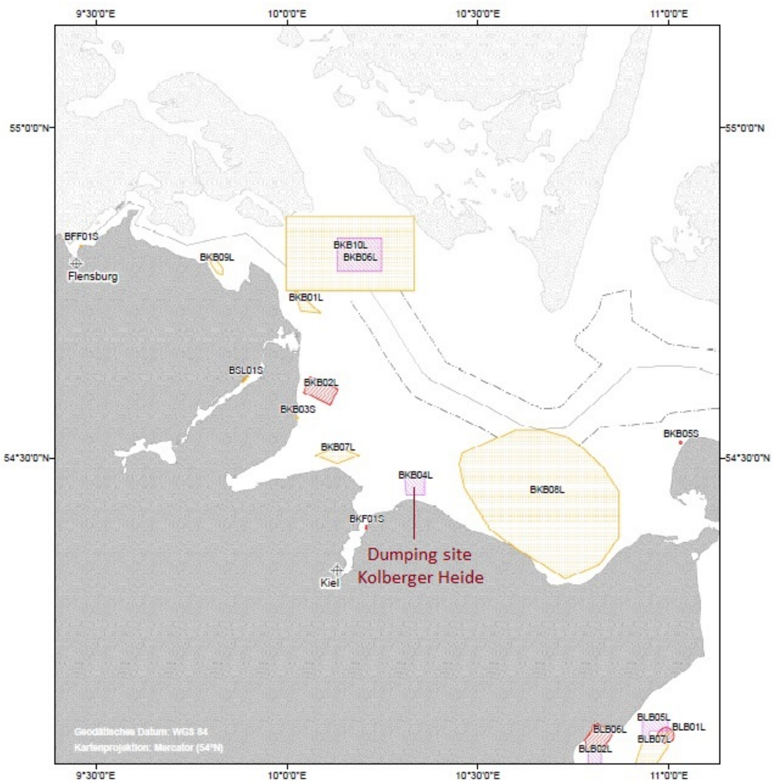

Figure 1.3: Simplified detail map of contaminated areas in the Kiel Bay. Magenta area: ammunition dumping site, red area: contaminated area, yellow area: potentially contaminated area. Continuous line: exclusive economic zone, dotdashed line: territorial sea boundary. Geographical data provided by `http://www.gadm.org`. The full size figure can be found in Appendix A (according to Böttcher et al., 2011).

2 Basic principles

With the beginning of the seafaring, the water masses which cover more than 70 percent of the earth's surface became subject of many explorations and the knowledge of water related processes grows. Along with the technical progress, complex instruments and techniques offered the possibility to increase the existing knowledge and to optimize existing working methods.

Alongside the principle of non-tidal water level changes, this chapter introduces the general method of GNSS positioning as well as selected underwater acoustic principles applied during this base study. The functionality of a MBES is introduced, subsequently leading to the theoretical foundations of snippet backscatter information. Lastly, the general principle of parametric sub-bottom profiling is explained.

2.1 Hydrophysic principle of standing waves

Long standing waves which occur in completely or partially closed basins like lakes, bays, or estuaries are called seiches. These free oscillations arise from the summation of two progressive waves which are traveling in opposite directions which leads to a periodic change in the water level (Open University, 1999). Seiches can be provoked by sudden changes in wind or air pressure and may lead to strong currents in the water column. Also existing tides can cause the occurrence or even resonance-induced amplification of seiches subject to the condition that the period of the tide coincides with the period of the seiche. But in general, the oscillations are damped which makes them badly verifiable (Seiß, 2015).

Figure 2.1 shows the idealized motion of a seiche in a completely closed and a partially closed basin. The point where the oscillating water is on par with the mean water level indicated by the dotted line is called node. Accordingly, the point where the water level reaches the minimum or maximum level is called antinode. As introduced, seiches may lead to currents in the water column. These are most powerful at the node positions where a horizontal motion of the water body occurs and accordingly weak at the antinodes where the water entirely moves in a vertical direction. The number of nodal points determines the mode of the eigen-oscillations in the basin. As it can be seen, the first order seiche with only one nodal point has a wavelength which relates to twice the length of the closed basin. The wavelengths describing the other displayed oscillation modes refer to the described one and amount to one half, one third, and one fourth of the origin wavelength.

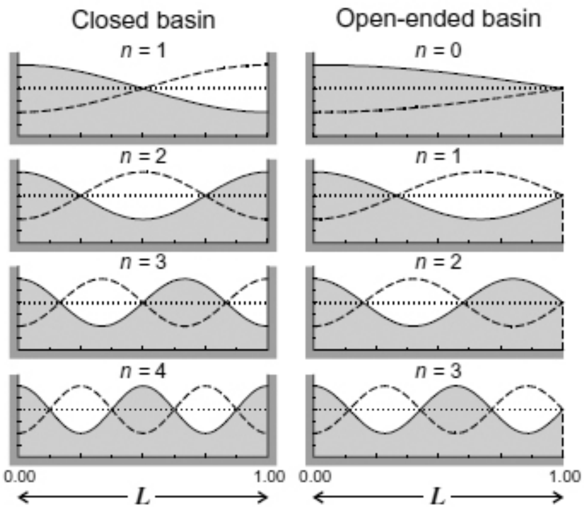

Figure 2.1: Surface profiles for the first four seiche modes in closed and open-ended rectangular basins of uniform depth (Rabinovich, 2009).

For the computation of the related period τ_n in a closed, rectangular basin of uniform depth, Merian's formula is used (Rabinovich, 2009):

$$\tau_n = \frac{2 \cdot L}{n \cdot \sqrt{g \cdot H}} \tag{2.1}$$

For partially closed basins, the wavelength of the first order seiche known as the Helmholtz mode equals four times the length of the basin. This is also expressed in the formula for the computation of the related period τ_n (Rabinovich, 2009):

$$\tau_n = \frac{4 \cdot L}{(2 \cdot n + 1) \cdot \sqrt{g \cdot H}} \tag{2.2}$$

The dimensions of the basin is given by the length L and the uniform depth H, both specified in meter. Additionally, the gravitational acceleration g given in ms^{-2} and the number of nodal points n is considered. Obviously, as indicated by Rabinovich (2009), the period of a seiche depends on the dimensions of the basin. Regarding the formulas 2.1 and 2.2, the following two relationships can be established:

- The longer the basin the longer the period of the seiche.
- The shallower the basin the longer the period of the seiche.

The Baltic Sea is one of the largest sea area with occurring seiches. The period of different oscillations was calculated independently by several experts. As stated in Magaard (1974), it is possible to distinguish between two oscillation systems with high wavelengths. The first one reaches from the western Baltic sea to the Gulf of Finland, the second one describes the seiche movement between the western Baltic Sea and the Gulf of Bothnia.

Table 2.1: Period of Baltic Sea first to third order seiches. Values base on calculations performed by Neumann (1941) as well as Krauss and Magaard (1962) (Magaard, 1974).

Oscillation system	1st order [h]	2nd order [h]	3rd order [h]
Western Baltic Sea – Gulf of Finland	27.4	19.1	13.0
Western Baltic Sea – Gulf of Bothnia	39.4	22.5	17.9

Table 2.1 provides an overview of the first to third order seiches of both oscillation systems. The amplitude of these Baltic Sea seiches may amount up to one meter which leads to a decay time of four periods (Magaard, 1974). Besides these two main standing waves, also seiches with shorter periods appear in the neighboring Bodden and Fjords, but as they have only a small amplitude which mismatches with the one of wind and air pressure, their propagation is not supported (Seiß, 2015).

2.2 Principle of GNSS positioning

The determination of the actual position of moving vehicles both on land and sea can be concluded as the main objective of tracking as a branch of navigation. For these tracking purposes, a system is needed which is fully available, reliable, and comparatively easy to use. 1973, the US armed forces invented such a system known as the global positioning system (subsequently referred to as GPS). Following this path, the usage of satellite systems summarized under the term of GNSS, has grown over the last years and became a great convenience within the scope of aids to navigation, especially for vessels offshore (Bauer, 2011).

All common GNSS[5] are using the same architecture and basic principles for localization as the pioneer GPS. These mentioned principles can be divided into absolute positioning which is also known as stand-alone GNSS, and relative positioning containing differential GNSS (subsequently referred to as DGNSS), but both of them require at least four satellites for determining a position (Bauer, 2011).

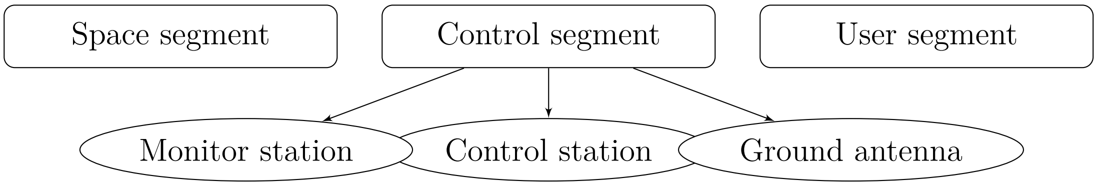

Figure 2.2: GNSS architecture. Classification of the system components space segment, user segment, and control segment which can be subdivided into monitor station, control station, and ground antenna (based on Misra and Enge, 2012).

Each GNSS consists of three components as displayed in Figure 2.2. The space segment comprises the satellite constellation. All available satellites are organized in a baseline constellation structured in accordance with the criteria stated by Hartl and Thiel (1984). Thus, it should be considered that the orbit is inclined and as high as possible. Furthermore, an even distribution of satellites arranged on symmetric orbits should be strove. The control segment provides a continuous monitoring of the GNSS satellites in the space segment and is in turn divided into three stations. The monitor station collects all measured values of the satellites[6] and forwards them to the control station which itself analyzes the measured values to predict the ephemerides and clock parameters. These computed data are transmitted back to the satellites by a ground antenna. The last segment contains all civil and military GNSS users which are able to receive the satellite signals including the GNSS time to compute the current position and velocity (Bauer, 2011, Misra and Enge, 2012).

For absolute positioning, the receiver uses a time shift to compute the pseudo range to at least four satellites. When the satellites send a sequence of signals, the receiver internally creates a similar sequence of signals within a similar time scale. This approach implies a receiver clock error Δt which has to be taken into account for calculating the actual distances to the corresponding satellites. The needed transmission time ΔT was measured by

[5] GPS (United States), GLONASS (Russian Federation), COMPASS which is also known as Beidou (People's Republic of China), and the European Galileo satellite system (Bauer, 2011).

[6] Measured values transmitted by the satellite are pseudo range, carrier phase and the Doppler phase shift (Bauer, 2011).

the receiver which afterwards computes the pseudo ranges S_P using formula 2.3 and the actual distances S using formula 2.4. In both computations, the propagation speed ν of the transmitted signals in the atmosphere has to be taken into account (Bauer, 2011):

$$S_{\mathsf{P}} = \Delta T \cdot \nu \tag{2.3}$$

$$S = (\Delta T + \Delta t) \cdot \nu \tag{2.4}$$

To determine the position consisting of a vertical and a horizontal component of the receiver, the actual distance towards each satellite and and its coordinates have to be known. The coordinates are part of the measured values the satellite transmits, the distance can be computed using formula 2.4. Using the Pythagorean theorem in a spatial form, the following equation system can be set up according to Bauer (2011):

$$(\begin{pmatrix} \Delta T_1 \\ \Delta T_2 \\ \Delta T_3 \\ \Delta T_4 \end{pmatrix} \cdot \nu + \Delta t \cdot \nu)^2 = (\begin{pmatrix} X_1 \\ X_2 \\ X_3 \\ X_4 \end{pmatrix} - X_{\mathsf{E}})^2 + (\begin{pmatrix} Y_1 \\ Y_2 \\ Y_3 \\ Y_4 \end{pmatrix} - Y_{\mathsf{E}})^2 + (\begin{pmatrix} Z_1 \\ Z_2 \\ Z_3 \\ Z_4 \end{pmatrix} - Z_{\mathsf{E}})^2 \tag{2.5}$$

where ΔT_i corresponds to the transmission time of the satellite signal, ν to the propagation speed of the transmitted signals in the atmosphere, Δt to the receiver clock error, X_i, Y_i, and Z_i represents the satellite coordinates and X_E, Y_E, and Z_E is the coordinate tripel for the receiver. Containing four unknown variables, this system of equations can be solved in consideration of the condition that at least four satellites are required. Therefore, equation 2.5 is stated as the general equation without reference to a special GNSS (Bauer, 2011).

The relative positioning in its differential mode can be defined as an enhanced form of the explained absolute positioning. By using two receivers, one as a reference and one as a rover, it is possible to minimize errors caused by imprecise knowledge of propagation speed and orbital data. This leads to an increased accuracy from meter up to millimeter in comparison to the absolute positioning. The receiver used as a reference is located on a known point and continuously determines its position following equation 2.4. The identified difference in position is then forwarded to the rover which should be located as close as possible to the reference station. Assuming that the difference in position determined on the reference point is the same as for the rover, the correction data can be used for positioning improvement. This enhancement is supported by complex internal algorithms developed by the provider of the reference data (Bauer, 2011).

2.3 Principle of underwater acoustics

At the beginning only used for military purposes, the underwater acoustics meanwhile are further essential for civilian applications like industrial work or scientific research. Different requirements such as bathymetric measurements, seafloor imaging or the investigation of internal sedimentary structures can be fulfilled using different kind of systems perfectly tailored to their scope. Especially the need of high-resolution imagery seafloor mapping and monitoring increased over the past few years and thus, also the sonar techniques which are working with backscatter strengths like a SAS are constantly be further developed.

2.3.1 Principle of multibeam echosounding

Nowadays, due to its measurement accuracy, a MBES is the preferred choice for the performance of seafloor depth measurements. With its wide angular coverage, it provides a cost-saving method to gather bathymetric data as well as acoustic images for large areas requiring a short period of time.

An MBES can be considered as an extended singlebeam echosounder (subsequently referred to as SBES). Whereas the SBES only sends out one vertical beam down to the seafloor, the MBES transmits and receives a fan consisting of a several hundred beams with a respective aperture angle of 1° to 2° to determine the prevailing water depth. It is thereby possible to use the high resolution of the small beams to cover a large corridor along the track of the vessel. Obviously, the total aperture of the fan is varying with the mounted system and thus is situated between 90° and 210°, whereas, according to Lurton (2010), the maximum angular width for practical usage is given by 150° what implies a seafloor coverage of 7.5 times the local water depth. MBES systems are designed with different frequencies depending on the scope, but as a general rule it can be said that the higher the water depth, the lower the required frequency. This rule of thumb is justified by the attenuation in the water column. Low-frequency signals suffer less attenuation and therefore the range is much higher in comparison to a high-frequency signal which has a comparatively low range. In general, shallow water systems operate within a frequency range between 500 kHz and 200 kHz whereas deep water echosounder use frequencies between 100 kHz and 12 kHz. For transmission and reception of the emitted signals, the MBES uses a transducer mounted in the hull of the vessel or any other appropriate place. Piezoelectric elements transform an electronic into a mechanical signal and transmit the generated acoustic pulse into the water column. The receive array records echoes which are reflected by the seafloor and reconverts this acoustic impulse into an electronic signal (Lurton, 2010).

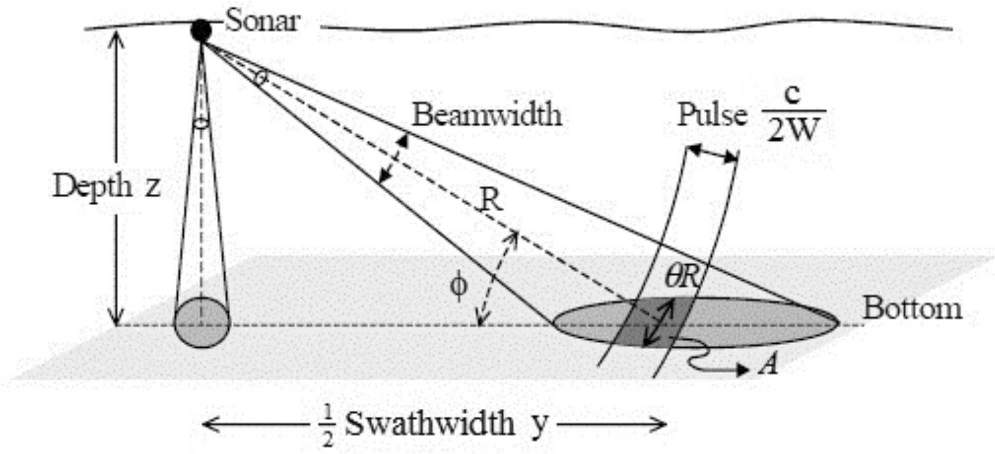

Figure 2.3: Beam geometry of a MBES and visualization of the incident pulse on the seafloor: Slant range R, grazing angle ϕ, along-track resolution θR, water sound velocity c, bandwidth W, and covered area A (according to Martinez Diaz, 2000).

The determination of the water depth is based on the exact measurement of the two-way travel time t of the acoustic signal between the transmission and the reception and the known water sound velocity c. In addition, the ray path has to be taken into account as well. Depending on the oceanographic setting, the sound speed should be determined periodically with an appropriate probe to ensure that the acoustic paths between the transducer and the seafloor are correctly registered and hence the water depth is correctly calculated. As an additional factor for the position determination of the calculated water depth, also the angle of incidence ϕ_i measured from the nadir to the outermost beam needs to be taken into account. The underlying geometrical setup for these calculations can be seen in Figure 2.3. With the help of that figure, the following two simplified formulas for the calculation of the water depth z and the half swath width y for a measured point can be derived (Lurton, 2010):

$$z = R \cdot cos(\phi_i) = \frac{c \cdot t}{2} \cdot cos(\phi_i) \tag{2.6}$$

$$y = R \cdot sin(\phi_i) = \frac{c \cdot t}{2} \cdot sin(\phi_i) \tag{2.7}$$

As a requirement for the validity of the simplified relations mentioned in formula 2.6 and 2.7, a constant sound velocity within the water column is assumed which does not correspond to a real situation. Realistic conditions imply a water column which consists of layers with different water sound velocity due to variations in temperature, salinity, and pressure. Therefore, the acoustic path cannot be described as straight due to refraction processes and calculations encountering the actual conditions become more extensive (Lurton, 2010).

In addition to the aforementioned relations, Figure 2.3 also introduces the parameters influencing the spatial resolution of the MBES. The across-track resolution ΔR set out in formula 2.8 can be expressed according to Martinez Diaz (2000) as a relation between the water sound velocity c and the signal bandwidth W which is double weighted. The along-track resolution θR given in formula 2.9 is determined by the ratio of the water sound velocity c, the frequency f, and the beam width L:

$$\Delta R = \frac{c}{2 \cdot W} \tag{2.8}$$

$$\theta R = \frac{c}{f \cdot L} \tag{2.9}$$

On the basis of the preceding formulas and Figure 2.3, it can be concluded that a high band width which is directly depending on the frequency leads to both a higher along- and across-track resolution (Martinez Diaz, 2000). Furthermore, to ensure the accurate location and computation of the water depth with an appropriate resolution, a MBES needs ancillary information consisting of position data provided by the GNSS as well as information concerning the motion of the vessel provided by an inertial measurement unit (subsequently referred to as IMU) (Lurton, 2010).

2.3.2 Principle of snippet backscatter theory

As already introduced in subsection 2.3.1, an MBES is able to record acoustic images. For this, the intensity of the backscattered signal returned from the seafloor is used to generate an image representing the seafloor reflectivity. With the aid of these information it is possible to derive seabed characteristics.

The signal transmitted by the MBES strikes the seafloor in different angles. For normal incidence, most of the energy is reflected according to the law of reflection. Due to this, it is called specular reflection or facet. For oblique incidence, scattering and volume scattering occurs which is influenced by the heterogeneity of the seafloor sediments. The penetration depth depends on the frequency, the impedance contrast of the different media, and the acoustic attenuation. Acoustic impedance characterizes the resistance to the propagation of the sound and is depending on the nature of the medium. Seawater has a relatively low attenuation in comparison to the sediments forming the seafloor which in turn leads to a more undisturbed forwarding of the acoustic echo as the particles can move more easily then the ones in the denser material. Both a low frequency and a low impedance contrast lead to an increase of the penetration depth. The composition of the sediment can differ significantly so that physical processes of absorption, refraction and scattering occur in dependence of the local sediment conditions. In the outer beams of the swath, a grazing incidence lead to surface scattering which is related to the micro-scale roughness of the seafloor. It describes a ratio between the physical irregularities of the subsea surface and the wavelength of the transmitted acoustic signal (Lurton, 2010).

Besides the chosen frequency also the local relief characteristic have an influence on the roughness indicated by the backscatter strength. A beam with a small incident angle creates just a small footprint on the seafloor and therefore covers only a few facets of the sediment. This enables a reflection of the transmitted acoustic energy in specular direction. However, with an increasing incident angle also the ensonified part of the seafloor and hence the number of facets increase. Since not all of these facets are orientated towards the incident wave, this leads to a decreasing backscatter strength of the facets. But considering the increased number of facets, an interaction of scatterings which occur with the same amplitude takes place. The described creation of the backscatter field is known as the Bragg scattering domain. Figure 2.4 illustrates the described context (Lurton, 2010):

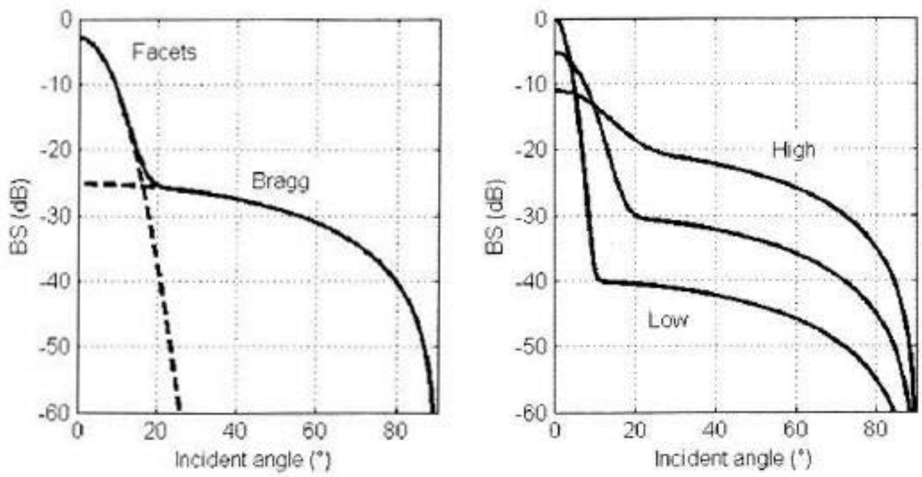

Figure 2.4: Idealized backscattering strength as a function of incident angle (from left to right): Facets and Bragg regime and the influence of roughness (Lurton, 2010).

Parts of the acoustic energy are reflected and other parts penetrate the seafloor where they are subject to refraction processes. The remaining part of the signal is scattered depending on the consistence and morphology of the seafloor. The scattering straight towards the incident wave and therefore back to the MBES is named backscatter (Lurton, 2010).

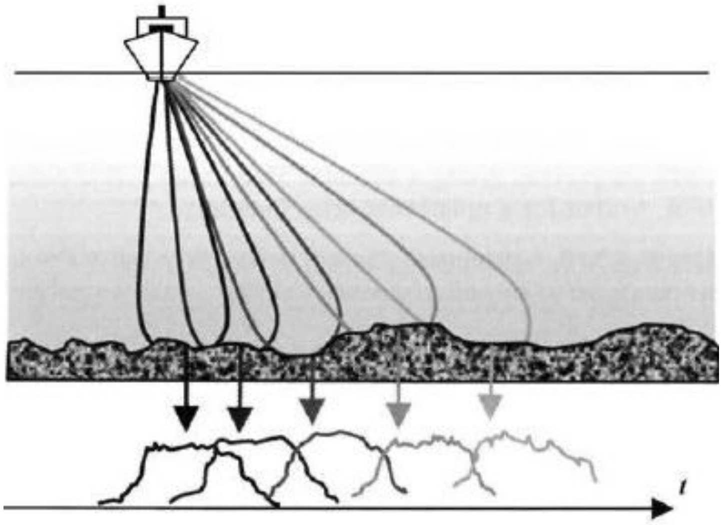

Figure 2.5: Formation of a sonar image using MBES (Lurton, 2010).

The backscattered signal is recorded in a time series for each beam. To generate a sonar image of the ensonified area, all image segments need to be recombined and arranged line by line along the swath as depicted in Figure 2.5. This recombination is ideally done after the evaluation of the depth measurement to ensure that the imagery data is connected to the right position, whereas only the depth values at the determined center points are known; all intermediate points get an interpolated depth value. For the performance, the center point of each beam needs to be determined and placed on the swath at the correct position. After that, the surrounding intensity values within one beam known as snippets are used for image formation until the intersection with the adjacent beam. Thereby, the number of snippets depends on the pulse length as it was illustrated in Figure 2.3. The shorter the pulse length, the more snippets may be generated. (Lurton, 2010).

The theoretical computation of backscatter intensity values and all related indications is based on the active sonar equation as stated below in its shortened form. Attention is paid to source level SL, transmission loss TL, target strength TS, noise level NL as well as the receiver and processing gain RG respectively RL. The intensity of the echo which is received by the transducer is defined as the echo level EL and expressed in dB (Lurton, 2010):

$$EL = SL - 2 \cdot TL + TS - NL + RG + PG \tag{2.10}$$

As mentioned, the echo level is affected by several factors arising from the process of signal transmission in the water column. The source level SL can be defined as the amount of acoustic energy transmitted into the water column and, as it describes a relative intensity, is given as a dB value[7] (Lurton, 2010). Due to geometrical spreading and absorption processes, the transmitted source level decreases with an increasing distance between the transducer and the target. Equation 2.11 illustrates this relation (Hammerstad, 2000):

$$2 \cdot TL = 2 \cdot \alpha \cdot R + 40 \cdot log(R) \tag{2.11}$$

The distance between transducer and target is given as the slant range R given in meter and α is named as the absorption coefficient given in dB per square meter. The combination of these two factors is summarized to the transmission loss TL, also given as a dB value. As the signal needs to travel towards the target and also back to the transducer, it needs to be applied twice (Lurton, 2010). Due to scattering processes, only parts of the emitted signal are reflected back to the transducer. The ratio between the intensity of the backscattered signal I_{bs} and the incident intensity I_i is defined as target strength TS, given as a dB value and indicated in equation 2.12 (Hammerstad, 2000). The target strength depends on the texture and the external and internal structures of the sediment as well as on the incidence angle and the frequency of the acoustic signal (Lurton, 2010). These characteristics as well as the beam geometry are important for backscatter imaging wherefore it is also possible to define the target strength as the logarithmic representation of the backscattering cross-section σ shown in equation 2.13 (Ona, 1999):

$$TS = 10 \cdot log(\frac{I_{\mathsf{bs}}}{I_{\mathsf{i}}}) \tag{2.12}$$

$$TS = 10 \cdot log(\frac{\sigma}{4 \cdot \pi}) \tag{2.13}$$

Depending on the incidence angle ϕ_i, the ensonified backscattering area has different boundings. For an incidence angle of 0°, the area instantaneously ensonified by the acoustic pulse is bounded by the beam geometry defined by along- and across-track aperture ϕ_L respectively ϕ_T and the slant range R. For all deviating directions, the backscattering caused by a propagation sonar pulse depends on water sound velocity c, transmitted pulse length τ, along-track aperture ϕ_L, and the slant range R (Hammerstad, 2000):

$$BA = \begin{cases} \phi_{\mathsf{L}} \cdot \phi_{\mathsf{T}} \cdot R^2 & \text{for } \phi_{\mathsf{i}} = 0° \\ \dfrac{c \cdot \tau}{2 \cdot sin(\phi_{\mathsf{i}})} \cdot \phi_{\mathsf{L}} \cdot R & \text{for } \phi_{\mathsf{i}} \neq 0° \end{cases} \tag{2.14}$$

[7]It should be mentioned that it is a frequent practice to reference both the source level and the target strength to a distance of one meter away from the transducer respectively the target (Lurton, 2010).

The backscatter strength for a unit of surface and is very important for the characterization of the composition of material located on the seafloor. The fact that the backscatter strength is dimensionless thereby makes it a common value to refer to as it is not affected by the applied unit system. According to Jackson et al. (1986) it is possible to express it as a dimensionless value which consists of the input parameters slant range R, the scattered intensity I_s, the incident intensity I_o, and the backscattering area BA:

$$BS = \frac{R^2 \cdot I_s}{I_o} \cdot BA \tag{2.15}$$

$$BS = BS_0 + 20 \cdot log(cos(\phi_i)) \tag{2.16}$$

As the backscatter strength depends on the angle of incidence whereas the incident angle behaves towards the strength of the returned energy in an inverse proportionality. This leads to the following determination: The smaller the angle of incidence, the higher the returned acoustic energy. For all incident angles larger than 25°, an approximation considering the mean unit backscatter strength BS_0[8] was formulated and announced as Lambert's Law stated as 2.18 (Hammerstad, 2000, Lurton, 2010).

The backscatter strength depends on geoacoustic properties, seafloor roughness, and the incidence angle as depicted in Figure 2.6. The most important thing is the geometry. This includes the inclination of the seafloor in relation to the incident wave. A slope towards the transmitted beam produces a stronger backscatter signal than a slope in opposite direction as indicated by the grey ovals. Furthermore, also the local incidence angle is very important for the backscatter signal. A small incidence angle produces a stronger backscatter signal than a larger one appearing in the outer beams of the swath. A further significant condition is given by the physical characteristics of the seafloor expressed by the seafloor roughness. If the seafloor appears as a very smooth surface, most of the produces scattering is radiated in the specular direction of the incident wave just as for reflection processes. For rough surfaces, the signal is backscattered more strongly. Last but not least, the intrinsic structure of the seafloor considering the composition and the density of the material affects the backscattering. As it can be seen in the lower image area, the way the scatter is propagated is influenced by the heterogeneity of the sediment surface layers (Blondel, 2009).

[8]The mean unit backscatter strength or mean backscatter coefficient refers to a uniform flat bottom (Hammerstad, 2000). As an upper limit of BS_0, a value around -5 $\frac{dB}{m^2}$ can be defined in theory, but practically observed values range between -10 and -40$\frac{dB}{m^2}$ (Lurton, 2010).

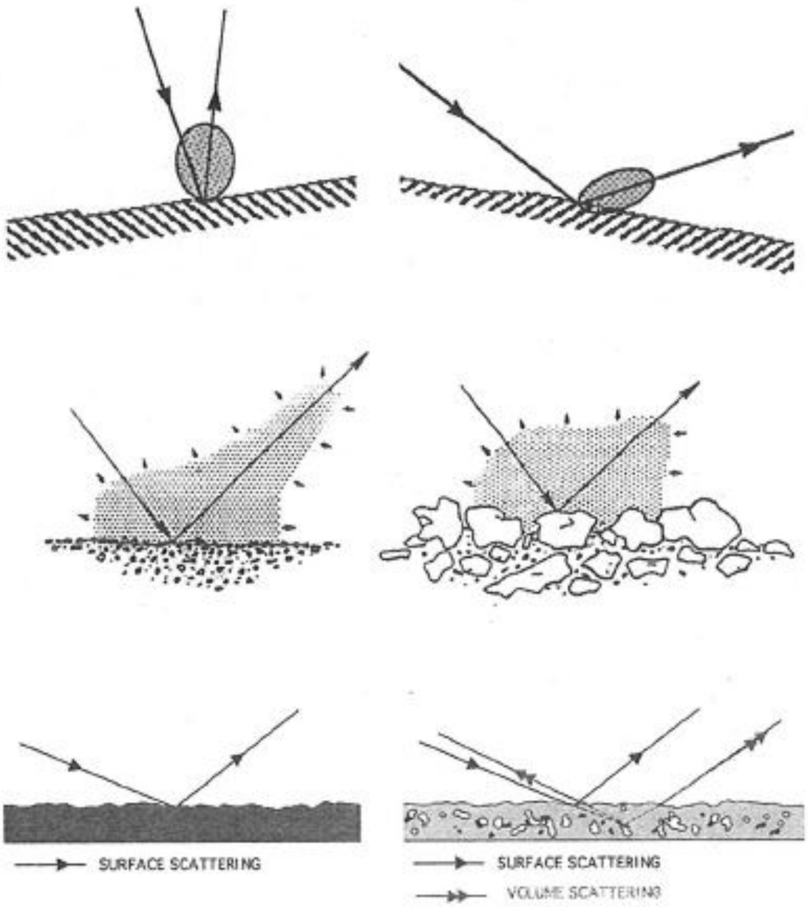

Figure 2.6: Influence factors for backscattering at the seafloor (from top to bottom): Local geometry of the ensonified area, roughness of the seafloor at scales comparable with the wavelength of the transmitted echo, intrinsic properties of the seafloor (e.g. rocks vs. sediments) (Blondel, 2009).

2.3.3 Principle of parametric sub-bottom profiling

In comparison to an MBES, a sub-bottom profiler (subsequently referred to as SBP) is able to offer an insight to sedimentary layers beneath the surface. Using this technique, embedded objects can be detected and therefore a SBP is an essential tool for geological investigations.

Generally spoken, a SBP works similar to a SBES. The only difference is in the used frequency range. While SBES uses high frequencies to detect only the seafloor, a SBP uses low frequencies in a range from 2 kHz up to 10 kHz to be able to penetrate it as shown in Figure 2.7. The acoustic signal is reflected by the interfaces between the individual sediment layers and returns to the transducer to offer a vertical cross-section of the investigated environment. As it can be seen in the right part of the Figure 2.7, only the specular reflection of the signal points out the particular sediment layer what leads to an independence of the

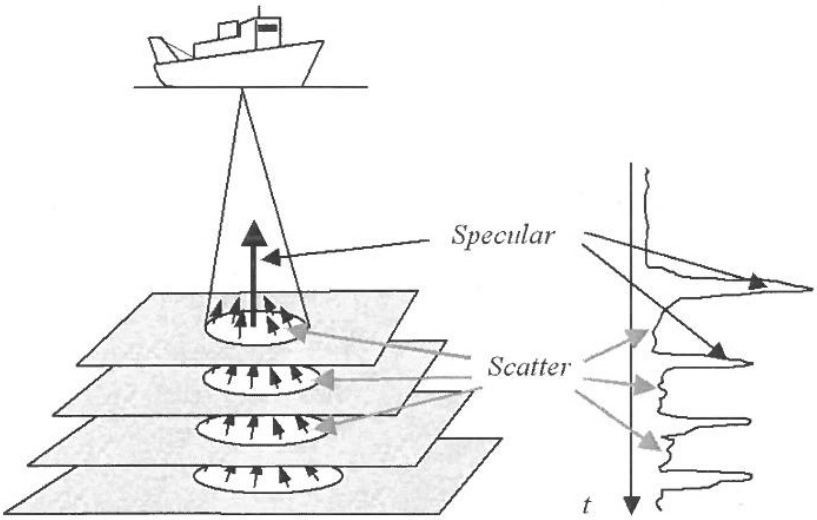

Figure 2.7: Formation of the echo from a sub-bottom profiler (Lurton, 2010).

beamwidth in the context of image quality evaluation (Lurton, 2010). However, a system using low frequency requires an appropriate large transducer to emit the acoustic energy into the water column. This fact in its turn leads to the need of a large vessel which is not able to operate in shallow water areas due to its draft. In order to avoid this problem, the parametric effect known from the field of physics, is used for low frequency beamforming.

To generate a non-linear sound, two slightly different high frequency signals are emitted at the same time. Due to the interference occurred when both signals entered the water column, a low frequency signal results from the difference between the two high frequencies. The resulting low frequency signal offers a large bandwidth, short pulse length, and a narrow beam width what makes is particularly suitable for sub-bottom profiling and object detection (Wunderlich et al., 2005).

The maximum penetration depth the generated low frequency can reach can be derived from the sonar equation. Based on this equation, the sediment properties expressed by the absorption coefficient are decisive for the maximum penetration depth. As the absorption coefficient depends on the frequency, it can be said that the generated frequency constrains the penetration range of the SBP. According to Lurton (2010), a working frequency around 3.5 kHz has proven its worth.

To achieve a high vertical resolution, short pulses and a narrow beam width are recommended. Commonly used for the calculation of the vertical resolution Δz is formula 2.17 taken from Wunderlich et al. (2005), where c represents the sound velocity and T_e the effective pulse duration. Whereas the vertical resolution can be assumed to be almost constant, the horizontal resolution Δx is given by the maximum dimension of the first Fresnel zone which results of the frequency λ and the sum of water and penetration depth H respectively H_s (Lurton, 2010):

$$\Delta z = \frac{c}{2} \cdot T_{\mathsf{e}} \tag{2.17}$$

$$\Delta x = \sqrt{\frac{\lambda \cdot (H + H_{\mathsf{s}})}{2}} \tag{2.18}$$

As stated by Theuillon et al. (2008), the gathered image of the sediment structures can be supplemented by estimated values characterizing the reflectivity or the acoustic impedance. Analyzing these physical parameters, a selective seabed classification based on sub-bottom profiling data is conceivable, but incomparable to the snippet backscatter information due to the coverage.

3 Acquisition of data

The data this thesis is based on was collected during the research cruise AL447 with RV ALKOR. The expedition started from Kiel, Germany, on October 20, 2014 and ended in Kiel on November 04, 2014. The route of the vessel is traceable in Figure 3.1:

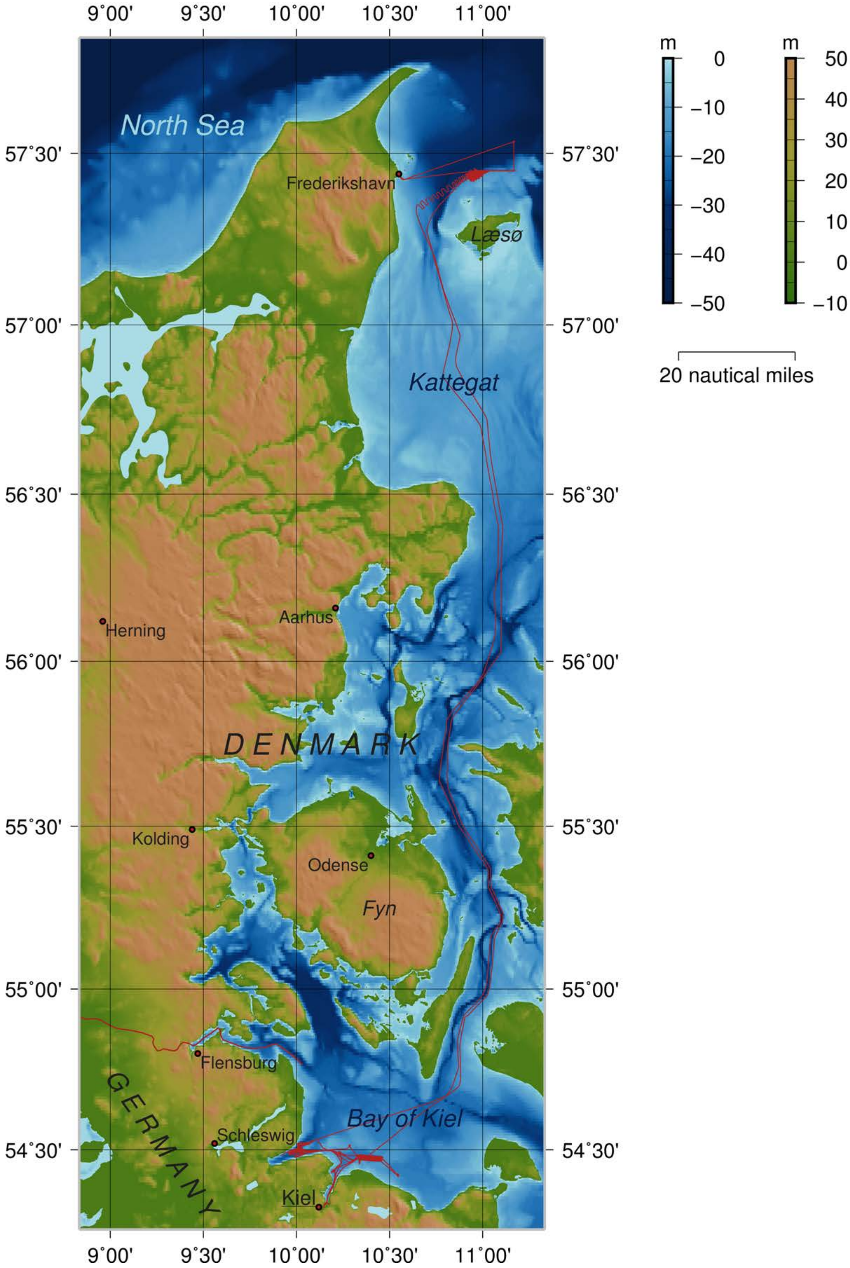

Figure 3.1: Shiptrack of the RV ALKOR cruise AL447. Mercator projection with global dataset GEBCO 2008 (30 arc-seconds) provided by GEBCO (2016). The full size figure can be found in Appendix A.

The research cruise was organized by the Helmholtz Centre for Ocean Research GEOMAR, Kiel, and conducted by chief scientist Dr. Jens Schneider von Deimling. In the framework of the European research projects SUGAR II[9] and ECO2[10], the expedition should have acted as a platform to test acoustic remote sensing tools for gas seep evaluations. Using geochemical and geophysical methodologies, the understanding of seepage triggering methods as well as the fate of gaseous dissolved seepage methane and their potential transfer to the atmosphere should have been improved. During the whole cruise, strong westerly winds occurred in the Skagerrak area of the North Sea. Even in the more protected Kattegat, wind speed with up to 15 $\frac{m}{s}$ were recorded with the vessel-based weather station. With regard to the mentioned prevailing weather conditions, the seepage site in the Eckernförde Bay, Germany, and a bubbling reef near the island of Læsø, Denmark, were investigated instead of the off-shore seepage sites in the North Sea. In addition to the mentioned activities and with the collaboration of the MELUR, the baseline study this thesis is dealing with was conducted in the area of the ammunition dumping site Kolberger Heide (Schneider von Deimling, 2015).

Following up the presentation of the investigated area, the survey instruments utilized for the acquisition of data are introduced. Furthermore, a clarification of the calibration procedures both for MBES and IMU executed ahead of the actual measurements is given.

3.1 Geographical extend of the investigated area

In the course of the dumping site investigation, 538 profiles were recorded in total. The survey lines were logged in five small projects[11] during several days which complement each other to a connected area with a size of 16.7 km^2 as depicted in Figure 3.2. The line planning was done during the cruise using the ocean floor observation protocol mapping software OFOP. Considering the prevailing water depth and the slope of the seafloor, an optimal overlap of the surveyed parallel lines was ensured. The evaluated profiles were acquired with an average speed of 4 knots, the required overall survey time amounts to 78 hours.

[9] The three-year SUGAR II project was funded by the Federal Ministry of Education and Research and the Federal Ministry of Economy and Technology. In addition, financial support was contributed by several involved parties from industry, private companies, and research institutes. Coordinated by the Helmholtz Centre for Ocean Research GEOMAR, Kiel, the project covers the research of submarine gas hydrate reservoirs (GEOMAR, 2014).

[10] The four-year ECO2 project funded by the European Union covers researches on the issue of sub-seabed CO_2 storage and the impact on marine ecosystems. The project was coordinated by the Helmholtz Centre for Ocean Research GEOMAR, Kiel (GEOMAR, 2016).

[11] Heidkate_1: 15 profiles recorded on October 20, 2014. Heidkate_2: 148 profiles recorded on October 20-21, 2014. Heidkate_3: 69 profiles recorded on October 23-24, 2014. Heidkate_4: 82 profiles recorded on October 25-26, 2014. Heidkate_5: 224 profiles recorded on November 02-04, 2014.

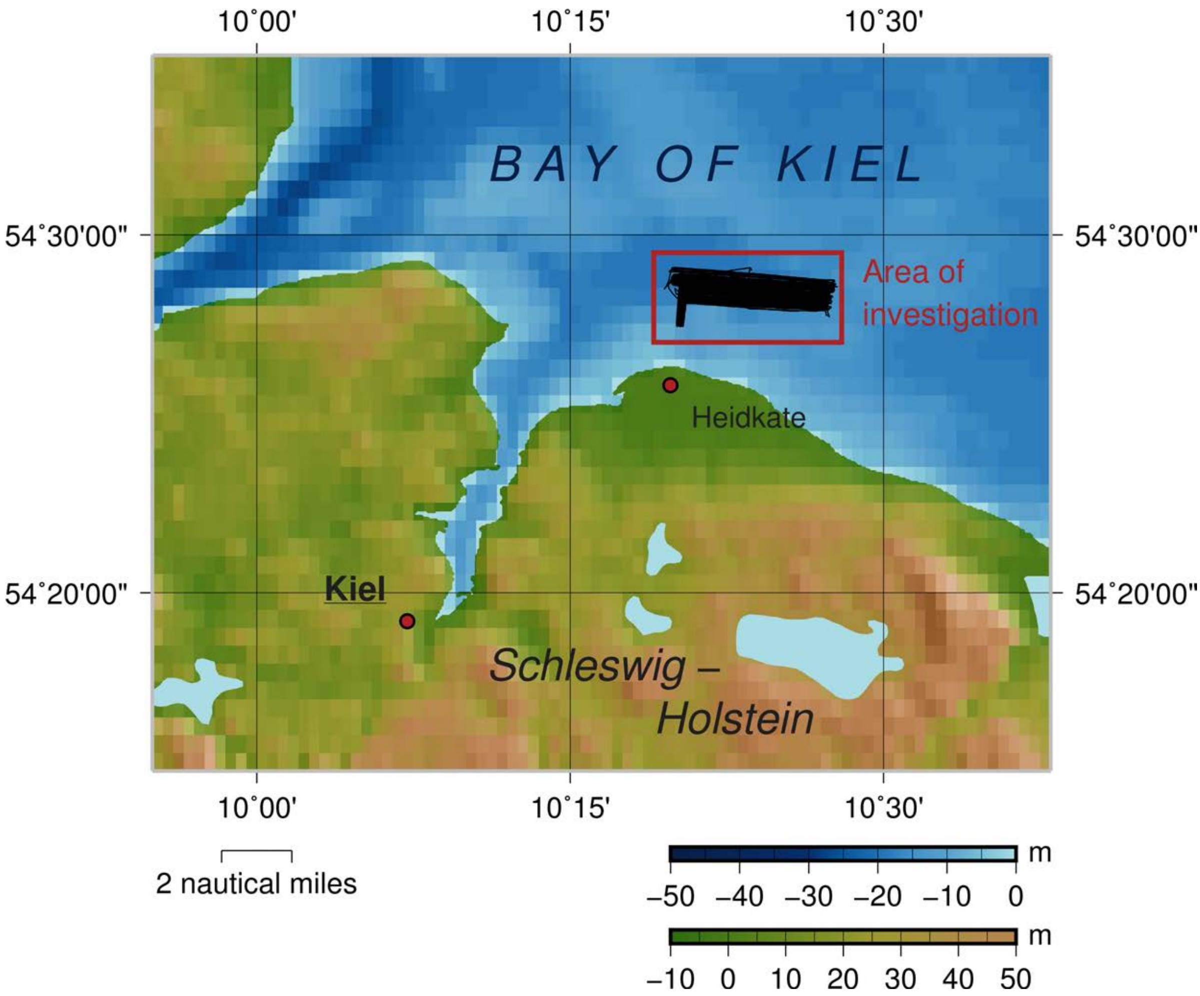

Figure 3.2: Area of investigation in the Kiel Bay. Mercator projection with global dataset GEBCO 2008 (30 arc-seconds) provided by GEBCO (2016) and tracklines of all conducted projects.

The area of investigation is located roughly 4.5 km northeast of the Schleswig-Holstein coastline in the Bay of Kiel near to Heidkate. In this coastal area, the water depths with a range from 5 m to 18 m are very shallow due to the storm surge of 1625. Immediately adjacent in the northwest of the survey area lies the accounted ammunition dumping site Kolberger Heide as already indicated in Figure 1.3. This official designated and appropriately marked dumping site covers around 12 km^2, the shortest distance to the coastline is only about 2 km.

3.2 Hydrographic data acquisition within the scope of AL447

As a platform for the accomplished hydrographic survey the medium sized German research vessel ALKOR pictured in Figure 3.3 was used. Launched in September 1989 at the Cassens shipyard in Emden, the vessel is operated by the Helmholtz Centre for Ocean Research GEOMAR[12].

Figure 3.3: Research vessel ALKOR (GEOMAR, 2012).

With a length of 55.2 meter and a beam of 12.5 meter, the ALKOR can accommodate 12 scientists and 12 crew members for a period of 21 days at sea (Institut für Meereskunde, 1989). The main area of operation is the European continental shelf comprising the North as well as the Baltic Sea, the English Channel, the Irish Sea, and the Norwegian Sea (GEOMAR, 2013a).

[12] The Helmholtz Centre for Ocean Research GEOMAR, re-organized in the contemporarily form in 2012, is a scientific research institution based in Kiel, Schleswig-Holstein. Up to the launching time of the ALKOR in 1989, the Institute for Oceanography (Institut für Meereskunde) was registered as the operator of the vessel (GEOMAR, 2013a, 2013b).

3.2.1 Inertial navigation system Coda Octopus|NovAtel F180R

To ensure that both the motion of the vessel and the position are recorded, the self-calibrating INS F180R developed by Coda Octopus Products Ltd. was installed for the AL447 research cruise. As the system does not belong to the standard equipment of RV ALKOR, it was mounted before setting off. The F180R is a multi-sensor system which combines an IMU with a two-antenna GNSS system provided by NovAtel Inc.. In this configuration, it is able to gather the attitude as well as the dynamics and the geographical position of a vessel on a precise level. The world geodetic system established in 1984 (subsequently referred to as WGS84) serves as a global reference frame for position and height data. The data collected with both system components come together in the processing unit which is in turn connected to the hydrographic work station for forwarding all information to the MBES acquisition software (Coda Octopus Products Ltd., 2013).

Figure 3.4: Mounting of the F180R antenna system on RV ALKOR. Baseline installation (left) and detail view of the master antenna (right) (Pictures by T. Kunde (left) and P. Held, GEOMAR (right), 2014).

On RV ALKOR, as shown in Figure 3.4, the GNSS antennas were mounted with a baseline distance of two meters on the railings of the top deck. This is an important consideration with regard to the accuracy for heading, attitude, position, and velocity. The IMU was mounted on the moon pool plate close to the MBES; an impression of the installation process is given in Figure 3.5. Subject to the condition that the possibility of using differential GPS is given, a theoretical position accuracy of 0.25 m can be achieved. When using the stand-alone solution without any correction data, the position accuracy is reduced to 0.50 m. Independent of the GNSS solution status it should be mentioned that the given accuracies are of pure theoretic nature as the actual performance depends on external factors like the constellation of satellites. Both the attitude and heading accuracy is independent of baseline distance and GNSS solution status and amount to 0.025° respectively 0.05° (Coda Octopus Products Ltd., 2013). To obtain an overview, all described technical specifications of the F180R system are listed in Table 3.1 below.

Table 3.1: Physical specifications and system performance of Coda Octopus|NovAtel F180R (Coda Octopus Products Ltd., 2013).

Physical specifications	
IMU Diameter	120 mm
IMU Height	170 mm

System performance	
Output rate	100 Hz
Heading accuracy	0.05°
Attitude accuracy	0.025°
Stand-alone position accuracy	0.50 m
DGNSS position accuracy	0.25 m

To control the INS, the manufacturer-specific software F180R Application Suite is used. This software implies both the configuration and any other control functions required for the system operation. In addition, the output data logging can be defined within the software. The output is comprised of information for position, attitude, heading, velocity, track, speed, and acceleration. All of them are combined in a so called *.mcom file. In addition, the diagnostic raw data file characterized by the suffix *.rd is stored internally. These files is of particular importance if the collected data should be post-processed to apply GNSS corrections (Coda Octopus Products Ltd., 2013).

For the AL447 cruise, an additional GNSS antenna was mounted to receive differential GPS correction data provided by Fugro. However, this did not provide the desired results caused by shadowing effects due to the antenna position on the vessel. Therefore it was decided to henceforth perform the conducted data acquisition without the available correction service.

3.2.2 Multibeam echosounder Kongsberg EM 2040C

For the acquisition of bathymetric data, the MBES EM 2040C from Kongsberg Maritime AS was installed on RV ALKOR. As well as the INS, this compact echosounder does not belong to the standard equipment on the vessel and therefore was mounted and calibrated in the moon pool right before the beginning of the cruise as shown in Figure 3.5. It is a high resolution echosounder specifically designed for shallow-water areas up to 520 m. The two arrays responsible for the transmission and reception of the acoustic signal are housed in a 22.9 kg sonar head with a diameter of 332 mm and a height of 119 mm which make the system very compact and therefore easy to install even on small vessels (Kongsberg Maritime AS, 2013a).

Figure 3.5: Mobile installation of the EM 2040C transducer (red) and the acoustic Doppler current profiler (yellow) on the moon pool plate (Schneider von Deimling, 2015).

Depending on the application, the frequency can be chosen in a range from 200 kHz to 400 kHz and therefore, the opening angle of the swath can vary from 70° up to 130°. During the AL447 cruise, a frequency of 300 kHz was used which implies an aperture angle of 130°. This setting allows a theoretical coverage of 4.3 times the actual water depth. Besides the frequency, also the bottom type and the attenuation effects the swath width and the accessible depth as depicted in Figure 3.6 (Kongsberg Maritime AS, 2013a).

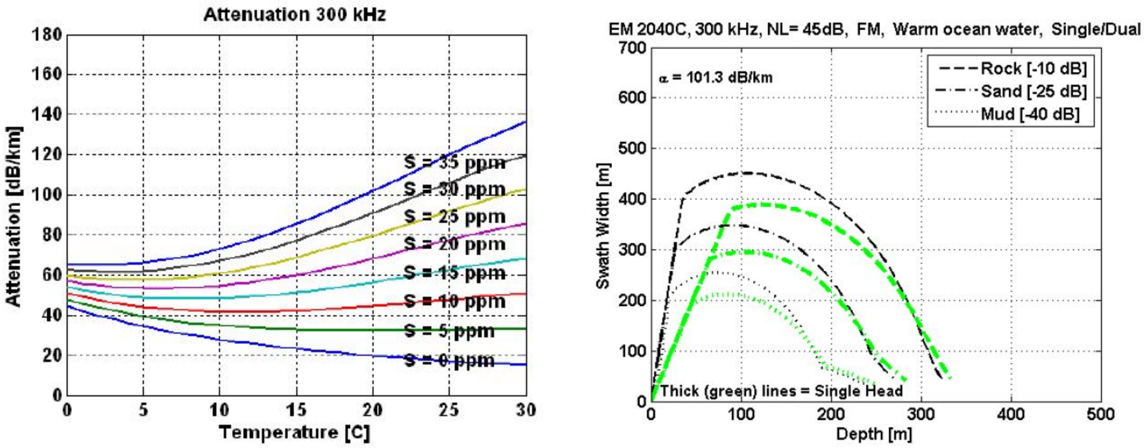

Figure 3.6: Attenuation and coverage of EM 2040C. Attenuation in the water surface $[\frac{dB}{km}]$ as a function of the water temperature [°] for different salinity values (left). Swath coverage [m] as a function of water depth [m], displayed for different bottom types (right) (Kongsberg Maritime AS, 2013a).

For 300 kHz, the swath consist of up to 400 beams with a respective width defined as 1.3° x 1.3°. The actual number of beams depends on the chosen beam spacing option which are named as equidistant, equiangular, or high density. To ensure a uniform sampling in across-track direction, it was set to equidistant during the AL447 cruise. The sampling was carried out with a pulse length of 50 μs which corresponds to the pinging mode very shallow. To guarantee the best possible comparability of the backscatter intensity values with the already executed SSS recordings, the pinging mode was set constant. The ping rate is given as a function of the water depth and amounts to 50 kHz (Kongsberg Maritime AS, 2013a). To obtain an overview, all described technical specifications of the EM 2040C are listed in Table 3.2.

For the acquisition of data, the Seafloor Information System (subsequently referred to as SIS) in version 4.1.5 was used as the interface between MBES and user. The software installed on the hydrographic work station was developed by Kongsberg Maritime AS and offers a flexible layout of the screen with the possibility to display various information in up to seven adjustable windows. Within SIS, the system performance as well as several other settings can be predefined and stored to the created project. During the acquisition process, the incoming data can be monitored in real time (Kongsberg Maritime AS, 2013b).

Table 3.2: Physical specifications and system performance of Kongsberg EM 2040C (Kongsberg Maritime AS, 2013a).

Physical specifications	
Diameter	332 mm
Height	119 mm
Weight	22.9 kg in air (12.3 kg in water)

System performance	
Frequency	200 - 400 kHz
Maximum ping rate	50 Hz
Number of beams per swath	up to 400 beams per swath
Beam width	1.3° x 1.3° for 300 kHz
Beam spacing options	equidistant, equiangular, or high density
Coverage sector	70° – 130°
Maximum depth	520 m for 200 kHz in cold ocean water
Pulse length	25 – 600µs
Range sampling rate	up to 61 kHz (15mm)

The logged data was stored in the manufacturer-specific *.all format. Depending on the survey, these files consist of different datagrams[13]. To provide an insight into the file structure, the processing software CARIS HIPS and SIPS 8.1 with its dump utility offers the possibility to display the content of each *.all file. An extract of such a file logged during the AL447 cruise is shown in Appendix B. As the *.all files contain lots of data, it was predefined in the SIS settings to generate a new file every ten minutes for all executed surveys to keep the file size at a low level.

According to Hammerstad (2000), the backscatter values which are particularly emphasized in this thesis are stored in two different ways and in two different datagrams. In the depth datagram, the backscatter values are represented by a beam average of the sample amplitude value. Due to the fact that the backscatter value is corrected for the time varying gain (referred to as TVG) there are no scaling issues with regard to the beam angle. The backscatter values stored in the seabed image datagram use these beam amplitude samples to generate a time series of reflectivity values for each beam. The intensity values which surround the

[13]Possible output datagrams are organized in four categories depending on their origin; the datagrams mentioned in parenthesis are selected examples: Multibeam data (depth or water column datagram), external sensors (attitude datagram), sound speed (SVP datagram), and SIS generated output. In addition, information about the multibeam parameters and the status of the processing unit are stored (Kongsberg Maritime AS, 2015).

center point of each received beam are evaluated and stitched together to thereby create a snippet backscatter time series format along the whole swath.

Taking a look into the seabed image datagram, the total number of pixels registered for one ping is stated. This is of particular interest for the resolution assessment of the time series format in comparison to the beam average format. In the investigated area referred to in this thesis, the number of pixels per ping is between 3000 and 4000 for the complete swate which indicates a much higher resolution of the time series format.

3.2.3 Sub-bottom profiler Innomar SES-2000 standard

To investigate the sediment layers beneath the seafloor, a SBP operating with low-frequency is required. The SES-2000 standard system provided by Innomar Technologie GmbH is permanently installed on RV ALKOR, but it was declined in favor of MBES data collection to run one or more profiles within the investigated area. However, within the framework of a day trip with RV LITTORINA in March 2015, six profiles were taken as shown in Figure 3.7, whereas the sixth profile does not overlap with the investigation area.

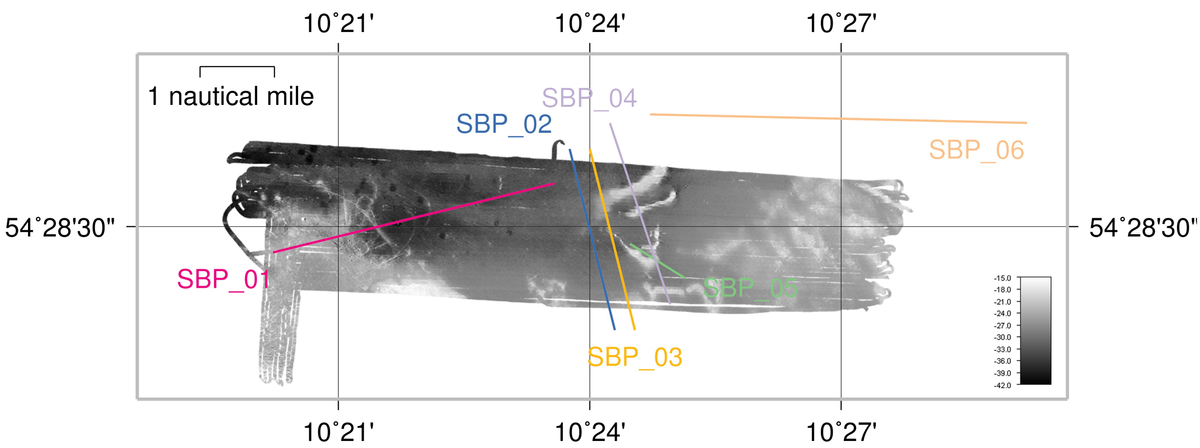

Figure 3.7: Location of SBP profiles from RV LITTORINA daytrip in relation to the survey area indicated by the snippet backscatter image (Mosaic pixel size: 0.50 m x 0.50 m). Dark colors represent low backscatter intensities, light colors indicate high backscatter intensities (Values given in dB). The full size figure can be found in Appendix A.

During the data acquisition, primary frequencies of 100 kHz and 108 kHz were used. Following the parametric effect, a secondary frequency of 8 kHz was generated for bottom penetration and the investigation of the upper sediment layers during the sunducted survey.

In order to get an insight into the technical specifications of the parametric SBP SES-2000 standard, Table 3.3 lists the key figures of the system in use (Innomar Technologie GmbH, 2009a).

Table 3.3: Physical specifications and system performance of Innomar SES-2000 standard (Innomar Technologie GmbH, 2009a).

Physical specifications	
Dimensions	300 mm x 260 mm x 70 mm
Weight	30 kg including 30 m of cable

System performance	
Primary frequency	about 100 kHz
Secondary frequency	4 - 15 kHz (user adjustable)
Aperture angle	$\pm$ 1.8°
Depth range	1 - 500 m
Penetration	up to 50 m
Accuracy (100 kHz)	0.02 m + 0.02 % of water depth
Accuracy (10 kHz)	0.04 m + 0.02 % of water depth

For data acquisition during the cruise, the software SES for Windows, formerly known as SESWIN, provided by Innomar Technologie GmbH was used. Beneath the real time display of the echosounder data, the user interface offers possibility to control the adjustable hardware parameters and to monitor incoming data as the navigation, motion data, or the actual track of the vessel. The recorded data can be stored in two different file formats. Per default, the file format *.ses is used for storage. It includes the envelope data of the recorded data. As a second option, the *.raw files offer the possibility to store the full waveform data of the received signal in addition to the *.ses format (Innomar Technologie GmbH, 2009a).

3.2.4 CTD probe

During the cruise, the sound velocity in the water column was acquired in the context of several measurements determining the actual conductivity, temperature, and depth (subsequently referred to as CTD). In regular depth intervals, the temperature, pressure, and conductivity represented by the value of salinity is measured and stored internally in a *.txt format. On RV ALKOR, the CTD probe was mounted in the center of a multi water sampler consisting of twelve tubes as it can be seen in Figure 3.8. During the lowering process, these bottles can be closed to obtain appropriate water samples used for biological and chemical analysis of the water column composition. This can be of particular interest with regard to possible pollutants due to the corrosion of ammunition bodies.

Figure 3.8: Multi water sampler with mounted CTD probe (Picture by P. Held, GEOMAR, 2014).

To be able to apply the measured sound velocity to the bathymetric data during the run time of the acquisition process, it is necessary to generate sound velocity profiles (referred to as SVP). Therefore, the sound velocity values logged during the downcast of the probe need to be extracted and converted into an *.asvp format which can be opened within the Kongsberg SIS software. Hence, before the data can be read in and applied to the current survey project, it needs to be revised and extended to fulfill internal software issues.
During the data acquisition, several CTD profiles were taken. The detailed information of the sound velocity profiles are listed in Table 3.4, whereas the locations are pictured in Figure 3.9.

Table 3.4: CTD profiles taken during AL447 in the area around the dumping site Kolberger Heide.

CTD station	Date	Time	Latitude	Longitude
1324	2014-10-21	06:43	54° 28.43’	10° 27.31’
1325	2014-10-21	10:42	54° 28.39’	10° 27.27’
1352	2014-10-23	17:48	54° 28.56’	10° 20.45’
1374	2014-10-26	07:42	54° 27.99’	10° 27.16’
1375	2014-10-26	08:28	54° 29.06’	10° 23.66’
1429	2014-11-02	18:28	54° 28.86’	10° 20.19’
1436	2014-11-03	12:16	54° 27.75’	10° 27.31’

3.2.5 Van-Veen grab sampler

For ground truthing, a Van-Veen grab sampler was used to collect sediment samples of the upper seafloor layer on a random basis. Before lowering the grab sampler into the water column on a cable, the clamshell needs to be locked. Fixed in this position by a hook, the gripper jaws are open until the grab sampler hits the seafloor. The soil contact leads to the release of the locking mechanism and the gripper jaws close themselves. Now, the cable can be hauled up again which leads to the closure of the gripper jaws. During this procedure, the upper sediments are trapped inside and can be transported to the sea surface. The one drawback is the fact that the sediments are mixed during the grabbing process, but to grasp a general overview this method is sufficient.

During the research cruise, two sediment samples were taken at the end of the cruise. This sample collection has required a closer inspection as the survey area is partly riddled by ammunition remnants. Therefore, the two samples were taken off the actual survey area as pictured in Figure 3.9, the detailed information of both samples are listed in Table 3.5.

Table 3.5: Grab core samples taken during AL447 in the area around the dumping site Kolberger Heide.

Grab core sample	Date	Time	Latitude	Longitude
1431-1	2014-11-03	06:31	54° 25.14’	10° 32.69’
1431-2	2014-11-03	06:54	54° 25.11’	10° 32.65’

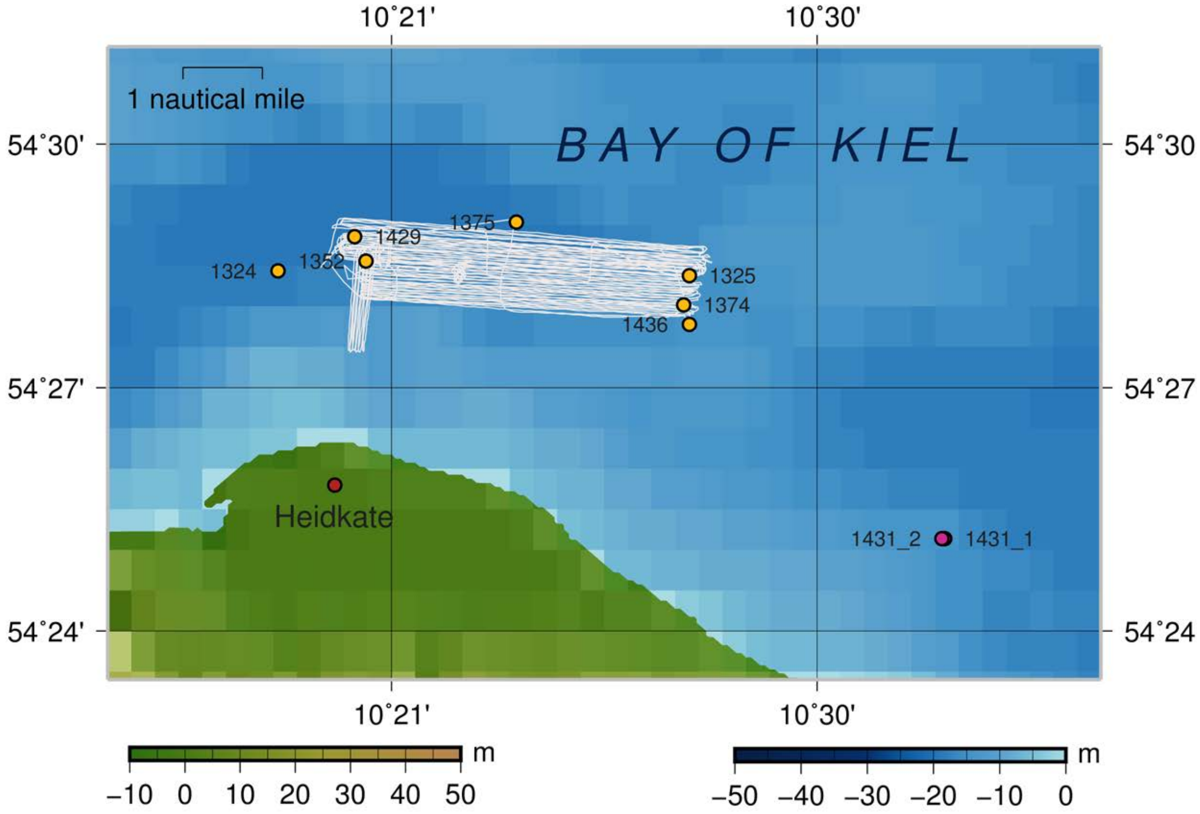

Figure 3.9: Location of CTD profiles (yellow) and grab core samples (violet). Mercator projection with global dataset GEBCO 2008 (30 arc-seconds) provided by GEBCO (2016) and tracklines of all conducted projects.

3.3 Calibration procedures

Whenever a hydrographic survey is executed, different types of errors can affect the data acquisition. These can be subdivided in random errors which cannot be excluded in advance as they occur instrument specific, and systematic errors which can be mostly wiped out with a calibration performed in forehand. According to Hare (1995) and Hughes Clarke (2003), the mentioned systematic errors can be categorized due to their influence in depth and position errors as listed in Table 3.6:

To meet requested accuracy requirements and therefore to ensure a high data quality, a calibration of the installed systems should be carried out even before the real data acquisition begins to minimize systematic influences. Depending on the respective properties, each instrument has its own calibration procedure to follow, but all MBES follow the same calibration scheme.

Table 3.6: Total error budget for a MBES survey. Subdivided into depth errors and position errors (Hare, 1995).

Depth error budget	
Sounder system error	Range and beam angle measurement errors ans beam width resolution
Roll error	Measurement and misalignment errors
Pitch error	Measurement, misalignment and mechanical stabilization errors
Heave error	measured and induced heave errors
Refraction error	Sound speed error effects in range, beam angle, and non-orthogonal beam steering
Dynamic draught error	Static draught, squat, and loading changes
Water level error	Measurement and spatial prediction

Position error budget	
Positioning system error	
Latency error	
Relative transducer-sounding position error	Erroneous range and beam angle, roll, and measurements, refraction, and transducer misalignment errors
Heading error	Transducer yaw misalignment and gyro-compass measurement error
Relative antenna-transducer position error	Offset and attitude measurement errors

3.3.1 Calibration of the Coda Octopus|NovAtel F180R

The F180R is a self-calibrating system which uses an internal software algorithm for the evaluation. Nevertheless, the following information have to be entered and loaded into the system in forehand of the actual calibration procedure:

- Distance and orientation of the GNSS antenna baseline
- Offset of the primary GNSS antenna in relation to the IMU and the offset accuracy
- GNSS solution status

After saving the measured offsets, the calibration process can be initialized along with the beginning of the maneuvers performed with the vessel. These maneuvers must be of dynamic nature such as figure-of-eight pattern, circles or jerky starts and stops[14]. By means of this, the system is able to identify and evaluate three main aspects which affect the system output later on. In detail, these factors can be named as the rapid linear and rotational movements due to the vessel motion, the slow linear and rotational movements due to the earth rotation, and last but not least the slow linear and rotational movements which occur because of the uncontrollable drift recognized by the accelerometers and rate sensors inside the IMU. Depending on the size of the vessel, the calibration maneuvers should be actively performed for at least one hour to achieve for a successful completion. As mentioned earlier, an internal software algorithm is able to split these three signals to determine the final calibration offsets. The calibration state is reached if the actual attitude and heading accuracies are corresponding to the reference specifications shown in Table 3.7 (Coda Octopus Products Ltd., 2013).

Table 3.7: Calibration specification for the Coda Octopus|NovAtel F180R INS mounted with an antenna baseline distance of 2 m. The F180R is calibrated when the heading and attitude accuracies are equal to or better than the listed specifications (Coda Octopus Products Ltd., 2013).

GNSS status	Heading [°]	Attitude [°]	Position [m]	Velocity [$\frac{m}{s}$]
Stand alone	0.2	0.075	0.5	0.04
DGNSS	0.2	0.06	0.25	0.03

For the AL447 cruise, the calibration procedure had to be performed three times due to an obvious incorrectness of the determined input offsets and some problems with the installed GNSS antenna system. The first calibration maneuver was undertaken in the Kiel Fjord on October 20, 2014 and takes approximately two hours. As the results did not meet the required reference specifications, the procedure was initialized again on October 22, 2014 after a renewed survey of the offset from the primary GNSS antenna in relation to the IMU. As part of a port call in Frederikshavn, Denmark, on October 27, 2014, the offset measurement was repeated land-based with a total station and thereupon once again adjusted and successfully re-calibrated. This leads to the following final offsets displayed in Figure 3.10.

[14] The recommended calibration figure to allow the best possible result is the figure-of-eight pattern (Coda Octopus Products Ltd., 2013).

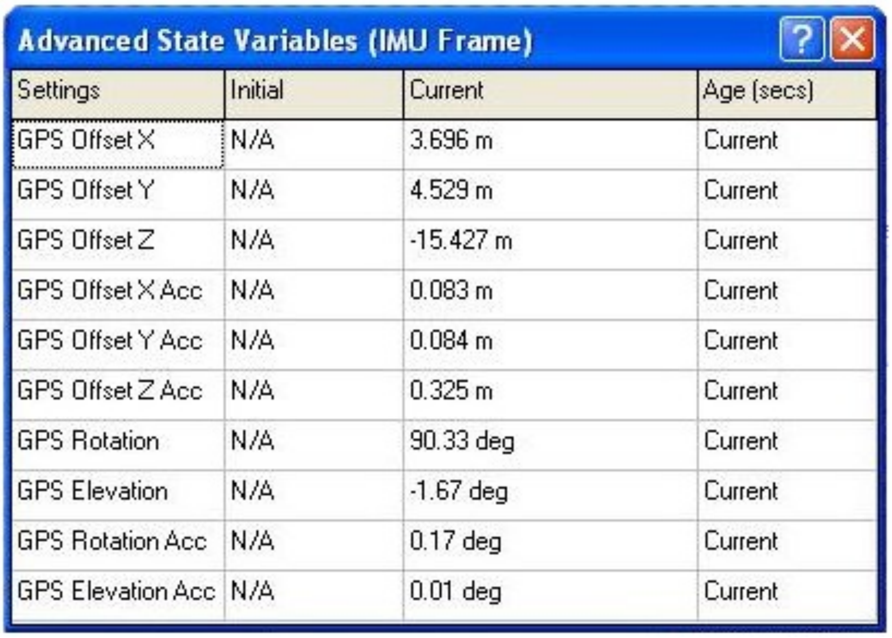

Advanced State Variables (IMU Frame)

Settings	Initial	Current	Age (secs)
GPS Offset X	N/A	3.696 m	Current
GPS Offset Y	N/A	4.529 m	Current
GPS Offset Z	N/A	-15.427 m	Current
GPS Offset X Acc	N/A	0.083 m	Current
GPS Offset Y Acc	N/A	0.084 m	Current
GPS Offset Z Acc	N/A	0.325 m	Current
GPS Rotation	N/A	90.33 deg	Current
GPS Elevation	N/A	-1.67 deg	Current
GPS Rotation Acc	N/A	0.17 deg	Current
GPS Elevation Acc	N/A	0.01 deg	Current

Figure 3.10: Advanced state variables after calibration of the Coda Octopus|NovAtel F180R. GNSS antenna offset in relation to the IMU, rotation, elevation and the accuracies related to the last-mentioned.

3.3.2 Calibration of the Kongsberg EM 2040C

To calibrate the EM 2040C MBES, a procedure formerly known as patch test is required after sensor installation in forehand of the actual survey. This test consists of different line pattern to detect systematic biases caused by measurement and misalignment errors as already indicated in Table 3.6 as well as to verify the performance of the installed system with respect to possible latency issues. With reference to Herlihy et al. (1989), certain conditions have to be fulfilled to ensure a reliable result. This especially affects the bathymetry of the survey area depending on the bias which should be determined. The most important is the morphology of the calibration area which should consist of a uniform slope and a flat area for the roll calibration. To facilitate the detection of a yaw bias, it is recommended that a clearly identifiable object is located within the calibration area. Figure 3.11 displays the line setup for each of the four named error source.

The latency check requires one line perpendicular to a slope, edge, or object which has to surveyed twice in the same direction but with varying survey speed. Commonly, the line is surveyed with normal survey speed in upslope direction and with reduced survey speed in downslope direction. As the pair of lines for pitch bias determination require the same seafloor morphology, the latency track surveyed with normal speed can be used. Supplementary, this line has to be surveyed again in opposite direction using normal vessel speed. For roll bias detection a flat surface is needed. A single line is surveyed in opposite directions with the same speed. Last but not least, two parallel, overlapping lines need to be recorded with the same survey speed to detect a possible yaw bias. In between the overlapping area, an object should be located (Godin, 1998).

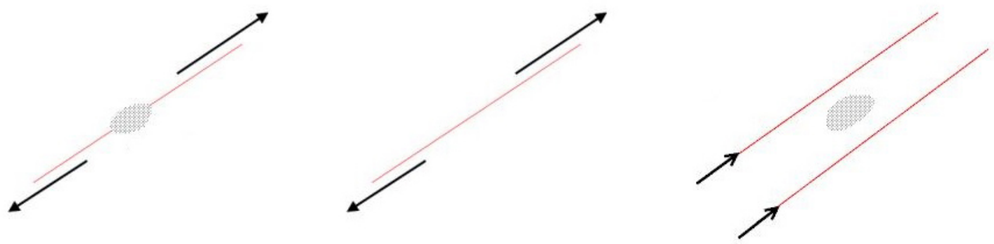

Figure 3.11: Calibration pattern for the MBES patch test. Spatial arrangement of the survey lines required for latency and pitch, roll, and yaw calibration (left to right). The greyish feature indicates that either a slope or an object is required (according to QPS, 2016).

After acquisition, the data can be evaluated using appropriate software. Possibly angular offsets appear in the form of a shift of the logged soundings, the adjustment of these detected offsets requires a geometrical solution. This is performed in a way that the considered soundings are manually placed on top of each other as it is exemplary shown in Figure 3.12.

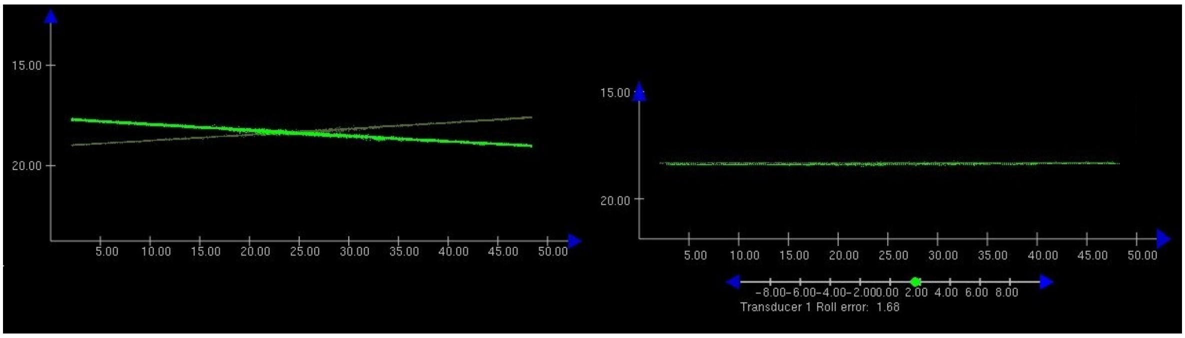

Figure 3.12: Calibration processing using CARIS HIPS and SIPS 8.1. Exemplary presentation with the example of the roll offset determination and the comparison between not adjusted (left) and adjusted (right) data.

For a computational determination of the different offsets, the following equations according to IHO (2005) can be used. Equation 3.1 describes the time delay δt, where Δx is the horizontal separation between the two sounding profiles near nadir and v_1 respectively v_2 represent the survey speed for both lines. Equation 3.2 describes the pitch offset $\delta\theta_P$, where Δx is the apparent offset of a depth on the same survey line in reciprocal directions and z represents the apparent depth offset between a point on the particular survey line. Equation 3.3 describes the roll offset $\delta\theta_R$, where Δz is the vertical displacement between the outer beams of the survey lines and Δy represents the half swath width. Equation 3.4 describes the yaw offset $\delta\alpha$, where Δx is the horizontal distance between the survey line and the object and ΔL represents the distance between the two survey lines (IHO, 2005).

$$\delta t = \frac{\Delta x}{v_2 - v_1} \tag{3.1}$$

$$\delta\theta_{\mathsf{P}} = tan^{\text{-1}} \cdot \frac{\Delta x}{2 \cdot z} \tag{3.2}$$

$$\delta\theta_{\mathsf{R}} = tan^{\text{-1}} \cdot \frac{\Delta z}{2 \cdot \Delta y} \tag{3.3}$$

$$\delta\alpha = tan^{\text{-1}} \cdot \frac{\Delta x}{\Delta L} \tag{3.4}$$

The line pattern for the patch test of the EM 2040C system on RV ALKOR was surveyed on October 25, 2014 in the Kiel Fjord. Recommended in advance by one of the technicians from Kongsberg Maritime AS, a latency calibration should not be performed due to the fact that the MBES already incorporates GNSS time synchronization and therefore no improvements could be expected. The performed patch test and the subsequent manual evaluation using CARIS HIPS and SIPS 8.1 results in the offsets listed in Table 3.8.

Table 3.8: Patch test results for the Kongsberg EM 2040C . Evaluation performed with CARIS HIPS and SIPS 8.1.

Calibration results	
Roll	1.681°
Pitch	-3.723°
Yaw	3.791°

4 Evaluation of data

Nowadays, a lot of different software solutions are available for the post-process of various measurement data. Especially for hydrographic and scientific surveys producing large volumes of data, the choice of the best suitable software solution is most important in consideration of an effective and efficient work strategy. Taking into consideration the logged data formats, the subsequently described software solutions as well as their underlying processes are presented by means of the appropriate processing workflow. Furthermore, the handling of the different acquired datasets is pointed out in detail.

4.1 Oceanographic water level data evaluation

The evaluation of movement processes like tides and wind driven currents form a part of the physical oceanography and directly affect the seafloor morphology due to sediment transports. These sediment transports in turn lead to burial processes which may affect ammunition bodies located on the seafloor. For monitoring purposes, the water level variations are logged with permanently installed tide gauges maintained by the responsible WSA. As the data is stored in comma-separated values, the choice of possible processing software or applications is only restricted by the data capacity depending on the monitoring period.

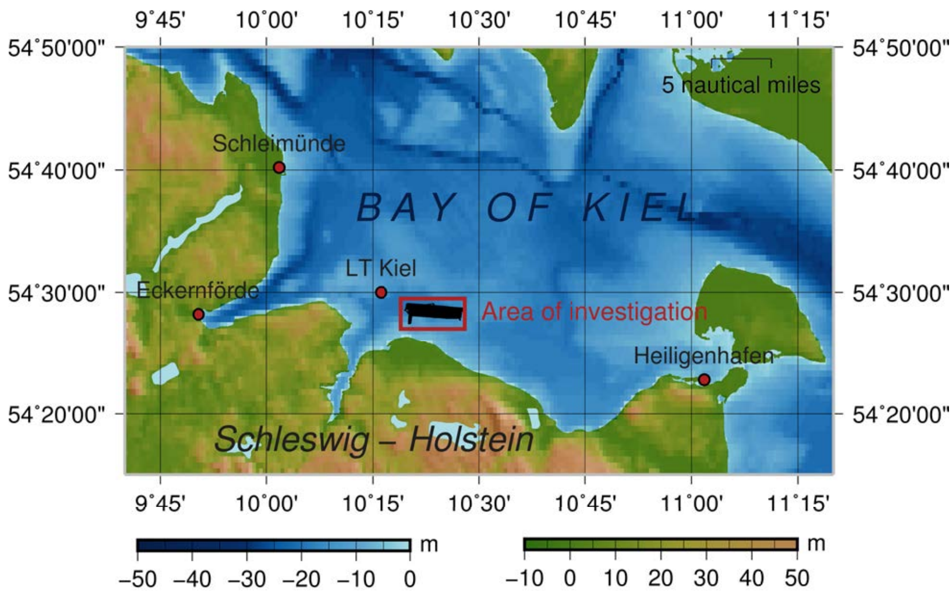

Figure 4.1: Location of tide gauges used for data evaluation. Mercator projection with global dataset GEBCO 2008 (30 arc-seconds) provided by GEBCO (2016) and tracklines of all conducted projects.

Provided by the WSA Lübeck, the water level variations monitored by the tide gauge stations displayed in Figure 4.1 were evaluated for the period from October 19, 2014 to November 06, 2014[15]. The data contain besides the time stamp given in central european time also the water level related to the current tide gauge datum. Normal height null (subsequently referred to as NHN) is specified as the general height reference. As all recorded survey data on the vessel use the coordinated universal time, the tide gauge data need to be shifted for one hour to ensure a correct allocation. For comparability of data, the water level need to be corrected by the tide gauge datum to obtain values related to NHN according to formula 4.1. These two adjustments were made using a usual spreadsheet software and the results were stored in a *.csv file for the actual evaluation.

$$Water\ level\ (NHN) = Measured\ value - Tide\ gauge\ datum \tag{4.1}$$

Having this done, the software MATLAB R2010a provided by MathWorks was used as it offers the possibility to both handle a larger amount of data and to display it in an appropriate manner. Focusing on numerical calculations, the high performance of MATLAB R2010a lead to short computing times which in turn is very important for an efficient work strategy.

To be able to perform a time series analysis, the range the water level data is alternating in as well as the mean water level is determined. For accuracy consideration, the correction, the variance, and the resulting standard deviation are calculated. With the help of this, the measurement uncertainty can be calculated for a confidence level of 95 %. In order to be able to give a more accurate statement of the water level fluctuation, a trend line has to be fitted in the raw data. Knowing the trend line parameters, the water level data can be adjusted with regard of the determined trend. To filter out possible temporal distributions and therefore to convert the continuous measurement into a periodical spectrum, a Fourier transformation is used. Having this done, different periods can be detected using a plot of the range frequency and the power of the Fourier analysis. The power of the Fourier analysis also gives evidence of the maximum changes in the water level. The mentioned periods are assigned to the time of occurrence by means of their maximum amplitude. Using this, the length of the respective period can be determined for further evaluations.

[15] It should be noted that the tide gauge station in Schleimünde has a malfunction during the first three days and therefore the data was transferred from the neighboring station

4.2 GNSS positioning evaluation

There are number of providers both for the acquisition and the processing of GNSS data. As satellite information are generally provided in a neutral file format, this opens up the choices between specific applications and programs which are not tied to a specific manufacturer. Regarding the processing of the position data gathered during the AL447 cruise, the possibility to work with the manufacturer-specific data format sets out the framework which leads to a very restricted freedom of choice.

The ability to process the manufacturer-specific output format *.rd is most restrictive as it is neither welcome nor possible to convert the encrypted data format into an independent one such as the receiver independent exchange format (subsequently known as RINEX)[16]. On this account, the software MOTION INSight Version 1.1.1 provided by Coda Octopus Products Ltd. which partly refers to the Waypoint GrafNav 8.3 software developed by NovAtel Inc. represents the only possible way for the application of subsequent GNSS corrections.

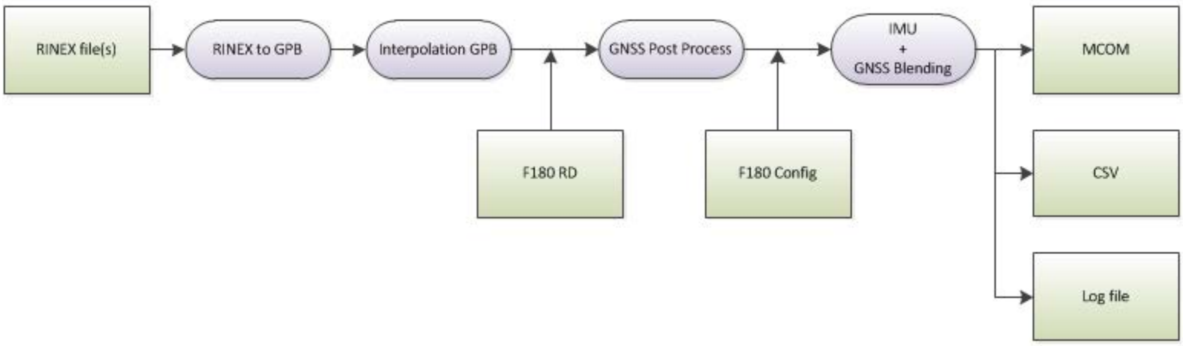

Figure 4.2: Processing workflow of the MOTION INSight 1.1.1 software application. General presentation of the workflow including the Waypoint GrafNav 8.3 processing steps (according to Coda Octopus Products Ltd., 2012).

Figure 4.2 provides a general overview of the workflow for the evaluation of the position data. The green rectangles indicate steps which need to be done by the user while the purple ellipses indicate the internal processing steps performed by the Waypoint GrafNav 8.3 software. As the GNSS base station data providing the SAPOS® correction information are logged in a RINEX file format containing the raw GNSS data, they need to be converted into the custom format *.gpb for further processing. This format contains for every tracked

[16] The RINEX format was developed for the purpose of GNSS data processing disregarding the manufacturer of the used instruments. Concentration on the essentials needed for post-processing, the format consists of three ASCII files containing observation data, navigation messages, and meteorological data (Gurtner, 2007).

satellite one position and measurement record for each epoch. The other information stored in the RINEX observation file remain unconsidered. Having done this internally conversion, the information can be interpolated. This step is necessary as the base station information provided by the German satellite positioning service SAPOS® are collected with 1 Hz whereas the F180R generates an output of 100 Hz. In order to be able to utilize the created files containing the SAPOS® correction data, the location of each station given in geographical coordinates and altitude relative to the WGS84 ellipsoid must be defined and assigned to the appropriate file. In this context, it should be mentioned that the height reference of the used base stations is given relative to the geodetic reference system from 1980 (referred to as GRS80) ellipsoid using the European terrestrial reference system from 1989 (referred to as ETRS89), but for practically relevant applications they can be assumed to be identical. In a next step, the *.rd files containing the raw data logged by the INS need to be selected and imported according to their time stamp in an ascending order. The adherence of the chronology is significant as, in case of disregarding this, the data may be erroneously merged. After the successful merging process, the raw GNSS data is extracted from the created *.rd file containing all INS data to be able to start the post processing (Coda Octopus Products Ltd., 2012). As the conducted survey produces kinematic data, the processing is done twice to be most effective. After processing the GNSS data in a chronological manner from the beginning to the end, a reverse processing is done. To obtain an optimal solution, both the forward and reverse processing solution are combined using variance weighting. This leads to an improvement of the overall accuracy as the solution with the greater estimated accuracy weighted more strongly. A graphical indication of the solution accuracy can be given by plotting the calculated differences between both solutions. It should be mentioned that the position given in latitude and longitude as well as the vertical component using the same weighting. The weight itself is computed using the following simple formula containing the variance Var (NovAtel Inc., 2010):

$$Weight = \frac{1}{Var} \tag{4.2}$$

Due to the fact that the MOTION INSight 1.1.1 software only falls back on the Waypoint GrafNav 8.3 software, the advanced processing settings cannot be adjusted by the user. The used default settings for both the forward and reverse processing as stated in the processing log can be found in Appendix B. The data used for the internal Kalman filter processing was the dual frequency carrier phase which implies the C/A code, the L1 Doppler phase shift, and the carrier phases of both frequencies L1 and L2. Processing in this dual frequency mode leads to an increased accuracy for longer baselines in comparison to the single frequency mode as it is possible to apply ionospheric corrections. The advanced real time kinematic (subsequently referred to as ARTK) option forces the computation of integer ambiguities for the kinematic trajectories. Using this technique, at least five satellites instead of four are required which leads to an achievable centimeter level accuracy. The acceptance to use GLONASS on the one hand maximizes the satellite usage, but on the other hand it can be disregarded as there is a GLONASS base station required to include them into the ARTK processing (NovAtel Inc., 2010).

To refer to the INS installed on the vessel, the configuration pursuant to the system has to be defined[17]. As this configuration is already done during the system setup on board of the vessel, it can be retrieved from the *.rd files. Prior to the final blending of IMU and GNSS data, the information written in the generated output files[18] and the general properties have to be selected. The system configuration is displayed in Table 4.1 (Coda Octopus Products Ltd., 2012):

Table 4.1: System configuration used within the MOTION INSight 1.1.1 software. The listed settings are extracted from the INS data.

System configuration	
Antenna separation	2.000 m
Primary antenna offset (x)	3.827 $\pm$ 0.048 m
Primary antenna offset (y)	4.551 $\pm$ 0.049 m
Primary antenna offset (z)	-15.593 $\pm$ 0.298 m
Antenna mounting angle (rotation)	90.00 $\pm$ 0.14°
Antenna mounting angle (elevation)	0.00 $\pm$ 0.01°
Vessel orientation (heading)	0.000°
Vessel orientation (pitch)	0.000°
Vessel orientation (roll)	0.000°
Remote lever arm offset (x)	0.000 m
Remote lever arm offset (y)	0.000 m
Remote lever arm offset (z)	0.000 m
Heave coupling reference	Alternating current
Altitude reference	Original

[17] The system configuration contains the following information: Antenna baseline, primary antenna offsets, antenna mounting angles (rotation and elevation), vessel orientation (heading, pitch, roll), remote leer arm offsets, heave coupling, and altitude reference (Coda Octopus Products Ltd., 2012)

[18] Fields that can be added to the *.csv output file are date, time of day, time from start, latitude, longitude, altitude, distance from start, velocity, speed, accelerations, heading, pitch, roll, angular rates, position accuracy, velocity accuracy, altitude accuracy, heading accuracy, pnline heave, iHeave date, iHeave time, iHeave status, and GNSS solution status (Coda Octopus Products Ltd., 2012).

Table 4.2 presents an overview of the eight conducted test series for the AL447 cruise. Due to a misunderstanding, it was only possible to evaluate the data for the last four days of the cruise. Therefore, each test series contains one project a day whereas it should be mentioned that there were required two projects for the third day because of a re-initialization of the system. The test series differ in the usage of different base stations providing the SAPOS® correction information. Geographically, the ensonified area is enclosed by the stations in Kiel, Bungsberg, and Westermarkelsdorf. Their location as well as the geographic spread of the base stations according to the survey area is displayed in Figure 4.3.

Table 4.2: Conducted projects for GNSS post processing. The checkmark indicates the use of base station correction data. If a station is not checked, it is not considered within the evaluation.

Project	SAPOS base stations		
	Kiel	Bungsberg	Westermarkelsdorf
1			
2	✓	✓	✓
3	✓		
4		✓	
5			✓
6	✓	✓	
7	✓		✓
8		✓	✓

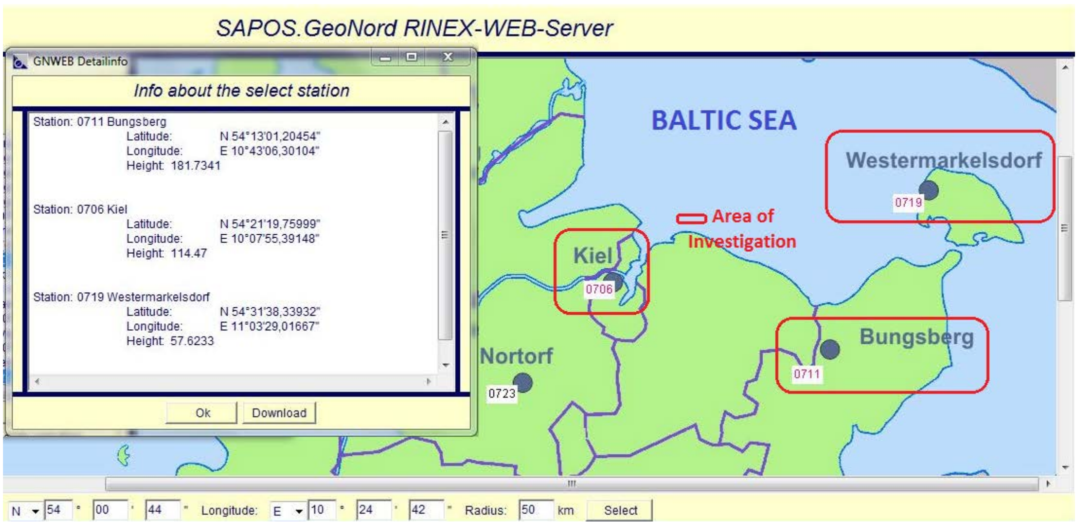

Figure 4.3: Location of the SAPOS base stations. Information about the base stations contain latitude, longitude, and height (SAPOS GeoNord, 2015).

As the input information stored in the *.rd files contain data logged with 100 Hz, the output of the post-processed data is likewise specified. All test series were performed with an alternating current heave coupling. By taking advantage of the physical effect causing a shift of the submitted waveform of $\frac{1}{3}$ of the pulse and therefore the removal of the direct current representing the average value of the waveform, the generated heave output has an average value of zero. Switching to the direct current heave coupling would have lead to an output of the absolute heave offset measured between the IMU and the seafloor (Coda Octopus Products Ltd., 2012, National Instruments, 2013).

4.3 Hydrographic data evaluation

The evaluation of the gathered MBES data includes the bathymetry and snippet backscatter intensities as well as the information describing the sediments shaping the seafloor. For this purpose, several software solutions are used. Especially for the processing of MBES data, the availability of a valid software license plays a decisive role as most of the common programs are licensed by the manufacturer.

4.3.1 Bathymetric data processing

To evaluate the bathymetric data, the software solution HIPS and SIPS 8.1 provided by CARIS was used[19]. This decision was made according to the experiences with the implemented post-processing procedures and therefore a reliable use in comparison to other software packages as MB System, Hypack, or QPS Qloud. In comparison to the positioning evaluation, the *.all file format was no limiting factor as this is a frequent output format.

The HIPS and SIPS 8.1 processing application is particularly used for the processing and analysis of bathymetric datasets in combination with sonar imagery and water column data. While the HIPS component of the processing software is made for the validation and cleaning of bathymetric datasets or water column data collected with MBES or SBES systems, the SIPS application covers the field of imagery data processing based on sonar surveys (CARIS, 2016). The processing is following a general workflow displayed in Figure 4.4. In combination with different other datasets like water level information collected by the surrounding tide gauge stations or the calculated sound velocity for the corresponding area, a digital terrain model can be generated to provide an impression of the seafloor morphology. All stages can

[19]During the processing time of this thesis, CARIS releases the new HIPS and SIPS 9.1 version in March 2016, but because of potential software bugs, it was consciously avoided to use this version.

be performed almost independently of each other. The working steps highlighted in red point out the presence of raw data, whereas the green part covers the georeferenced data. The blue colored part of the workflow indicates the processing of the georeferenced data as the last mandatory steps (CARIS, 2014).

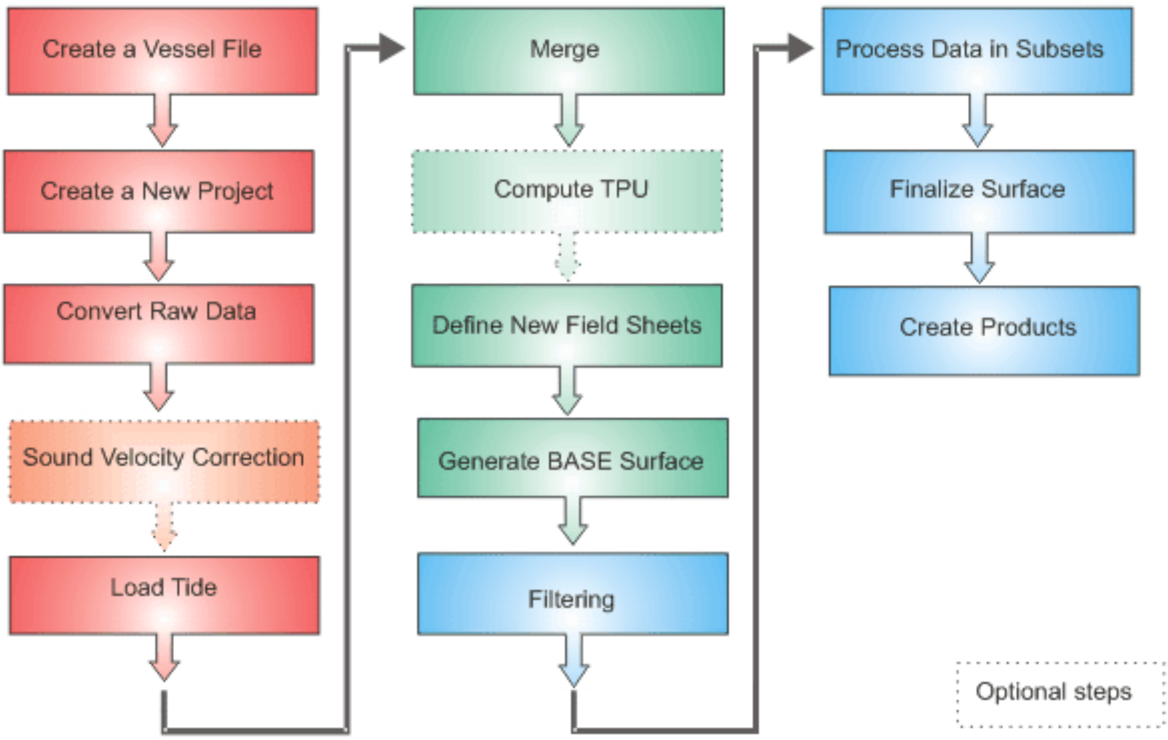

Figure 4.4: Processing workflow of the CARIS HIPS and SIPS 8.1 software application. General presentation of a MBES workflow using a CUBE filtering algorithm (according to CARIS, 2014).

To be able to process the collected data with respect to the equipped vessel and its dimensions shown in Figure 4.5 as well as to perform error estimations during the post-processing of the data, a vessel file need to be set up in advance. This file contains all information about the technical data of the vessel and also the location of the mounted sensors and their achievable accuracies (see Table 4.3). To remain compliant, the reference ellipsoid was defined as the WGS84, the reference point on the vessel was set to the IMU mounted in the moon pool., and the number of beams used by the MBES was defined as 400.

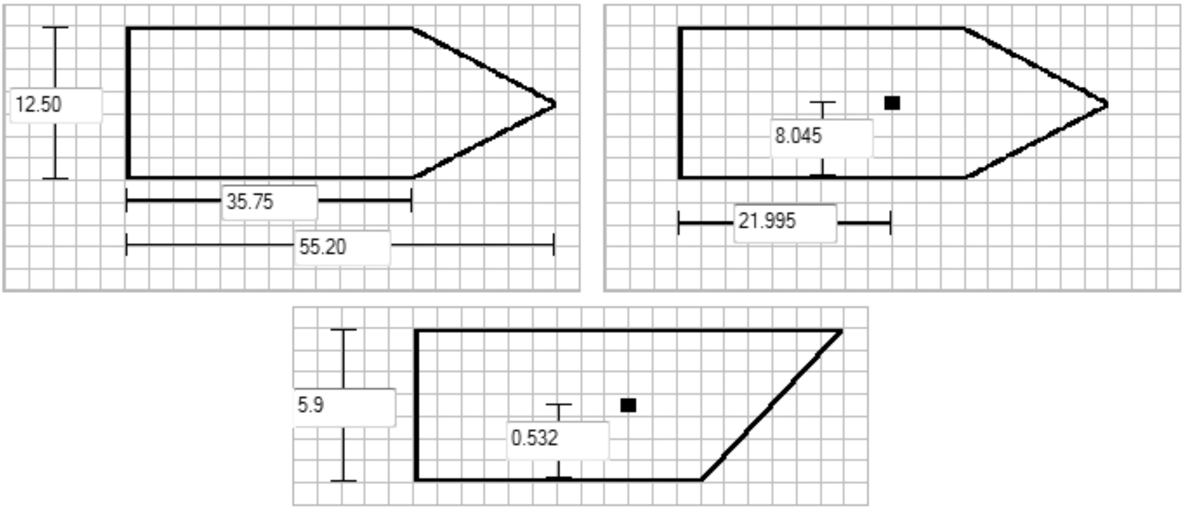

Figure 4.5: Dimensions of the RV ALKOR inserted to CARIS HIPS and SIPS 8.1. Plan view of the vessel shape (top left), plan view of the reference point (top right), and profile view of the vessel shape (bottom). Measurement units are given in [m].

Table 4.3: Offsets and standard deviations entered in the vessel file and considered in the TPU computation.

Offset		Standard deviation	
IMU to transducer (x)	0.410 m	Gyro of the IMU	0.050°
IMU to transducer (y)	0.000 m	Roll	0.025°
IMU to transducer (z)	0.732 m	Pitch	0.025°
GNSS to transducer (x)	3.403 m	Heave amplitude	5.000°
GNSS to transducer (y)	4.556 m	Heave	0.05 m
GNSS to transducer (z)	-16.416 m	GNSS	0.200 m
		Delta draft	0.03 m
		Tide	0.02 m
		Sound velocity	0.25 $\frac{m}{s}$
		Vessel speed	0.3 $\frac{m}{s}$

Using the information contained in this vessel file, a project can be set up with the indication of the exact day of the performed survey to ensure that all data was correctly assigned. Following the project setup, the data stored in the *.all files is converted into the internal HIPS data format. In this context the possibility to set a filter for apparent erroneous depth measurements is given, but to avoid data loss, this was not used for the considered data. In a next step, the tide information of the surrounded tide gauge stations are added to the lines converted into the project to correct the data for possible tide variances. As this is not equal to the general workflow it should be mentioned that it is common to apply the sound velocity correction taken from loaded sound velocity profiles. In view of the fact that the sound velocity was already applied during the data acquisition, this step is consciously avoid to not consider this correction two times. Not mentioned in the flowchart, but also an essential step is the validation of navigation and attitude information to detect jumps in the GNSS navigation signal and to do plausibility checks for the motion of the vessel, the heading data, and the applied sound velocity and tide data. With regard to the already mentioned problems with the INS in the beginning of the survey, a lot of GNSS jumps were detected in the data of the first two projects. While examining the other three projects, navigation errors were only found occasionally. Figure 4.6 offers an insight to the navigation validation and displays a comparison between erroneous data on the top and the corrected data in the bottom. Concerning the attitude information, no irregularities were found in the examined data. In addition, the depth measurements can be examined and validated for obviously incorrect soundings, but as the data examined in this study deals with objects located on the seafloor, this data cleaning has to be done with particular caution to not delete possible features of interest.

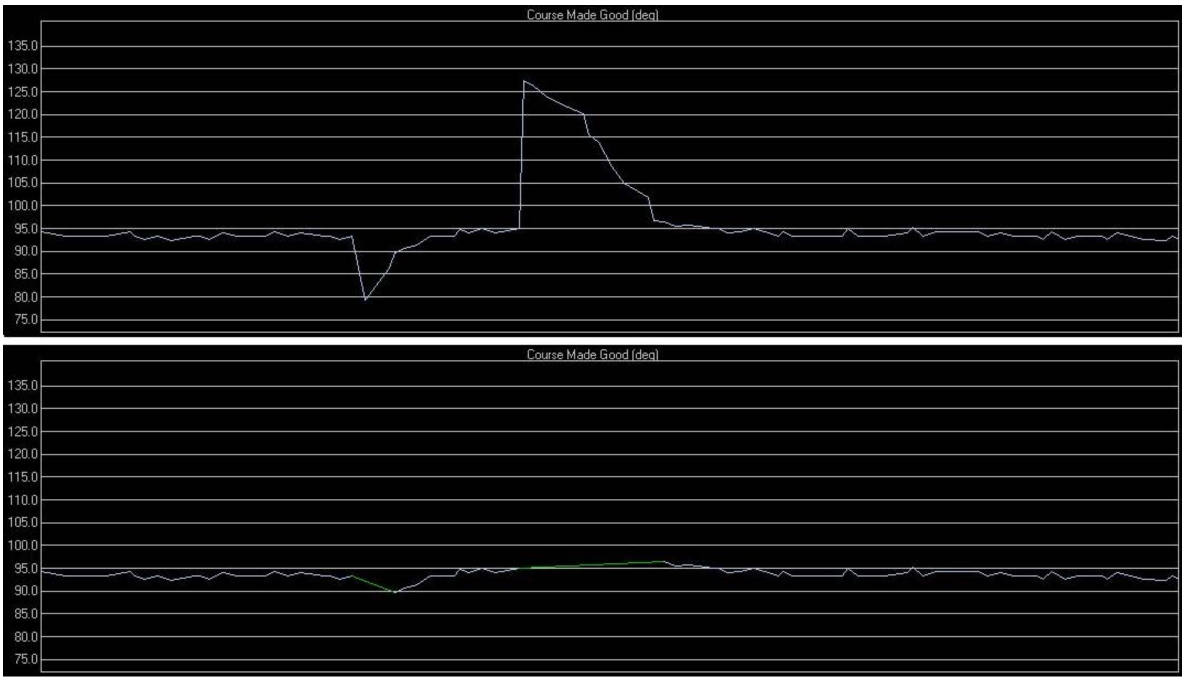

Figure 4.6: Validation of the navigation information using CARIS HIPS and SIPS 8.1. Comparisoon between erroneous data (top) and the corrected data (bottom).

Having applied all corrections and validations of data, the horizontal and vertical offset information defined to the vessel file can be combined to create geographically referenced positions and depths of the soundings. To be able to assess and give evidence for the measuring accuracy according to the minimal standards for hydrographic surveys defined in IHO (2008), the total propagated uncertainty (subsequently referred to as TPU) of each sounding can be computed. The TPU implies a horizontal error estimation as well as an estimation of the depth error. Both of them fell back on the following static and dynamic errors stored in the vessel file or linked in the real-time data (CARIS, 2014):

- navigation, heave, pitch, roll, and tide errors
- latency error estimate
- sensor offset estimate
- individual sonar model characteristics

Both the uncertainty associated with the depth and the one associated with the position value is scaled to 95% which corresponds to 1.96 times the standard deviation. The results can be informative about the grid size for the digital terrain model (subsequently referred to as DTM) which can be generated within a field sheet. To prevent possible confusions it should be mentioned that in CARIS software, the aforementioned DTM are named BASE surface[20]. During the setup of the field sheet, the horizontal resolution was defined as 0.02 m and the resolution of all depth values was stated as 0.001 m. Within this field sheet, a DTM can be created based on a CUBE[21] interpolation. For this, the resolution of 0.5 m indicating the distance between the surface values needs to be defined as well as the contributing horizontal and vertical uncertainties representing the IHO standard of the Special Order. In addition, the method used for disambiguation was defined as the density and locale approach which uses the hypothesis containing the most soundings and is consistent with the neighboring points. The formulated hypothesis has then to be validated until the final DTM can be computed.

[20] A Bathymetry Associated with Statistical Error surface is a georeferenced data image (CARIS, 2014) and can be equated with a DTM defined according to Miller and Laflamme (1958) as *"[...] a statistical representation of the continuous surface of the ground by a large number of selected points with known X, Y, Z coordinates in an arbitrary coordinate field."*.

[21] A Combined Uncertainty and Bathymetry Estimator surface uses multiple hypotheses for the representation of potential depth variances of the seafloor (CARIS, 2014).

4.3.2 Snippet backscatter processing

Even though the CARIS HIPS and SIPS 8.1 software package offers the possibility to process snippet backscatter information, it was decided to use the Geocoder application implemented in the QPS Fledermaus software in Version 7.3.6. It was justified by the fact that the practical implementation in comparison to the CARIS HIPS and SIPS 8.1 software does not require different intermediate stages which significantly affects the efficiency in the form of the required processing time.

The Geocoder toolbox implemented in QPS Fledermaus is particularly used for the analysis and visualization of MBES backscatter information. Thereby, it is irrelevant if these data are beam averaged or snippet time series data. It uses a stage-based processing which contributes to the already mentioned time efficiency. Figure 4.7 provides an overview of the general workflow this program is following (Interactive Visualization Systems Inc., 2011).

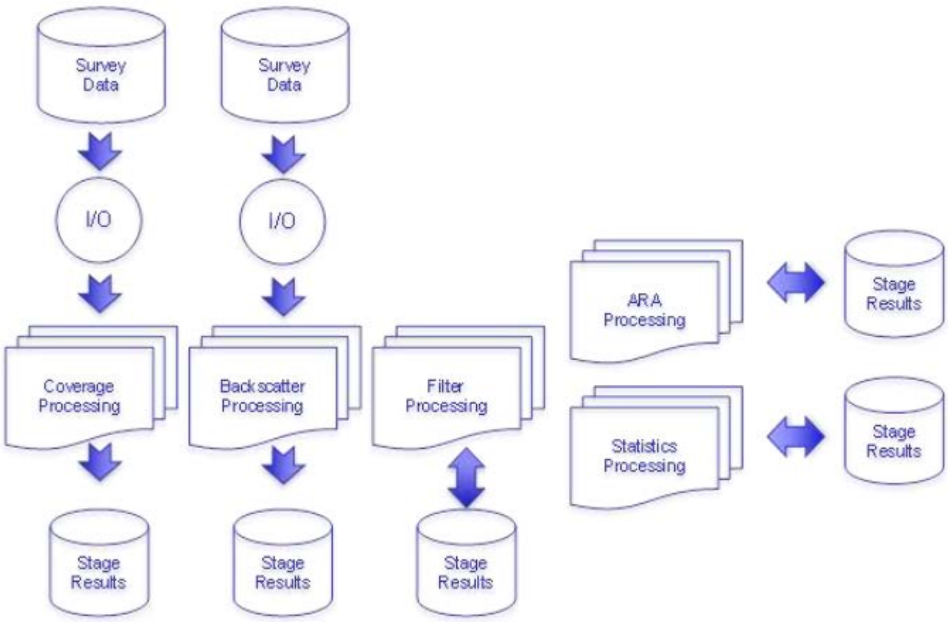

Figure 4.7: Processing workflow of the Fledermaus Geocoder toolbox. Split into five processing stages (squared) and three product stages indicated by the double arrow (Interactive Visualization Systems Inc., 2011).

Following the conversion of the input data, the files are internally indexed and the first of the five processing stages takes place. At this point, it should be mentioned that the stages of coverage, backscatter, and filter processing are depending on the output of the preceding processing step whereas the two independent stages shown in the right part of Figure 4.7 are only build on the first three parts. The coverage processing includes the readout of the swath extend for each beam and the stored navigation information. In addition, the meta data including the geographical extend and the sonar type were extracted. Using these meta data, the overall coverage can be computed. Having this done, the first of the three mentioned product stages can be performed including backscatter processing, filter processing and mosaic rendering. Based on the generated backscatter mosaic, it is possible to compute and render statistics and/or to process a sediment analysis named as the angle vs. range analysis (subsequently referred to as ARA) (Interactive Visualization Systems Inc., 2011). Based on this general workflow, the evaluation of the snippet backscatter information gathered during the AL447 cruise took place.

During the project setup, the horizontal output coordinate system WGS84 was chosen to ensure consistency with GNSS positioning and MBES processing. The definition of the horizontal input coordinate system was done during the import of the source files. Same as the output, the WGS84 was chosen. The determination of a vertical datum was not performed both for input and output. Before starting with the processing, several processing parameters were customized which will effect all processing stages. This includes the corrections listed in Table 4.4 and the entry of the specific sonar defaults as displayed in Figure 4.8:

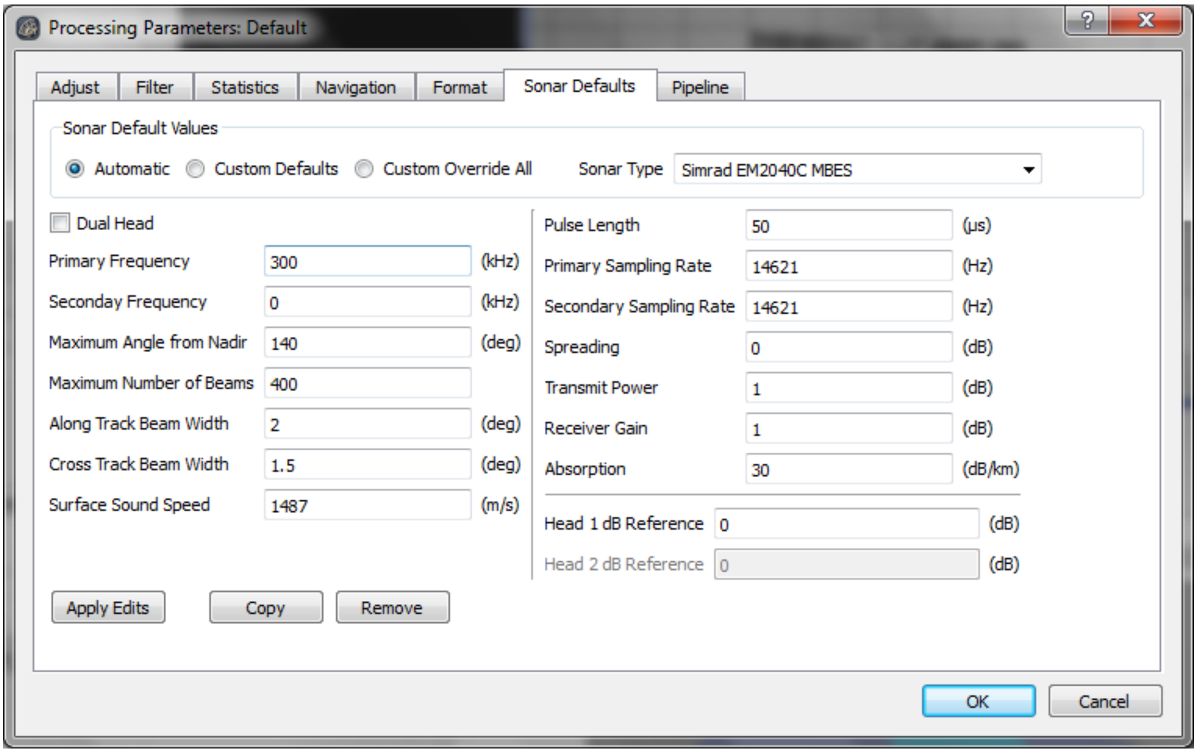

Figure 4.8: Sonar defaults of the EM 2040C representing the nominal parameters such as primary frequency, surface sound speed, and pulse length.

Table 4.4: Processing and mosaicing parameters in Fledermaus Geocoder.

Processing parameters	
Tx|Rx power gain correction	On
Beam pattern correction	On
AVG window size	300 pings
AVG correction algorithm	Flat
Heading spline smoothing	300

Mosaicing parameters	
Line blending	50 %
Mosaicing style	Blend

The Tx|Rx power gain correction represents the radiometric correction and is applied directly to the backscatter intensity values. Using this correction, all disturbances caused by the water column which influence the acoustic signal can be taken into account to enable the best estimate of the returned backscatter strength. The radiometric corrections are based on the sonar type and the topography of the seafloor. Geometrical properties were not affected with this kind of correction, but they are considered by the process of georeferencing. The beam pattern correction was applied, but only for using the default pattern file with all values set to zero. These zero values represent the difference between the current backscatter value and the theoretical model for each beam angle. Due to the fact that is was not possible to take sediment samples within the area of investigation, a specific beam pattern correction file based on ground truthing and grain size analysis could not be produced and therefore, nor further adjustments effecting the ARA were done. The angle varying gain (referred to as AVG) corrections are based on a window size describing a number of pings. Within this area using an algorithm stated as flat, an average intensity was calculated and all surrounding variations in the backscatter level of were smoothed out . In addition, the signal noise was reduced. With the application of the heading spline smoothing, a smooth curve was computed as an approximation of the available navigation with a skip factor of 300. This leads to the elimination of artifacts caused by the navigation linked with the backscatter information. The mosaicing parameters only effect the creation of the backscatter mosaics as they describe the handling of all single components which were linked together. A line blending of 50 % ensures an equal consideration of overlapping samples in the outer beams. With the mosaic style option blend, the pixels representing the nadir beam are blended with other overlapping pixels to create a homogeneous mosaicing result.

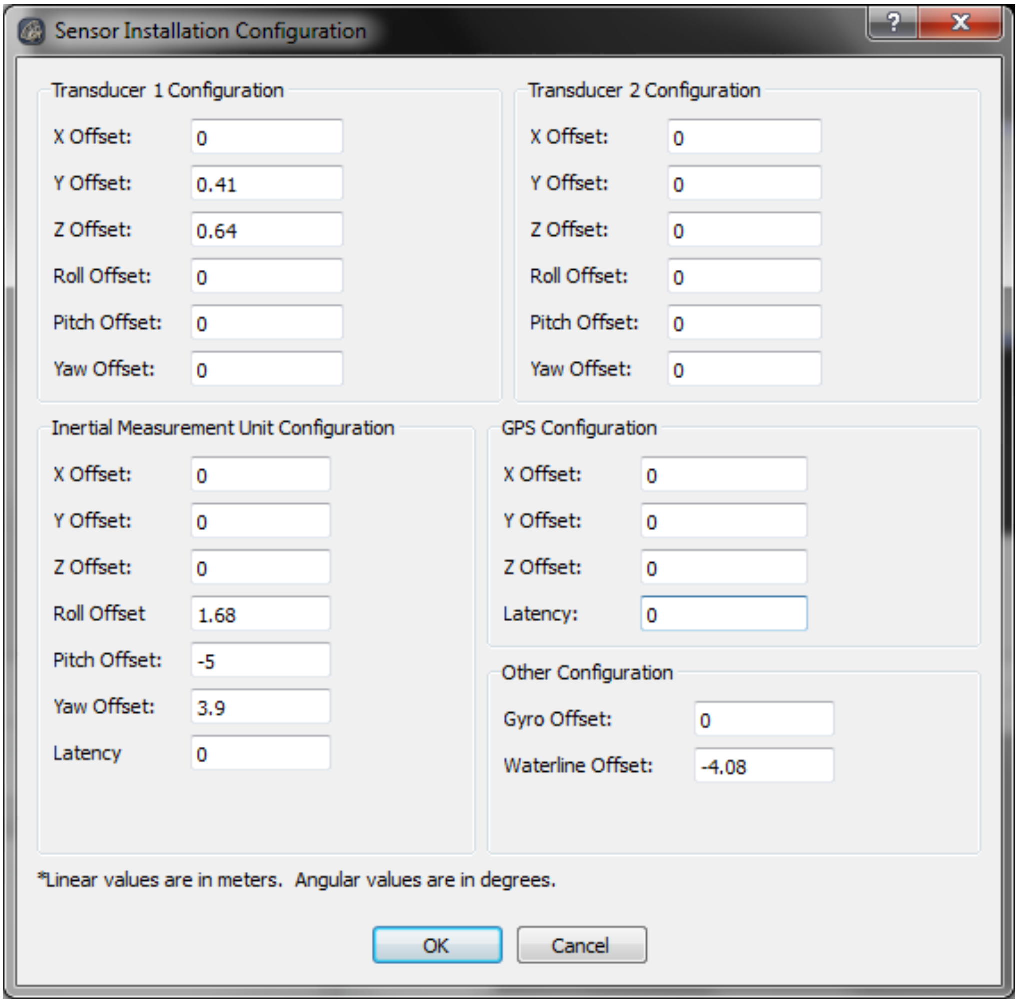

Figure 4.9: Sensor installation configuration of the EM 2040C. Offsets of the transducer and the IMU are internally stored in the *.all files, the waterline offset was entered according to previous measurements.

The sensor installation configuration affects the whole project and displays the specific sensor offsets which were determined in forehand of the conducted survey. In this case, the values were already stored internally in the input files and do not have to be edited except for the waterline offset which was entered manually. The offsets for the GPS configurations were consciously set to zero as they were already applied to the data during the acquisition process.

Having done all configurations, the creation of a backscatter mosaic can be performed starting with the computation of the pixel size given in a meter range. This indicates the resolution of the mosaic and is pre-computed, but still adjustable. The internal computation of the resolution represents an estimation based on the beam configuration shown in Figure 4.8 and the along-track coverage. Depending on the chosen mosaic area and the associated survey lines, this value can vary from 0.05 m up to 0.20 m, but due to the direct involvement of the pulse length stored in the beam configuration, it still provides a higher resolution in comparison to the resolution computed for the bathymetry. By clicking the appropriate button in the user interface, the system starts to build the mosaic as described in the beginning. After successful mosaicing, the histogram for the mosaic should be adjusted to ensure that no details will be lost due to blurry contrasts. This can be done by stretching the data range within the mosaic over the full colormap as displayed in Figure 4.10.

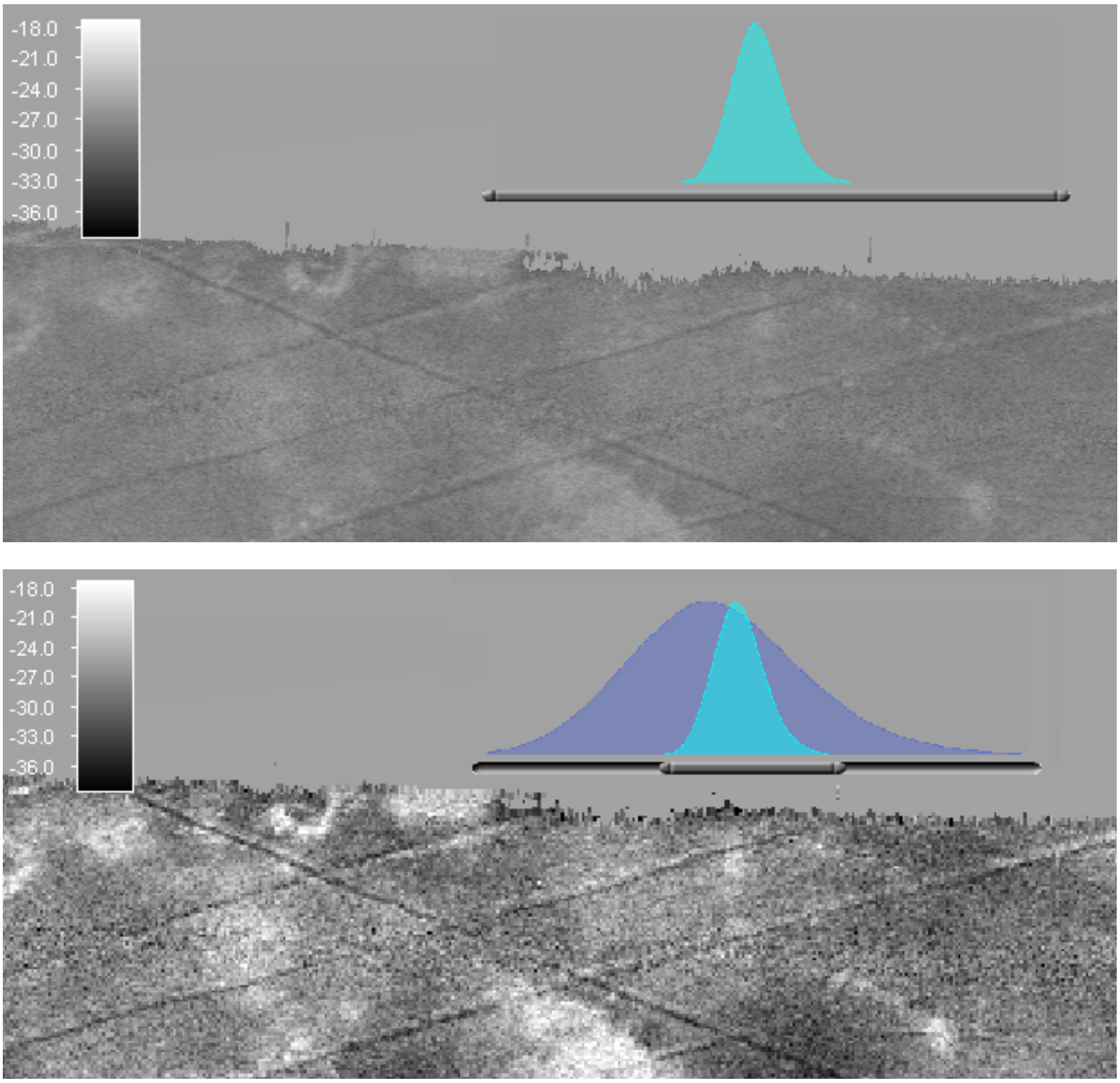

Figure 4.10: Histogram adjustment of the snippet backscatter mosaic. Mosaic without adjusted histogram (top) and after stretching the range (bottom). Dark colors represent low backscatter intensities, light colors indicate high backscatter intensities. Values given in dB.

Following this, a statistical grid can be computed. It includes maximum and minimum values as well as the variance of the computed mosaic and some other additional grids. As default, the resolution of the statistical layer amounts to 20 times the resolution of the snippet backscatter mosaic (Interactive Visualization Systems Inc., 2011). During the conducted evaluation, this leads to a grid resolution of 1.00 m based on a snippet backscatter image with a pixel size of 0.05 m, for the overview grid with a pixel size of 0.50 m the resolution is accordingly bigger.

Besides the already mentioned output, the ARA can be performed to characterize the seafloor in consideration of a comparison of backscatter intensities. The analysis is based on the mathematical Jackson Model which uses the grazing angle and the respective backscatter intensity for the computation of an acoustic response curve. This is done for different types of sediment and different frequencies. Through the comparison of the modeled curve and the observed angular response, the closest possible approximation can be determined which in turn provides information concerning the sediment properties named as grain size, density, or roughness. As the characterization process revert to the snippet backscatter information, the identical influencing factors like the calibration of the system and the utilized radiometric corrections apply to this results. Additional to the mentioned influences, a survey area located in shallow waters can contribute to a good and accurate characterization (Interactive Visualization Systems Inc., 2011). In the absence of a sediment probe within the area of investigation, it was waived to perform a beam pattern correction to obtain more accurate ARA results. Hence, no further default settings have to be done in forehand of the actual computation. Concerning the resolution it was decided to use a 1.00 m grid as otherwise, a nonexisting accuracy of the resulting image is duped.

4.3.3 Sediment evaluation

For the evaluation of the present sediments on and below the seafloor, the software application ISE 2.95 provided by Innomar Technologie GmbH was used. Even if there is the possibility to convert the manufacturer-specific output format *.ses into a general *.ascii file format, the choice was made due to the fact that this software is well-known and therefore a smooth operation is ensured.

The ISE 2.95 software offers the possibility to correct the gathered SBP information with regard to tide, vessel motion of GNSS data. Furthermore, it gives possibility to digitize and calculate occurring sedimentary layers to grasp an idea about the sediment thickness and, mostly in combination with additional information like sediment probes or density profiles, the type of sediment (Innomar Technologie GmbH, 2009b). As the necessity of the mentioned processing steps strongly depends on the input data, there is no general underlying workflow like in CARIS HIPS and SIPS 8.1 or QPS Fledermaus Geocoder 7.3.6 which has to be taken into account.

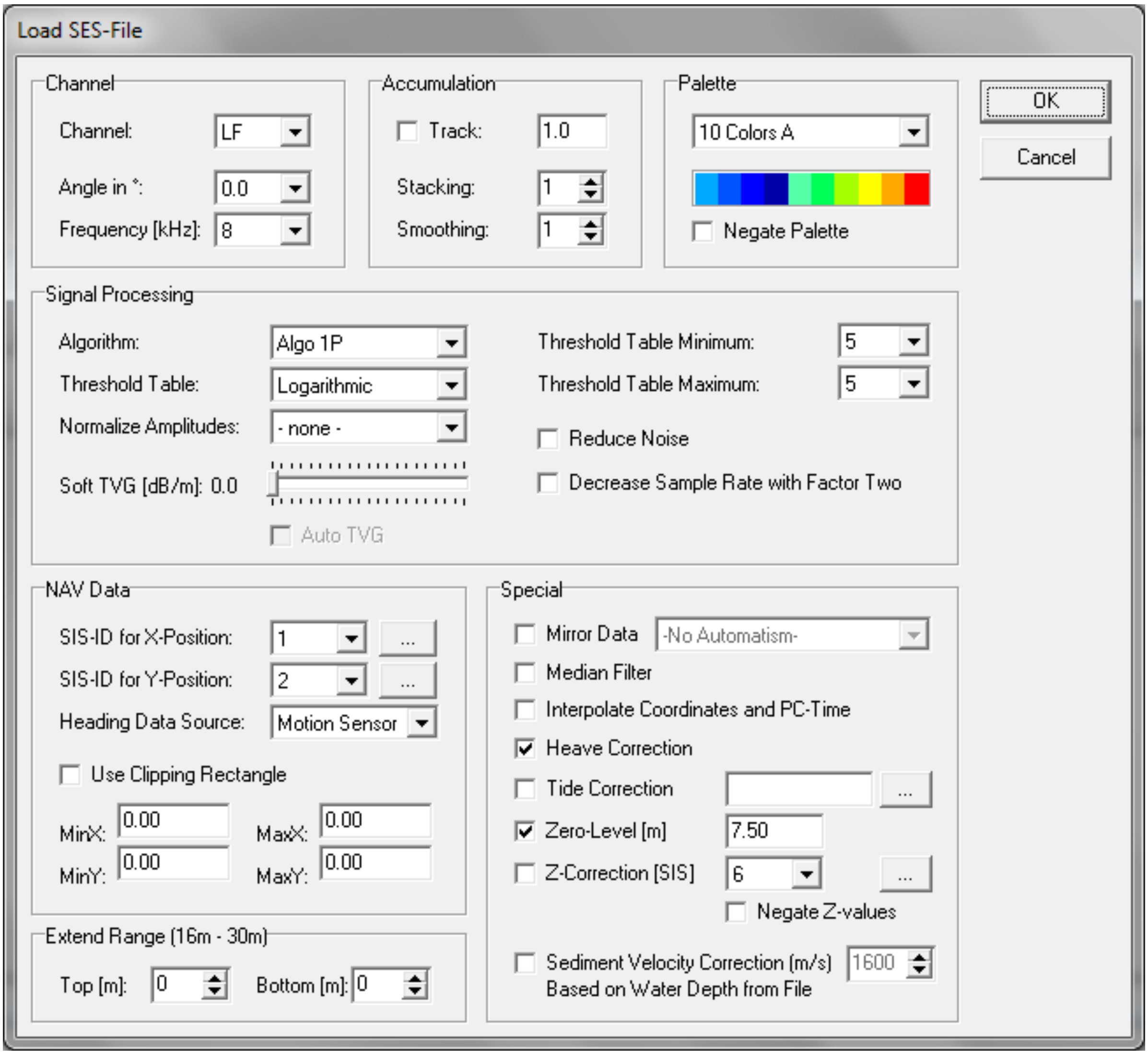

Figure 4.11: Import dialog for a *.ses data file in ISE 2.95. Configuration options effecting channel, accumulation, color palette, signal processing, navigation data, range extension, and additional settings.

Figure 4.11 shows the dialog containing all information needed for the input of a file. In comparison to the already introduced software applications, it is only possible to process one file at a time which makes it necessary to repeat the settings for each line. Besides some settings effecting the pictorial representation of data, the displayed frequency has to be chosen. Since the SES-2000 standard is a parametric SBP, it can be distinguished between the high and the low frequency whereas the seafloor penetrating low frequency is preferable. The parameters effecting the signal processing like the accumulation can be selected which is very useful to create a horizontally scaled output, but it requires that the input data is already marked with coordinates. Settings concerning the processing algorithm or the threshold for noise reduction are possible, but in this case, the default values were used. The same applies to the adjustment of navigation data as the GNSS position data was not directly combined with the SBP during the data acquisition. In a last step, different special settings can be made which effect the display of the data including several corrections. Due to the fact, that the collected data has a constant height offset of 7.50 m in comparison to the MBES data, a new zero level was applied for alignment.

After importing the *.ses file, the general ping information is available. This includes the operation frequency of 8 kHz, the distance of 54.21 m between two pulses, the pulse length of 1 sec, and the gain used for high and low frequency which amounts to 16 dB for the low and 3 dB for the high frequency. In addition, the used sound velocity of 1513 $\frac{m}{s}$ is displayed. During the acquisition, no SVP information were collected, so a subsequent adjustment of the value is not possible as it requires an appropriate sound velocity profile. As well as it is possible to perform corrections of the sound velocity, the GNSS positioning data can be imported during the processing. An identical time basis sets out the framework for this operation. Unfortunately, the PC time was synchronized with the logged GNSS time while surveying. This leads to an incorrectness of both time stamps which makes a subsequent import of the position data impossible.

Considering these circumstances, it was decided to skip further processing steps as it is not possible to exactly allocate the data profiles. Thus, the sediment profiles are considered exemplary to support the conclusions based on the other datasets.

4.4 German Navy Tactical Map

The Federal Office Bundeswehr Equipment, Information Technology and In-Service Support (subsequently referred to as BAAINBw) was founded in 2012 and has its main task in the equipment of the Bundeswehr. One department of the BAAINBw is the Bundeswehr Technical Center for Ships ans Naval Weapons, Maritime Technology and Research (subsequently referred to as WTD71) with several branches including one based is Kiel (BAAINBw, 2016). The Tactical Map Version 5.1.1.0 provided by the WTD71 in Kiel graphically represents information concerning the underwater situation and contamination which are collected within the task field of the WTD71.
Regarding all graphical presentations in this section as well as in the following chapter it should be mentioned in forehand that the indication of all geographical coordinates is consciously waived as they represent internal information bound by the obligation of secrecy.

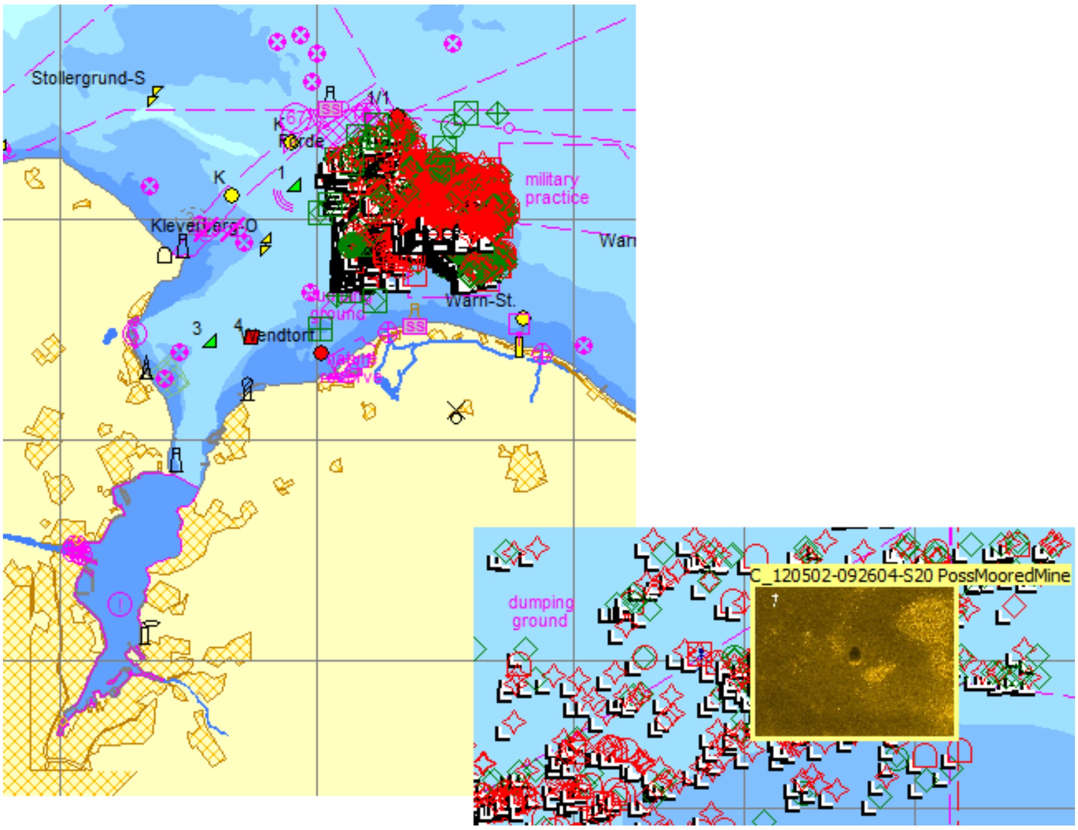

Figure 4.12: Display provided by the Tactical Map. The left part shows a general overview of all contained graphical information, the right part indicates the differentiation between objects and the mouseover function.

Figure 4.12 gives an insight into the display of the stored data. A nautical chart serves the background data. The magenta lines shown in the overview on the left part of the figure highlight designated areas as dumping sites or zones especially established for military purposes. The large scale excerpt shows detected point objects. Locations signed with a green symbol indicate harmless objects such as rocks, ropes or anchors, whereas a red symbol refers to potential risks. Through the shape of the symbol it is possible to distinguish between mines, drums or other identified objects.

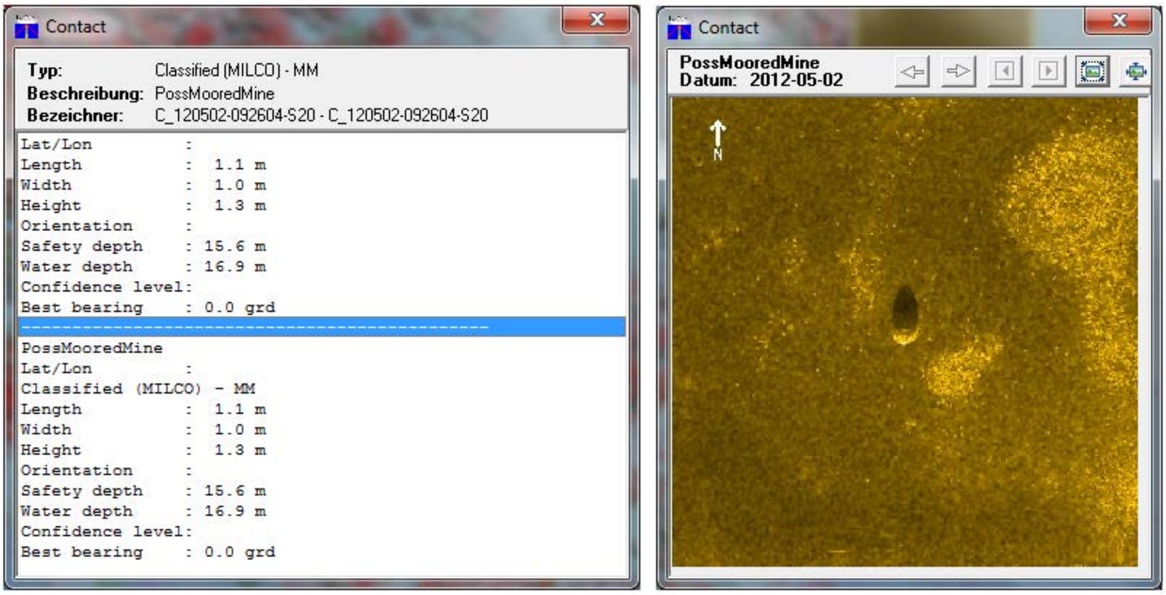

Figure 4.13: Stored object information in the Tactical Map. Description of position, dimensions and type of the object (left) and sonar image (right). For secrecy, the position information is blanked out.

In each object, a sonar image and a related description is linked. A small version of the saved image is also connected to a mouseover function, however the description of the object is only available by targeted selection. Figure 4.13 exemplary shows an identified contact. Besides information about type of the object, the description contains the geographical position given in latitude and longitude as well as the dimensions of the objects. Additionally, statements concerning the water depth and the nautical depth are given. The graphical presentation gives evidence of the object type and the date it was located on-site. As also pointed out by Kretschmer and Jans (2016), the images used for the comparison were gathered using the AUV HUGIN manufactured by Kongsberg Maritime AS equipped with the SAS system HISAS. Using these data, a kind of ground truthing for the collected snippet backscatter images can be performed.

5 Evaluation results and discussion of data

Having processed the data, the results need to be presented and evaluated. In this context, the consideration may not just be done individually, but also in the context of the entire results to be able to point out connections and interdependencies. At the beginning, the evaluated tide gauge observations are presented to indicate the influence of the water level variations to the bathymetric and snippet backscatter data. Furthermore, the results of the GNSS post-processing are evaluated in regards to the attainable precision using different GNSS solutions. This is done particularly in view of the economic efficiency and its associated costs. Subsequently, all hydrographic results are presented and evaluated. To conclude, a comparison between previously applied survey methods for ammunition detection and the feasability of snippet backscatter information is made to emphasize the advantages and drawbacks. Moreover, the current sediment situation is interpreted to assess the possibility of sediment displacement which may lead to the burying of ammunition bodies in the future.

5.1 Oceanographic data interpretation

Regarding the tide gauge variations during the observation period shown in Figure 5.1, only small periodical shifts due to the different localities are recognizable. The magenta hydrograph of the water level logged in Heiligenhafen stands out in comparison to the ones representing the data from Schleimünde, Eckernförde and LT Kiel which leads to the fact that this one is the only station located in the east of the investigated area. Obviously, the tidal curves are not periodical as they are for the North Sea due to the fact that the Baltic Sea appears as a brackish water basin which is more dominated by internal standing waves. Nevertheless, the water level fluctuates around 120 cm as indicated in Table 5.1.

Table 5.1: Water level range and mean level for the surrounding tide gauge stations. Water level information is given in relation to NHN.

Tide gauge station	Water level range [cm]	Mean water level [cm]
Schleimünde	119	-4
Eckernförde	120	-4
LT Kiel	118	-3
Heiligenhafen	123	-1

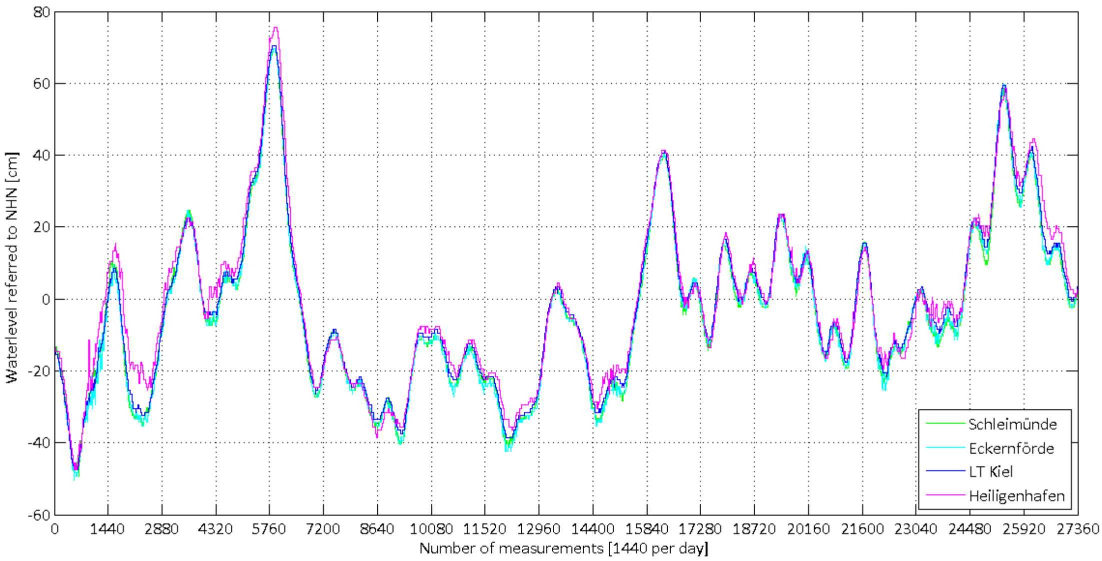

Figure 5.1: Water level variations logged at tide gauge stations around the dumping site. Water level referred to NHN over a time of 19 days. Data source: WSA Lübeck. The full size figure can be found in Appendix A.

The fact that the water in the Baltic Sea does not fluctuate in a periodical manner is also reflected in the results of the conducted Fourier transformation. In total, there are 21 fluctuation periods of different frequencies detected and summarized in Table 5.2.

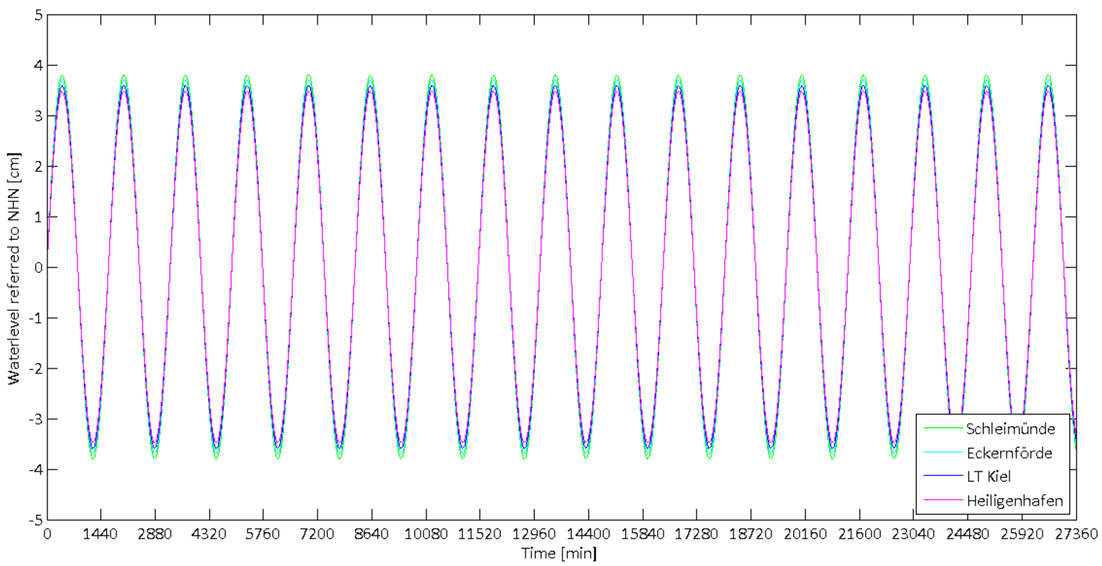

Figure 5.2: Frequency of a detected first order seiche. Oscillation system: Western Baltic Sea - Gulf of Finland. The full size figure can be found in Appendix A.

Table 5.2: Frequency and amplitude of the detected water level fluctuations. Frequency f [h] and amplitude $\hat{x}$ for each of the four investigated tide gauge stations.

Schleimünde		Eckernförde		LT Kiel		Heiligenhafen	
f [h]	$\hat{x}$ [cm]	f [h]	$\hat{x}$ [cm]	f [h]	$\hat{x}$ [cm]	f [h]	$\hat{x}$ [cm]
182.0	±16	182.0	±17	182.0	±17	182.0	±18
109.2	±11	109.2	±11	109.2	±11	109.2	±11
78.0	±7	78.0	±7	78.0	±7	78.0	±8
54.6	±7	54.6	±7	54.6	±7	54.6	±7
42.0	±8	42.0	±7	42.0	±7	42.0	±7
34.1	±9	34.1	±8	34.1	±9	34.1	±9
27.3	±4	27.3	±4	27.3	±4	27.3	±4
						24.8	±3
23.7	±3	23.7	±3	23.7	±3		
21.8	±3	21.8	±3	21.8	±2	21.8	±2
20.2	±2	20.2	±2	20.2	±2	20.2	±2
18.8	±2	18.8	±2	18.8	±2	18.8	±1
17.6	±1	17.6	±1				
				17.1	±1	17.1	±1
15.6	±2	15.6	±2	15.6	±2		
						15.2	±1
14.0	±2	14.0	±2	14.0	±2	14.0	±2
12.4	±5	12.4	±5	12.4	±5	12.4	±5
11.9	±2	11.9	±2	11.9	±2	11.9	±2
11.4	±1	11.4	±1				
						11.0	±1

A comparison of the computed values with the typical and known oscillations stated in the second chapter, Table 2.1 shows a correlation with the first order seiche occurring in the oscillation system bounded by the Western Baltic Sea and the Gulf of Finland. Figure 5.2 displays the period for this detected water level fluctuation over the whole survey period. This main standing wave is, as already indicated in the second chapter, well supported by the atmospheric influences of wind and air pressure and therefore clearly detectable. The further detected periods cannot directly be assigned, but it is noteworthy that the detected periods with a frequency of 54.6 hours and 109.2 hours are multiples of the assigned first order seiche. In conjunction with this, the amplitude increases with the frequency by 75 % respectively 58 %. Regarding the other oscillations it might be reasonably assumed that they represent short period seiches as appearing in small Bodden and Fjords. Especially the three individually occurring water level fluctuations observed for the tide gauge in Heiligenhafen lead to this conclusion. To give evidence of this assumption, further long term investigations and evaluations are necessary to exclude uniqueless events.

Regarding the water level changes caused by the oscillations, it can be said that they will not decisively effect the gathered MBES data. The maximum fluctuation is determined to $\pm$ 17 cm which is, in comparison to the amplitude of the known Baltic Sea seiches, relatively small. Having in mind that the mentioned first order seiches may lead to changes in the water level of up to one meter it can be implied that the unknown detected changes can be reduced to short term meteorological impacts.

5.2 GNSS positioning interpretation

To evaluate the general accuracy of GNSS positioning, it has to be distinguished between the accuracy of the pseudo range measurement and the carrier phase accuracy. While the carrier phase evaluation for kinematic observations providing only one set of data is quite complex, a general statement of the attainable accuracy can be given. According to Bauer (2011), the accuracy of a continuous kinematic observation can be stated to 1-2 dm. The pseudo range measurement is comprised of several error influences summarized in Table 5.3 (Bauer, 2011). However, it should be mentioned that the stated values are, just as the stated carrier phase accuracy, a rough assessment and improvable by the choice of the used equipment and applied survey method. According to the manufacturer specifications, the mounted system

Table 5.3: Error budget of a GNSS survey. Signal dispersion containing ionosphere, troposphere, and multipath effects. Receiver errors containing noise and instrumental delays (according to Bauer, 2011).

GNSS error source	
User range error	1 - 2 m
Ionosphere (two frequencies)	cm - dm
Troposphere	0.5 m
Multipath effect	1 m
Noise	0.5 m
Instrumental delay	dm - m

is able to derive a positional accuracy of 0.5 m up to 4.0 m for the absolute positioning and 20 cm up to 1 cm when using DGNSS (Coda Octopus Ltd., 2006). These specifications are given according to the circular error probable (subsequently referred to as CEP) as an indicator of accuracy, what implies a statistical significance of 50%. This for navigational purposes convenient circular approximation of the known error ellipses assumes a circular Gaussian distribution and represents the extensive accuracy. It should be mentioned that the CEP is only valid for Cartesian coordinates (Bauer, 2011).

The evaluation described in the previous chapter provides the accuracy of both latitude and longitude position which were used for the calculation of the horizontal accuracy consideration. Table 5.4 summarizes the computed the mean horizontal accuracy values for all conducted test series. In addition, the ranges of the latitude and longitude accuracy is indicated based on the Gaussian distribution for a statistical significance of 96%. To provide a better overview, the results for the first two test series are subsequently depicted and explained.

Table 5.4: Results of the GNSS postprocessing. Number of the test series according to Table 4.2, range of the latitude and longitude accuracy [m], mean position accuracy [m], and the range of the confidence interval (96 %) [m].

Test series	Lat accuracy [m]	Lon accuracy [m]	Position accuracy [m]	Confidence interval [m]
1	0.451 ... 3.553	0.449 ... 2.960	0.678	0.545 ... 0.812
2	0.055 ... 2.023	0.054 ... 1.900	0.086	-0.003 ... 0.176
3	0.055 ... 2.040	0.054 ... 1.906	0.089	-0.011 ... 0.189
4	0.056 ... 3.422	0.055 ... 2.806	0.091	-0.023 ... 0.205
5	0.056 ... 3.553	0.055 ... 2.960	0.156	-0.213 ... 0.525
6	0.055 ... 2.026	0.054 ... 1.898	0.086	0.004 ... 0.168
7	0.056 ... 2.031	0.055 ... 1.900	0.087	0.004 ... 0.169
8	0.053 ... 3.429	0.052 ... 2.807	0.091	-0.060 ... 0.241

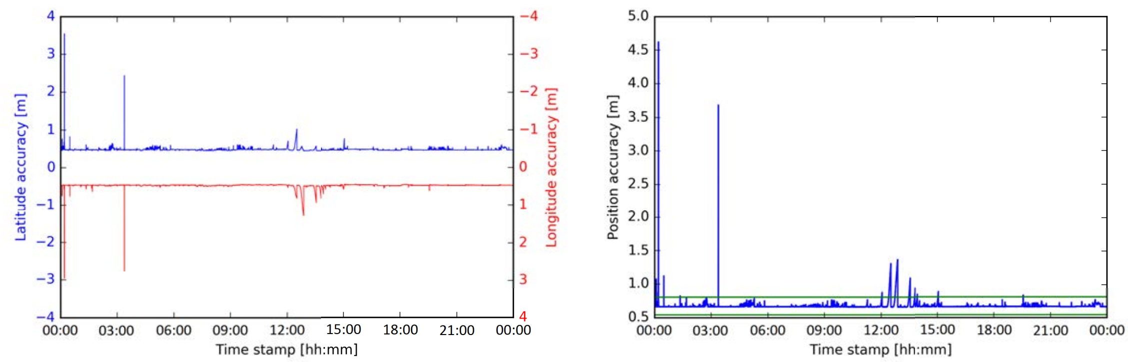

Figure 5.3: Position accuracy for absolute GNSS positioning. Accuracy for latitude and longitude position [m] over a period of 24 hours (left) and horizontal position accuracy [m] (right). The green horizontal lines indicate the computed confidence interval.

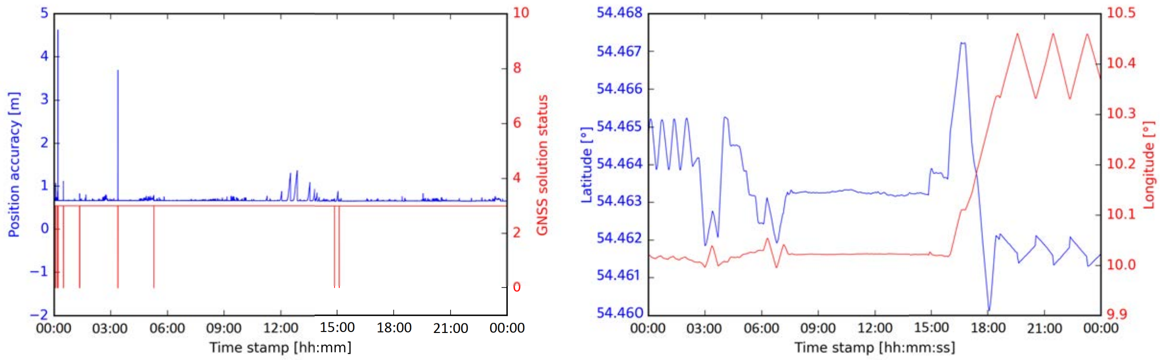

Figure 5.4: GNSS solution status and bearing. Horizontal position accuracy [m] in relation to the GNSS status over a period of 24 hours (left) and the bearing of the vessel shown in latitude and longitude (right).

On the left side of Figure 5.3, the accuracy of both the latitude and longitude position component of the absolute positioning over an observation period of 24 hours is shown. The latitude accuracy displayed by the blue graph is ranging between 0.451 m and 3.553 m, the longitude accuracy shown in red covers a range from 0.449 m to 2.960 m. Obviously, there are two outliers shortly after midnight and 03:00 AM. Between noon and 03:00 PM, an accumulation of less accurate measures occurs which is particularly noticeable in the longitude accuracy. With regard to the GNSS solution status as shown on the left side in Figure 5.4, the reason for this cannot be seen in a loss of the GNSS signal indicated by a change from solution status 3 representing the absolute positioning to status 0. A possible reason for this could be a change in the atmospheric layers or the result of shadowing effects due to the direction of motion. With regard to the right side of Figure 5.4 it can be seen that the vessel did not noticeable move from 07:00 AM to 03:00 PM which leads to the conclusion that the mentioned shadowing effects can be ruled out as the accumulation of less accurate measures occurs only in the mentioned time frame. While errors caused by the ionosphere are mostly compensated within the GNSS antenna, the troposphere is affected by the prevailing weather conditions. The change of the water vapor content in relation to the daytime is well-known and its effect can only be taken into consideration by a predicted approximation. The resulting error as well as all other influences can be additionally amplified by the satellite constellation which also changes during the day due to their constant orbits. For evaluation, the knowledge of the positional or horizontal dilution of precision (referred to as PDOP respectively HDOP) stored in the NMEA 0183 data file would be necessary, but as these information was not available, no further studies were conducted. To the right of Figure 5.3, the resulting horizontal accuracy is presented. The green lines indicate the confidence level the accuracy is alternating in. Its boundaries are stated as 0.545 m and 0.812 m.

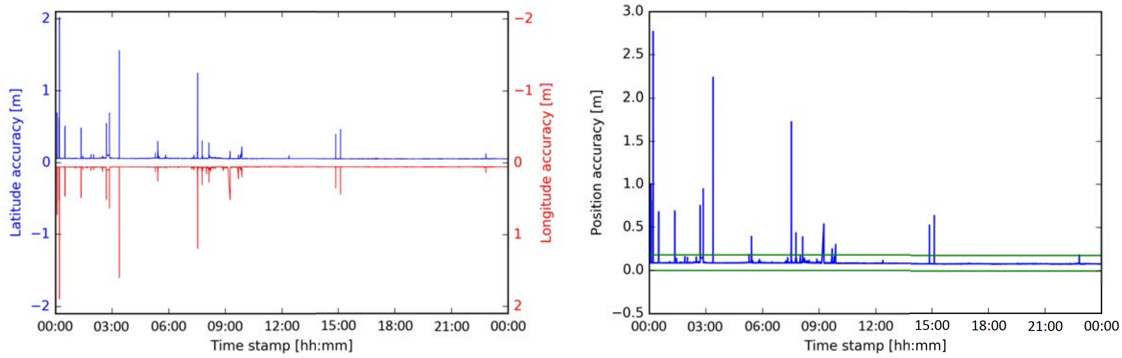

Figure 5.5: Position accuracy for DGNSS positioning using three SAPOS base stations. Accuracy for latitude and longitude position [m] over a period of 24 hours (left) and horizontal position accuracy [m] (right). The green horizontal lines indicate the computed confidence interval.

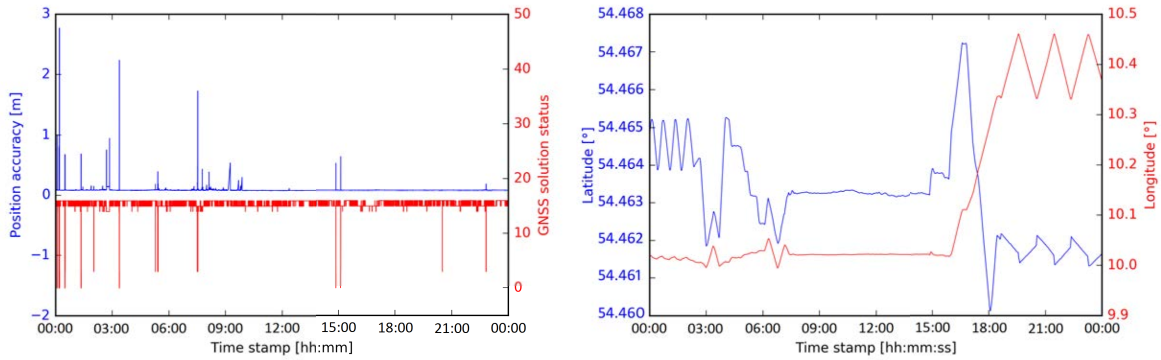

Figure 5.6: GNSS solution status and bearing. Horizontal position accuracy [m] in relation to the GNSS status over a period of 24 hours (left) and the bearing of the vessel shown in latitude and longitude (right).

Figure 5.5 gives exemplary evidence of the comparison of latitude and longitude accuracy computed for the DGNSS solution using all three SAPOS® base stations. The graphs for the other DGNSS solutions can be found in the Appendix B. On the right, same as in Figure 5.3, the horizontal resolution is displayed. The latitude accuracy varies between 0.055 m and 2.023 m, the longitude accuracy shows a variation from 0.054 m to 1.900 m. In comparison to the absolute solution, various outliers can be seen during midnight and 03:00 AM and around 09:00 AM. Taking a look to the logged GNSS status which can be seen on the left side of Figure 5.6, it can be seen that some of them are caused by a loss of the DGNSS solution or even the complete GNSS signal. In comparison to the GNSS solution status 3 indicating the absolute positioning, for one the DGNSS is alternating between 15 and 16 which describes a change from the float to the integer processing results. It is striking that the detected accumulation of less accurate measures in the early afternoon hours does not exist anymore. Hence, a cluster of noticeable deviations can be detected around 09:00 AM which could also be recognized in the horizontal accuracy of the absolute positioning, but there it is not that distinctive as the order of magnitude is different.

In summary, it can be seen that both the accuracy given for the absolute positioning and the accuracy given for the DGNSS positioning are within the stated manufacturer requirements. Regarding the horizontal accuracy, the usage of the SAPOS® correction service leads to an increasing horizontal accuracy as it was expected in forehand. In percentages, this is equivalent to an increase of of approximately 87.5 %. Comparing the achieved accuracies for the DGNSS positioning it is conspicuous that there are only small differences between the different post processing setups. The only exception is constituted by the single usage of the SAPOS® corrections sent by the base station in Westermarkelsdorf. In comparison to the other setups, a deviation of approximately 0.07 m is detectable which may result from the distance between the area of investigation and the base station itself. From the financial perspective, it is of particular interest that there are no significant differences between the other solution using all of the SAPOS® base stations or just one of them. The maximum difference as already stated amounts to 0.07 m which is still negligible for the detection of ammunition bodies as they have a certain size which can be assumed to be not smaller than 0.10 cm as it can be seen within the snippet backscatter evaluation.

5.3 Hydrographic data interpretation

The hydrographic interpretation of the final products resulting from the data processing includes the bathymetric maps and graphic representations created with CARIS HIPS and SIPS 8.1 as well as the different mosaics generated with the QPS Feldermaus Geocoder 7.3.6 software application. The emphasis is laid particularly on the results of the comparison between the detected bodies located on the seafloor and the already mapped ammunition from the Tactical Map. Unfortunately, the data collected with the SBP is only restrictedly suitable. Due to the fact that the time stamp within the data is erroneous, it was not possible to combine the GNSS position data with the depth information. However, as the coordinates for the start- and endpoint of the survey lines are known, the data can still be used to get a general impression of the subsurface structures in the area of investigation.

5.3.1 Bathymetric data interpretation

As it was explained in the previous chapter, the chosen grid size for the bathymetric chart is based on the calculation of the horizontal component of the TPU. Figure 5.7 displays a random excerpt of the horizontal TPU over the complete swath of 400 soundings. While the x-axis describes the sounding number where sounding 200 represents the nadir position, the y-axis points out the percentage of the different contributing influence factors. Obviously, the static GNSS uncertainty component is the most powerful influence. It is important to note that the impact is the greatest at the nadir position and slightly decreases when moving to the outer beams. In concrete figures, the percentage effect varies between 97 % and 100 % which leads to a component value of 0.390 m. The heading uncertainty as well as the real time sonar uncertainty make up the remainder whereas only the heading has a considerable impact of 0.010 m for the outer beams which contributes to the total horizontal TPU of 0.395 m. This distribution was to be expected as both components are related to each other as a change of the course automatically leads to a change in the position. Thereby, the influence exponentially increases with the distance to the center of movement represented by the vessel.

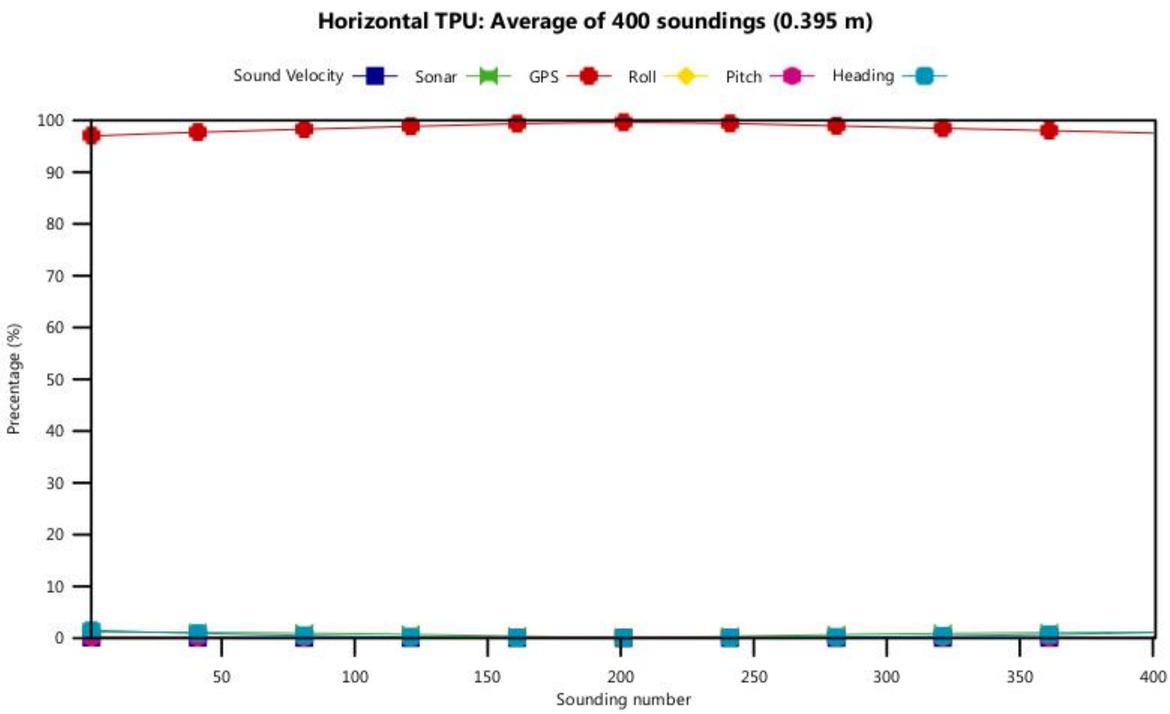

Figure 5.7: Percentage horizontal TPU for a complete swath (400 soundings) based on CARIS HIPS and SIPS 8.1. A graph for the same swath showing the component values can be found in Appendix B.

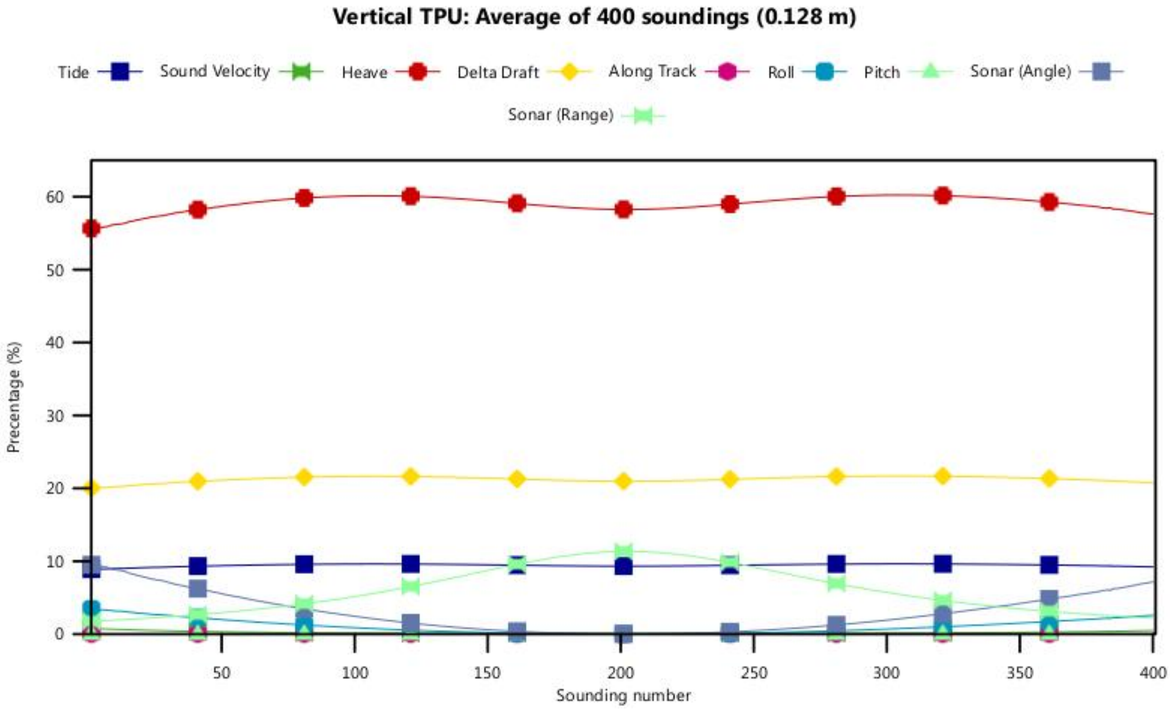

Figure 5.8: Percentage vertical TPU for a complete swath (400 soundings) based on CARIS HIPS and SIPS 8.1. A graph for the same swath showing the component values can be found in Appendix B.

Regarding the vertical TPU depicted in Figure 5.8 as a representative for the depth uncertainty, the influencing factors differ from the ones contributing to the horizontal TPU. The vessel motion in vertical direction represented by the uncertainties of heave and draft is the most influencing factor. It can be seen that the influence both in the nadir direction and in the outer beam region is imperceptible smaller. The uncertainty caused by the tidal influences shows the same distribution, but in a smaller range as the Baltic Sea is not influenced by a strong tidal current as for example the North Sea. The influence of the dynamic components is negligible even if the graphical representation shows a slight increasing impact for the outer beams which is also caused by the increase of the distance between the vessel and the target point on the seafloor. The at first glance most conspicuous uncertainty contribution is the graph which represents the range of the sonar. With increasing beam angle, the effect becomes lower due to the longer distance. Strikingly, the sound velocity seems to have no effect, even if it directly influences the acoustic wave propagation. Taking all the Factors displayed in Figure 5.8 into account, the vertical TPU amounts to 0.128 m in total and is therefore approximately three times less than the horizontal TPU. This stresses once again the importance of a precise GNSS positioning to obtain the best possible solution in accordance with the requirements.

To be able to evaluate the conducted hydrographic survey, the minimum standards stated by the IHO (2008) and accessible in Appendix B are consulted. As the stated uncertainties are also based on a 95 % confidence level, the requirements can directly be compared to the computed values from CARIS HIPS and SIPS 8.1. Comparing the maximum allowable horizontal component of the TPU, the Special Order as the highest quality mark requires 2 m whereas the collected data provide a value of 0.395 m. To be able to compare the vertical components, a simple computation has to be taken out using the following formula given by the IHO (2008):

$$Vertical\ TPU = \pm\sqrt{a^2 + (b \cdot d)^2} \tag{5.1}$$

In this formula, the uncertainty itself is divided into a component which does not vary with the water depth (a) and a component which does vary with the water depth (b · d), whereas b acts as a coefficient for the water depth d. Inserting the values stated for the Special Order and assuming an average water depth of 12.4 m, this leads to a vertical uncertainty of 0.267 m. Thus, the survey fulfills all requirements for a Special Order classification according to the IHO minimum requirements.

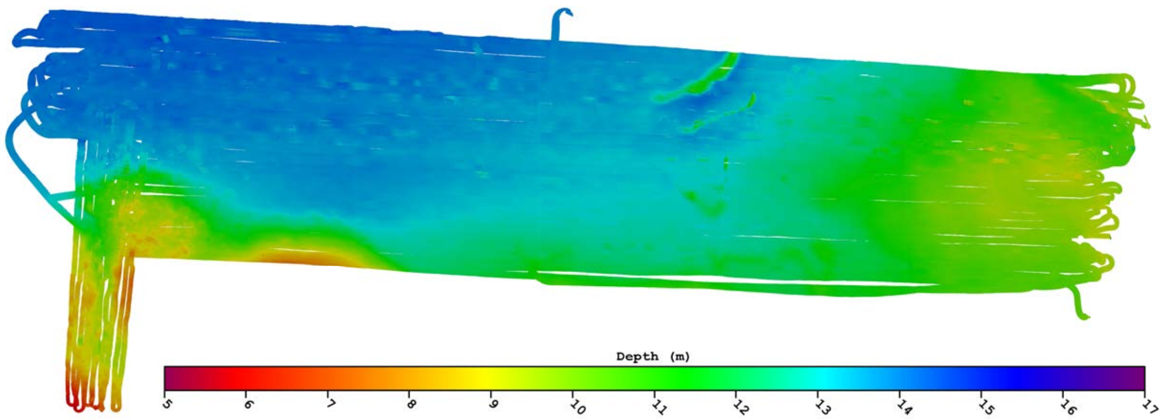

Figure 5.9: Bathymetric data processed with CARIS HIPS and SIPS 8.1. Grid size of 0.40 m x 0.40 m according to the horizontal TPU. The full size image can be found in Appendix A.

The bathymetric grid shown in Figure 5.9 ranges from 5.38 m up to 16.80 m water depth, whereby the southeast represents the shallower area. In the northwestern part of the survey area, the seafloor falls off and it gets deeper. Taking into consideration the localization of the area and its genesis, a confirmation of the storm surge event in 1625 can be construed.

The histogram depicted in Figure 5.10 illustrates the overall distribution of the depth values. In total, 15,223,695 depth values are pictured.

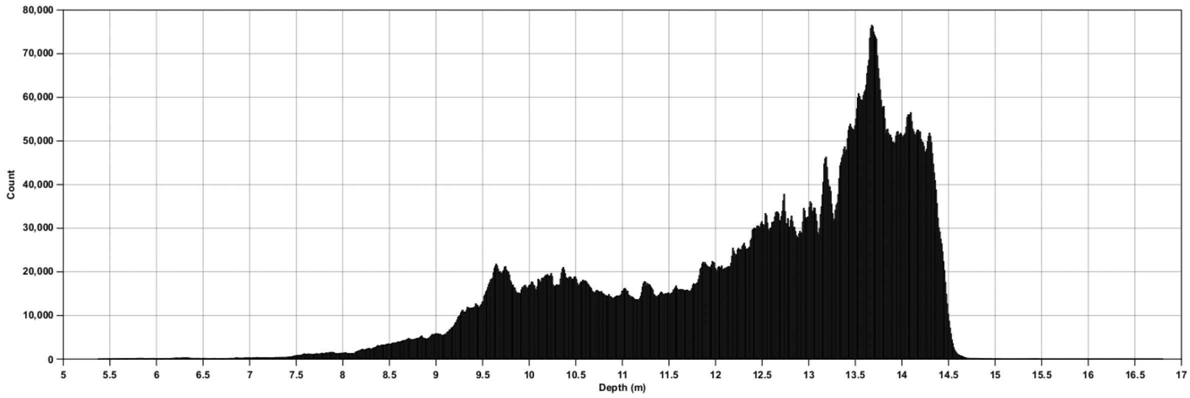

Figure 5.10: Histogram representing the distribution of depth values. The full size image can be found in Appendix A.

Most of the ammunition bodies were detected at depth from around 14 m with few exceptions. In the north of the investigated area, two conspicuous features arise from the seafloor. The more dominant one rises up to 3 m and measures approximately 650 m, the smaller one measures 600 m with a height of 1.5 m. The origin cannot be determined only by this information, but with regard to the nearby areas, it can be assumed that these ridges are permanently located there as there are indications of scouring on the east side of the structures.

5.3.2 Snippet backscatter interpretation

As already indicated in the previous chapter, the grid size for all created mosaics is computed by using the information about the specific beam configuration set within the Fledermaus Geocoder 7.3.6 and the along-track coverage which has to be determined for each beam according to formula 5.3 given by the IHO (2005)[22]:

$$a_{\mathsf{y}} = \frac{2 \cdot z}{cos^2(\beta)} \cdot tan(\tfrac{\Phi_{\mathsf{R}}}{2}) \tag{5.2}$$

$$a_{\mathsf{x}} = \frac{2 \cdot z}{cos(\beta)} \cdot tan(\tfrac{\Phi_{\mathsf{T}}}{2}) \tag{5.3}$$

For the computation of the across-track coverage a_y, information of the mean water depth z, the beam pointing angle β, and the beam width of the receiving beam Φ_R are required. The formula given for the along-track coverage a_x includes the beam width of the transmitting beam Φ_T in addition to the aforementioned parameters. Using the average water depth of 12.4 m taken from the analysis of the bathymetry and the beam width of 0.65° as stated in Kongsberg Maritime AS (2013a), the following footprint dimensions are computed:

Table 5.5: MBES footprint dimensions for nadir position and outer beams.

	Nadir beam ($\beta = 0°$)	Outer beam ($\beta = 65°$)
Across-track coverage	0.28 m	1.58 m
Along-track coverage	0.28 m	0.67 m

The number of pixels for each swath has to be taken into account for the grid size computations as well. Taking a look to the differences between the nadir and the outer beam of the swath, it is clearly accessible that the pixel density decreases with an increasing incidence angle what in turn leads to a worsening of the resolution. Assuming an average number of 3,500 pixels per swath according to evaluations using the CARIS HIPS and SIPS 8.1 dump utility, for a swath consisting of 400 beams this leads to a number of approximately nine pixels per beam. Obviously, the information in the nadir region is much denser than in the outer beams. Taking this into account, the grid size for the evaluation of the suspected cases was set to 0.05 m x 0.05 m whereas the overview mosaic generated from the snippet backscatter information displayed in Figure 5.11 uses a grid size of 0.50 m x 0.50 m. Due to the general settings of the color table, high snippet backscatter intensities are represented by light colors and accordingly a low snippet backscatter intensity is indicated by a dark coloring.

[22]The depicted formulas are valid for the dimensions of the footprint ellipse on a flat seafloor. The corresponding adaptions in case of the presence of a slope can be seen in IHO (2005).

Figure 5.11: Snippet backscatter image of the survey area processed with Fledermaus Geocoder 7.3.6. Dark colors represent low, light colors high backscatter intensities. Values given in dB. Mosaic pixel size: 0.50 m x 0.50 m. The full size image can be found in Appendix A.

Obviously, the overview is consistent with the bathymetric grid shown in Figure 5.9 and also with the ARA sediment analysis described in more detail in the following section. The conspicuous features in the north of the investigated areas are clearly detectable within the snippet backscatter mosaic. This leads to the conclusion that they are of different sedimentary composition and surface texture in comparison to the surrounding area. With regard to the high intensity values, it can be assumed that they consist of more solid sediment or rock with rough contours which would support the previous assumption. In addition, some structures in the south of the already mentioned features show off. In the bathymetric model, they are almost unremarkable, but the evaluation of the snippet backscatter shows differences according to the environment. In the more contaminated western part of the survey area it can be seen that the surface is split in an area evoking high backscatter intensities and an area with low backscatter intensities. As stated above, this can be an indication for a varying seafloor surface morphology and composition.

Besides the information concerning the morphology, additional details can be seen especially in the more contaminated western part of the investigated area where the water depth increases in comparison to the shallow parts in the east and south. Figure 5.12 shows an extract mosaic which gives indication of significant tracks highlighted with the dotted lines. Due to the parallelism and the occurrence in trio formation, some of these tracks can be identified as marks caused by trawl fishery. This appraisal is corroborated by the the fact that according to Böttcher et al. (2011, 2015) and Frenz (2014) ammunition bodies were found on and on as a dangerous by-catch. For further analyses, such marks may also give evidence of dumping pattern as it is historically documented that some of the warfare material was dumped even before the actual designated dumping site was reached (Böttcher et al., 2015). Furthermore, a possible spreading of dumped ammunition bodies as a result of external influences like the already mentioned fishing operations can be reproduced using these additional information.

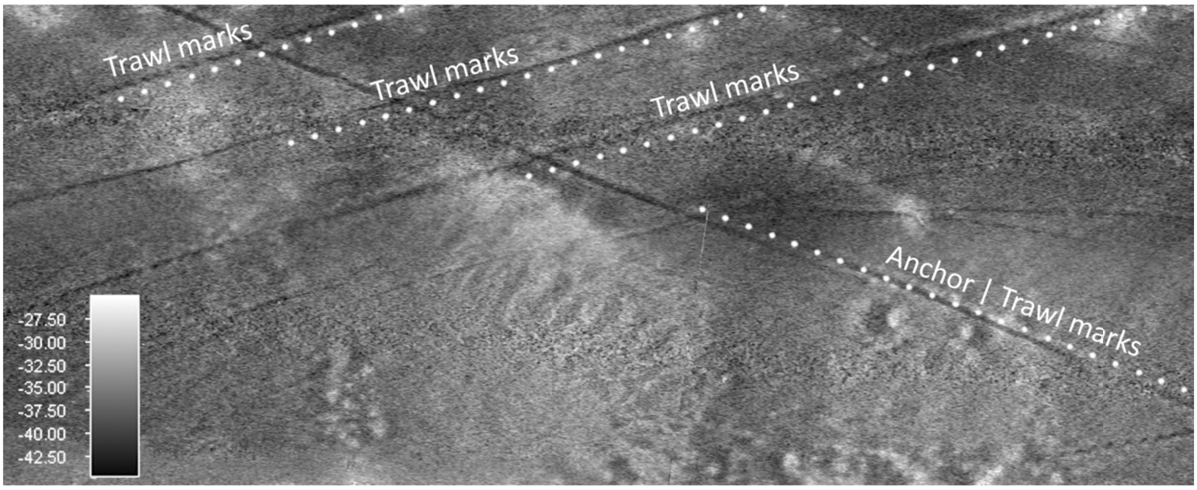

Figure 5.12: Tracks on the seafloor detected within Fledermaus Geocoder 7.3.6. Dark colors represent low, light colors high backscatter intensities. Values given in dB. Mosaic pixel size: 0.05 m x 0.05 m.

Likewise, some circular features are detectable as shown in Figure 5.13. With a diameter of approximately 15 m and their spatial proximity to the ammunition site, this may be the location of a controlled detonation. However, a verification for this assumption cannot be given with regard to the present state of research. A comparison with the information of the Tactical Map is not possible as the features are outside of the coverage area. A consultation with a member of the body of experts from MELUR revealed that, based on the shape of the circular features, the assumption can be considered plausible regarding to the detonation method. Due to the strengthened sound propagation and the arising pressure waves caused by an underwater detonation, these procedures are only performed in cases where this is unavoidable for safety reasons. The circular form which can be seen in Figure 5.13 arises from an installed bubble curtain which completely surrounds the detonation spot to reduce the acoustic wave propagation and therefore to protect fishes and marine mammals. Using this technique, a reduction of the vulnerable water areas of up to 97 % can be achieved, but it is also complex and cost-intensive (Böttcher et al., 2011, 2015).

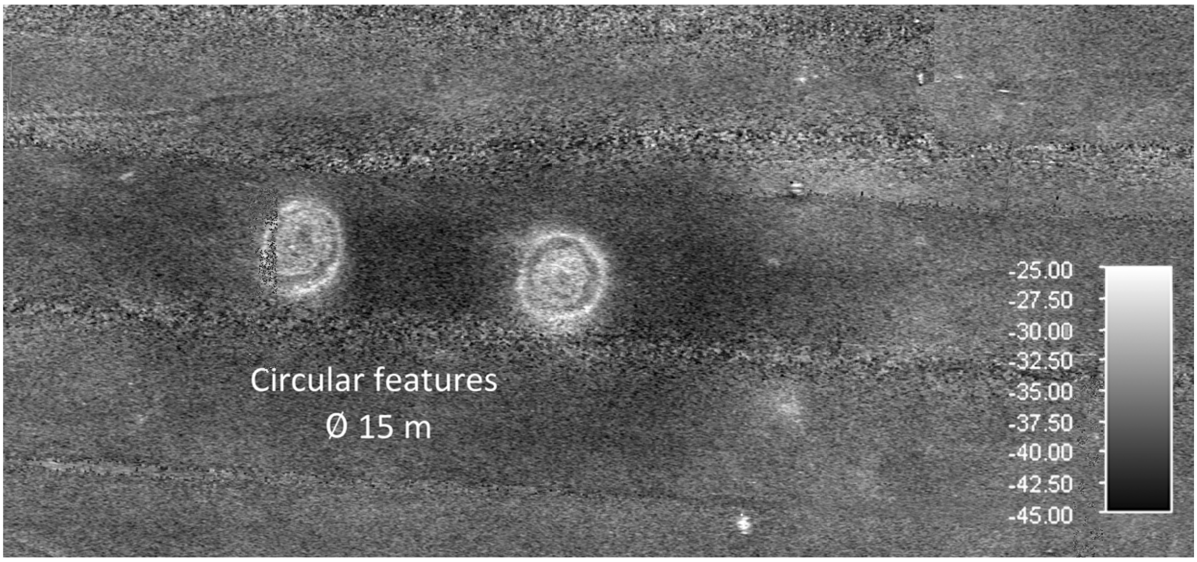

Figure 5.13: Circular features on the seafloor detected within Fledermaus Geocoder 7.3.6. Diameter of approximately 15 m, distance between both features approximately 30 m. Dark colors represent low, light colors high backscatter intensities. Values given in dB. Mosaic pixel size: 0.05 m x 0.05 m.

To be able to evaluate the feasability of snippet backscatter information for the detection of suspicious objects and ammunition on the seafloor, 20 exemplary objects are examined and compared with the official information stored in the Tactical Map. The examined featured are detected and captured during the data acquisition within the Kongsberg SIS software. During the post-processing using the Fledermaus Geocoder 7.3.6 application, these sections were evaluated with particular attention to be able to compare the picked locations of the suspicious objects to the Tactical Map information after transforming the Cartesian into geographic coordinates. The mentioned exemplary objects include individual objects of different size and location in the MBES swath, stray fields or other small objects arranged in a cluster. The following figures show all examined objects: The left image subscripted as *.A always shows the screenshot taken during the data acquisition. In comparison to the following two images, this one is not geographically referenced and therefore the objects are rotated with respect to the appropriate bearing of the vessel. In the middle indicated as *.B, the processed and geographically referenced snippet backscatter mosaic created with Fledermaus Geocoder 7.3.6 with a pixel size of 0.05 m x 0.05 m is shown. A comparative sonar image taken from the Tactical Map is displayed on the right side named as *.C. Table 5.6 summarizes all information of the objects including the water depth, type, dimensions, detected deviations in the horizontal position, and the approximate position of the object within the MBES swath. At this point it should be emphasized once again that all information which may lead to the location of warfare objects are consciously waived for safety reasons.

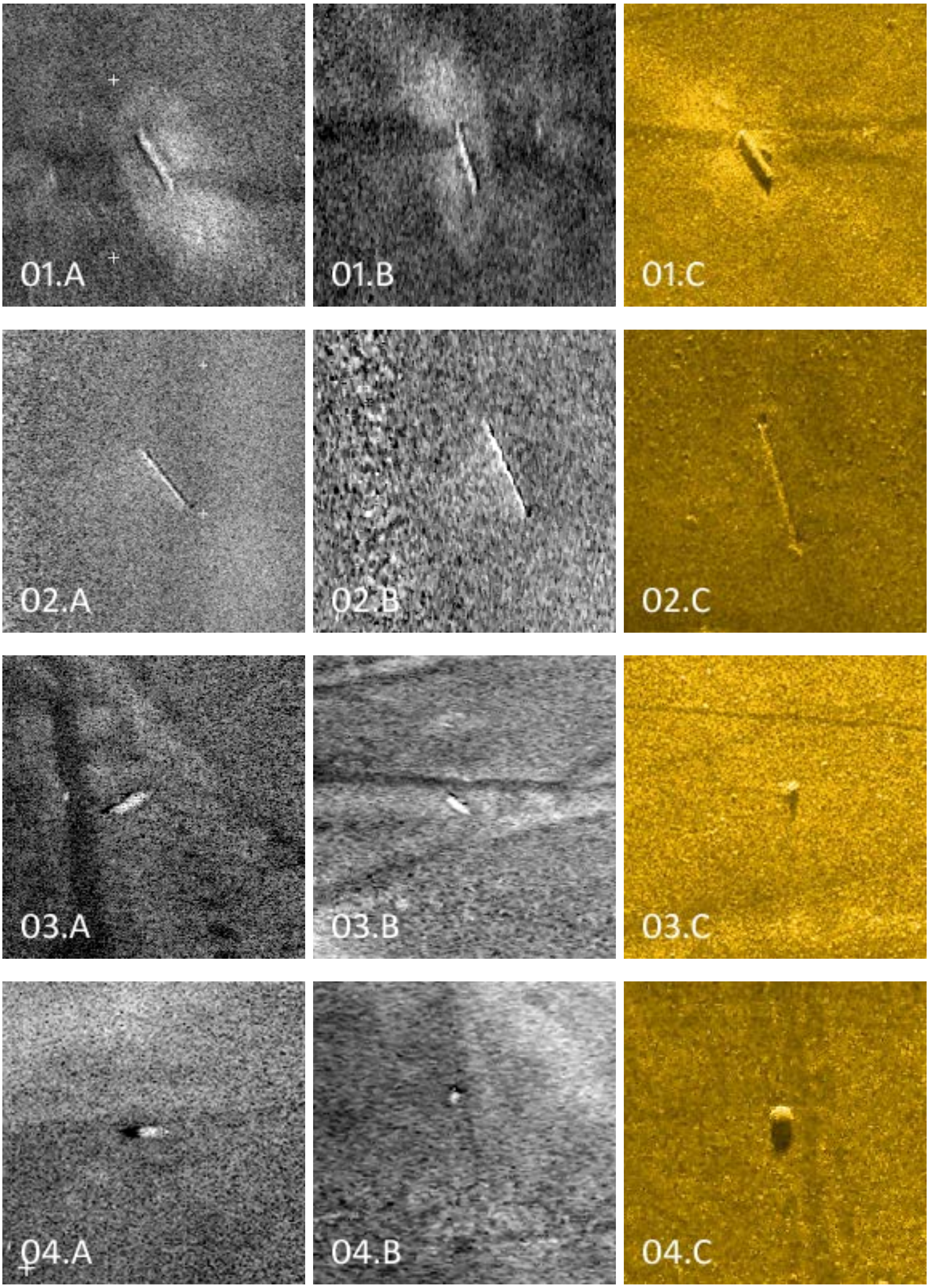

Figure 5.14: Evaluation of suspicious objects and ammunition bodies. Detailed information to the displayed objects is given in Table 5.6.

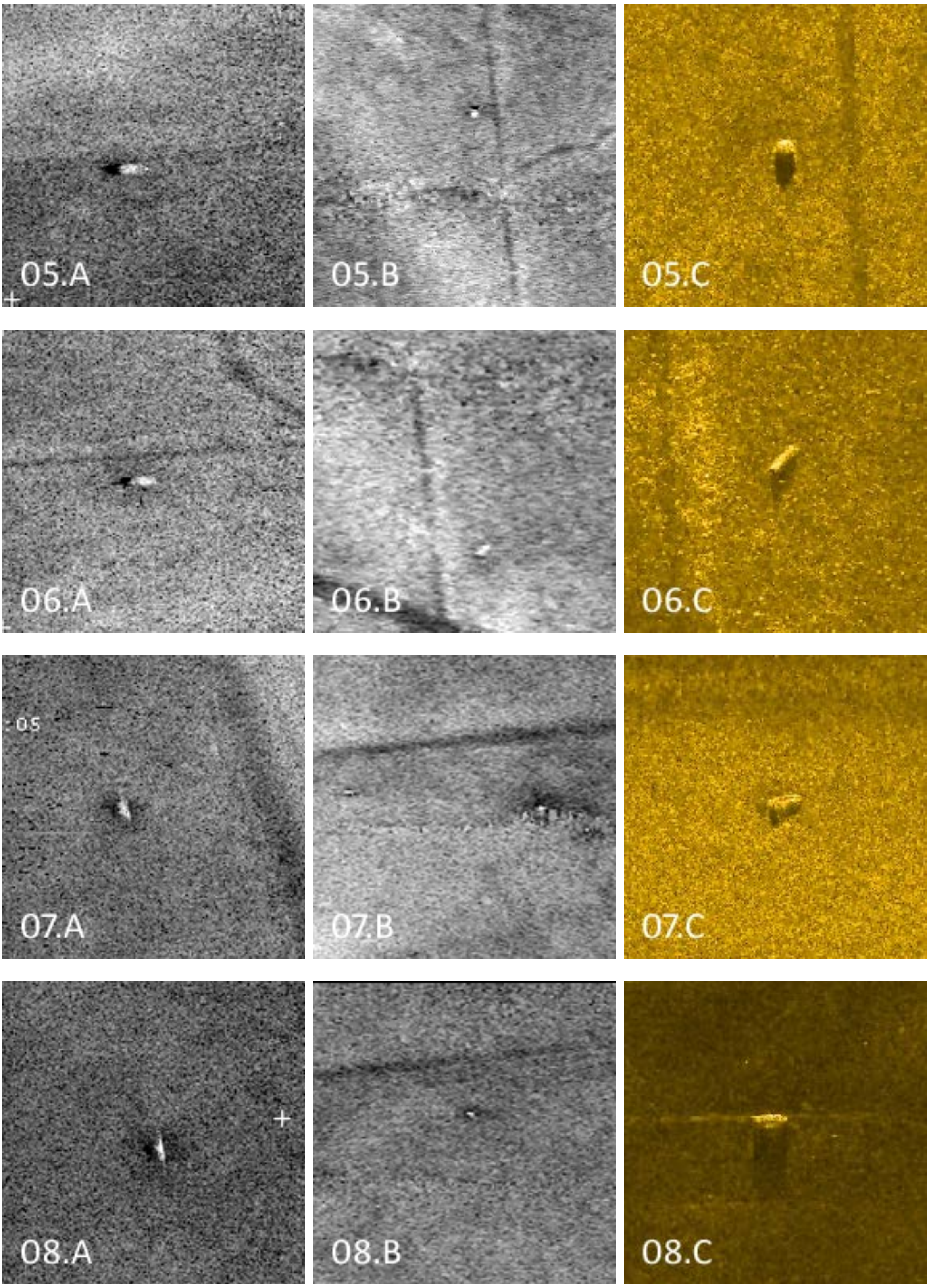

Figure 5.15: Evaluation of suspicious objects and ammunition bodies. Detailed information to the displayed objects is given in Table 5.6.

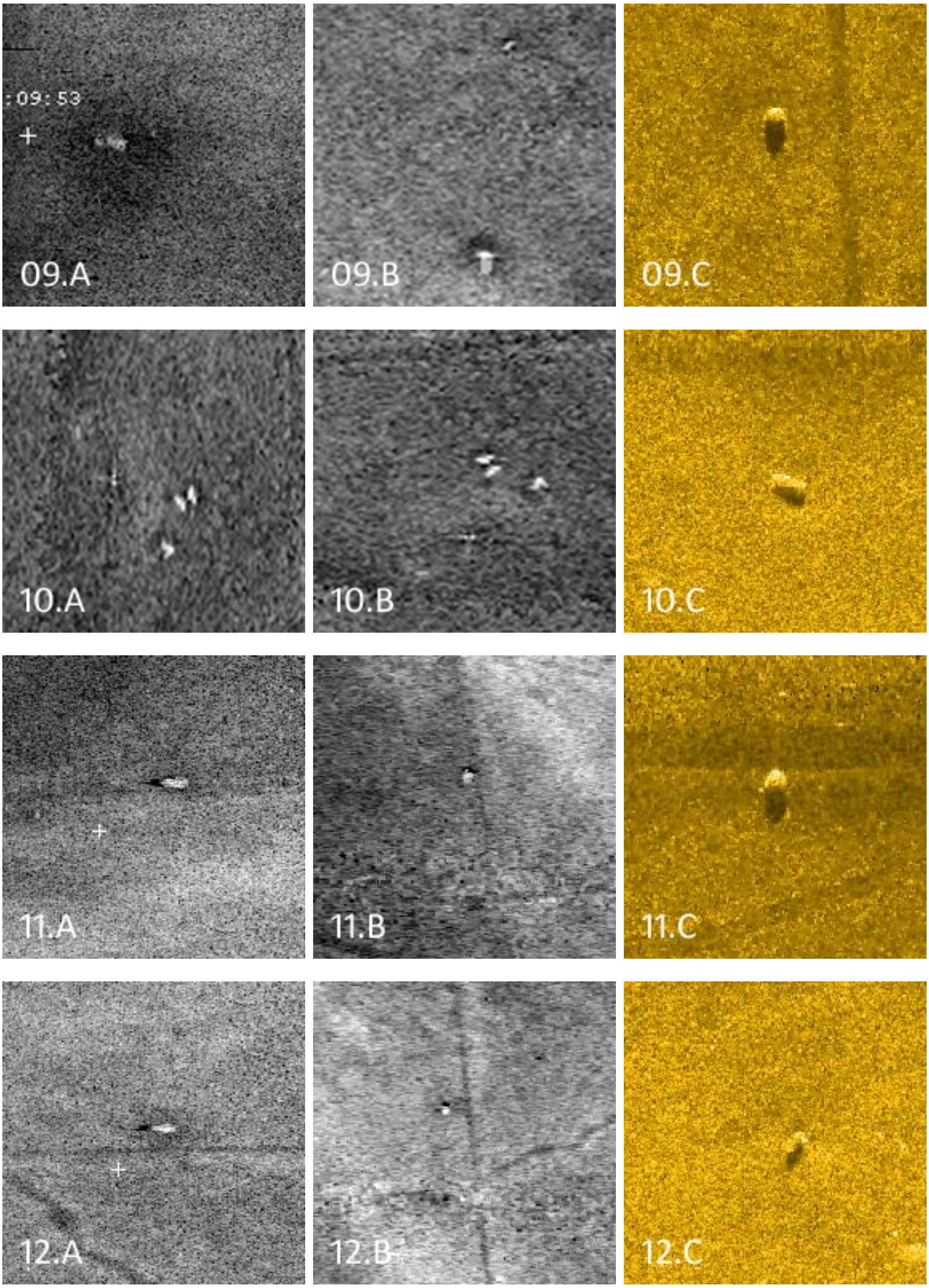

Figure 5.16: Evaluation of suspicious objects and ammunition bodies. Detailed information to the displayed objects is given in Table 5.6.

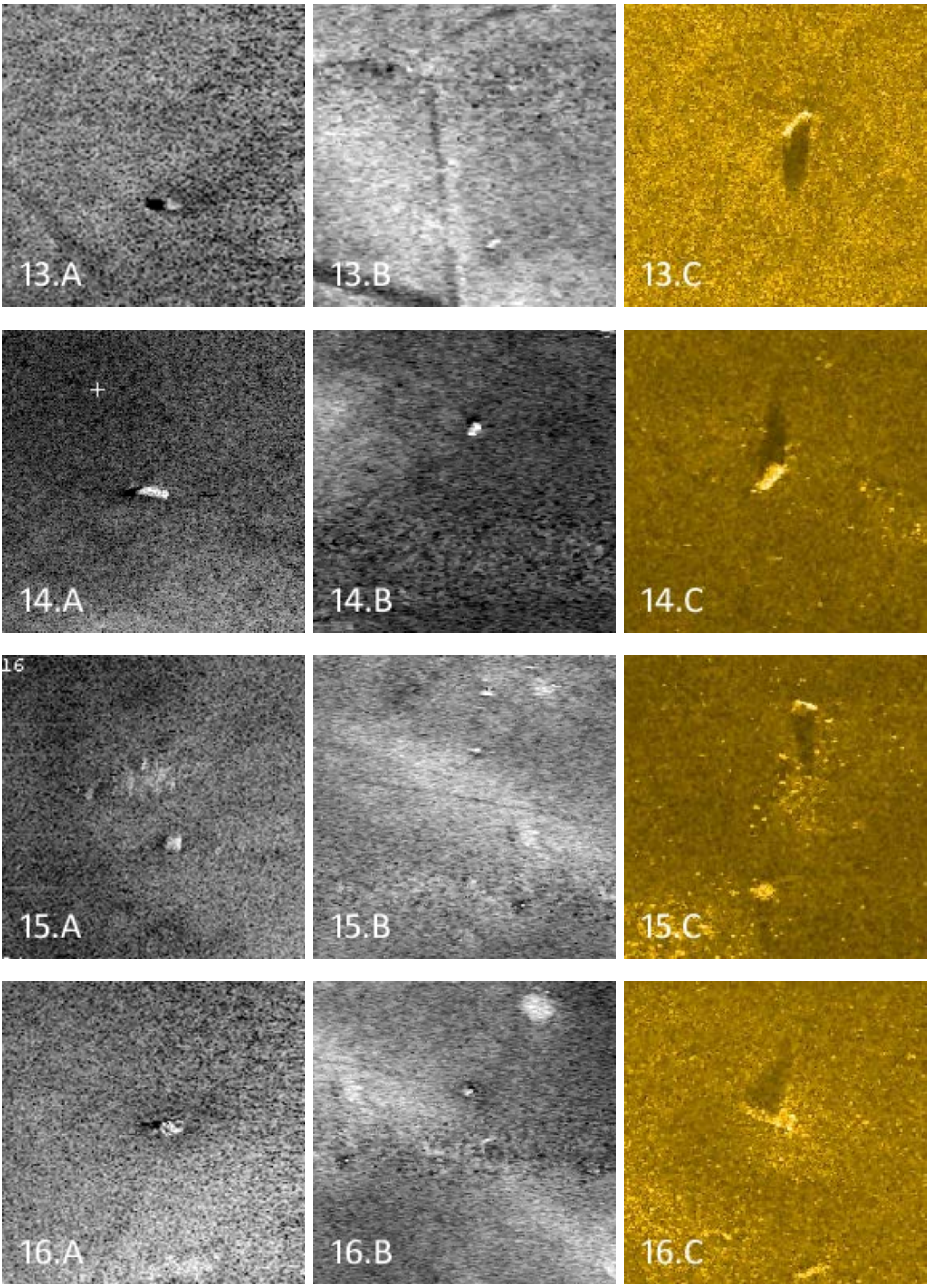

Figure 5.17: Evaluation of suspicious objects and ammunition bodies. Detailed information to the displayed objects is given in Table 5.6.

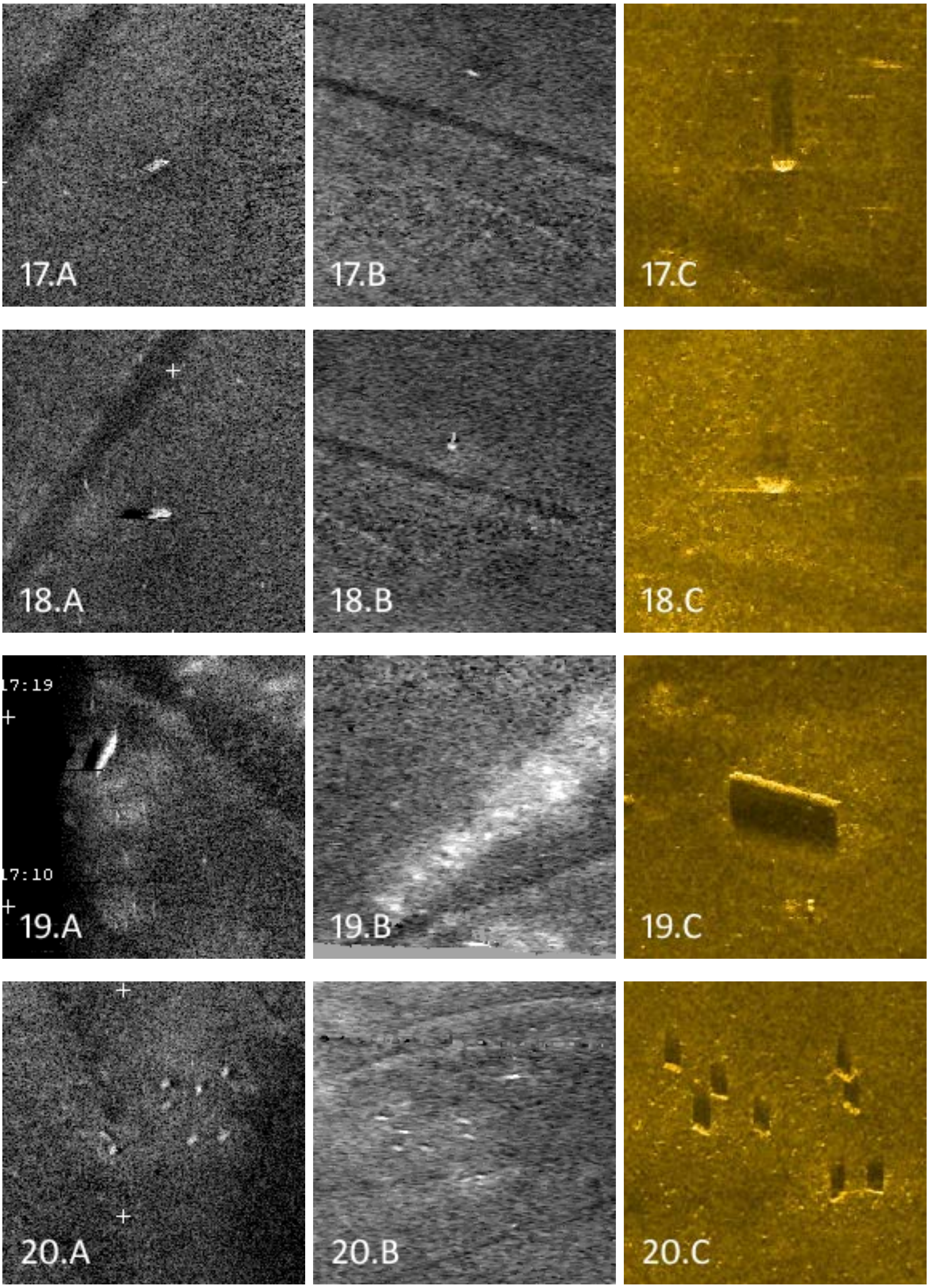

Figure 5.18: Evaluation of suspicious objects and ammunition bodies. Detailed information to the displayed objects is given in Table 5.6.

Table 5.6: Information of suspicious objects and ammunition bodies. Water depth [m], object type according to the Tactical Map, dimensions (values indicated by an asterisk are measured within the Fledermaus Geocoder software), difference between the estimated horizontal positions (Tactical Map - Evaluation), position shift according to the official value stated in the Tactical Map, approximate position of the object within the MBES swath, and acquisition date of the Tactical Map information.

ID	Depth [m]	Object type	Dimension [m]	Difference [m]	Longitudinal shift [m]	Transversal shift [m]	Swath position	Acquisition
01	19.1	Poss ground mine	2.7 x 0.5 x 0.2	9.05	-1.29	-8.96	middle	08.02.2012
02	13.4	Mine like	6.7 x 0.3 x 0.2	7.92	-4.95	6.18	middle	02.05.2012
03	19.2	Poss moored mine	1.9*	5.15	4.89	-1.6	middle	08.02.2012
04	19.3	Poss moored mine	1.3*	1.04	-0.63	-0.83	middle	08.02.2012
05	19.4	Poss moored mine	1.3*	1.36	-1.12	-0.78	middle	08.02.2012
06	19.4	Drum	1.2*	2.9	-2.37	-1.67	middle	08.02.2012
07	18.9	Drum	1.5*	6.73	6.68	0.85	middle outer	08.02.2012
08	18.8	Poss moored mine	1.5*	12.66	10.34	-7.3	middle outer	08.02.2012
09	19.0	Rock	1.9*	3.15	-2.1	2.35	middle outer	08.02.2012
10	19.1	Drum	1.9*	5.29	1.51	-5.07	middle outer	08.02.2012
11	19.4	Poss moored mine	1.2*	0.94	-0.91	0.25	middle	08.02.2012
12	19.4	Drum	1.3*	0.75	-0.7	-0.27	middle	08.02.2012
13	19.4	Drum	1.2*	1.48	-1.47	-0.19	middle	08.02.2012
14	18.8	Drum	1.5 x 0.8 x 0.4	2.58	-1.02	2.37	middle	02.05.2012
15	19.1	Rock field	4.5*	4.43	-3.42	2.81	middle outer	08.02.2012
16	17.8	Mine like	1.6*	4.67	-2.68	3.83	middle inner	02.05.2012
17	19.6	Poss moored mine	1.2*	19.4	-18.21	-6.7	middle	09.02.2012
18	19.8	Poss moored mine	1.3*	8.18	-2.07	7.91	middle	09.02.2012
19	19.2	Pipe torpedo	4.2*	6.65	-0.64	-6.62	outer	08.02.2012
20	19.1	Drums	12.1*	23.99	7.2	-22.88	middle outer	08.02.2012

Comparing the images taken during the data acquisition and the created snippet backscatter mosaic, the post-processed images remain significantly below the expectations. After a consultation with the manufacturer of the Fledermaus Geocoder software, the reason for this issue seems to be identifies as the fact that for the data processing an older version was used which did not ideally support the utilized MBES with all its properties[23]. Nevertheless, a determination of ammunition bodies is technically feasible as shown using the prefixed examples. All objects are located basically in the same water depth as the area appears in a flat and uniform shape. Therefore, only a theoretical assessment of the sensitivity is possible. Based on the fact that an increasing water depth leads to increasing beam footprints and thus less snippet backscatter information, a detection at a certain water depth will no longer be possible.

The object type usually is accompanied by the dimensions of the object. Within this case study, the object size differs from 6.7 m to approximately 1.0 m. Taking a look to the presented images, at least in the Kongsberg SIS data all objects are clearly identifiable and almost explicit distinguishable from natural objects as rocks. Regarding the post-processed snippet backscatter mosaic, the allocation is not always possible. A reason for this might be the comparatively bad resolution as actual, the post-processed data is at least comparable to the online data displayed during the acquisition. Thus, the post-processed images did not represent the normal case and the assessment regarding the detectable object sizes must be treated with caution. A justification for the ubiquitous differences between the horizontal position of the objects stated in the Tactical Map and the determined position during the post-processing can be seen in the usage of different positioning systems and therefore different accuracy ranges. While the hull-mounted MBES system utilizes the logged GNSS position of the vessel, the sonar which was used for the gathering of the images stored in the Tactical Map is located on an AUV or towed behind a vessel. In both cases, an underwater positioning system is required which is not able to provide a comparable horizontal positioning accuracy. Assuming that the position stated in the Tactical Map is correct, the shifting directions in their individual components of northwards and eastwards can be evaluated to determine a possible constant offset. This consideration takes also the acquisition date of the sonar image stored within the Tactical Map into account as such an analysis makes only sense for the inspection of one survey campaign. A look at the individual components indicates that no constant shifting towards one or another direction can be detected. If such a constant shifting would have been noticed, a systematic error in the positioning could be assumed and further investigated. It is conspicuous that for the examined stray field the

[23] In this thesis, the post-processing was done using the software version 7.3.6. According to themanufacturer, version 7.5.3 should be used to access the recent sonar model.

straight distance was determined to be that large even if it is clearly identified. This kind of deviation most probably results from the fact that it is not known where position stated in the Tactical Map was picked. Depending on the philosophy, this could be for example the assumed center of the object or, to refer to the safety of navigation, it is possible to pick the position where the object has its highest elevation and therefore provides the shallowest navigable water depth. However, this kind of consideration is only of relevance for stray fields or objects arranged in a cluster. For individual objects this is rather negligible due to their small dimensions. The detected differences in the horizontal position are represented by the distance between the official Tactical Map position which is assumed to be correct and the calculated horizontal position based on the snippet backscatter post-processing with Fledermaus Geocoder 7.3.6. For the evaluated object, this distance ranges from 1 m to 10 m, whereby there are three object where the distance exceeds this range. Regarding the beam angle, same as for the water depth, only a theoretical assessment of the sensitivity is possible due to the fact that none of the evaluated objects are located in the nadir beam or in the outer beam area. As already indicated in the beginning, the outer beams of the MBES swath have a stretched footprint which leads to a decreased resolution. In the nadir position, the footprint of the beams are smaller, but due to the incidence angle, mainly reflection occur and recorded objects are not visible or at least not clearly identifiable as also artifacts can be a result of the reflection.

5.3.3 Sediment interpretation

As already identifiable in Figure 5.9, there are structures situated in the north of the investigated area. Only by using the information given in the bathymetry it is not possible to make a specific statement of the situation. With the aid of the backscatter mosaic displayed in Figure 5.11, it was possible to derive further conclusions as the structures were clearly identifiable. They show a high backscatter intensity which acts as an indicator for solid material. When regarding the gathered SBP data collected in profile SBP_04 and depicted in Figure 5.19, it is obvious that the structures are not composed by sediments. Whereas the area around shows up to five distinguishable sediment layers of different thickness, the bottom of the structures is completely free from any sediments. It can therefore be deducted that the rises are of geological origin.

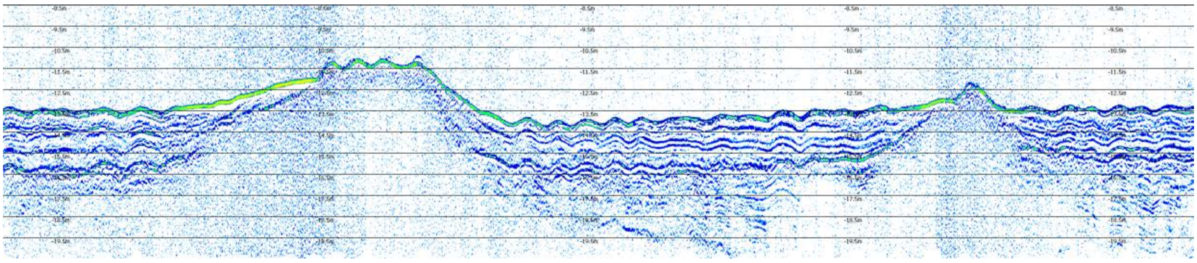

Figure 5.19: Recording of unknown structures in the northern survey area using the SES-2000 standard.

This assumption is confirmed by the ARA mosaic shown in Figure 5.20. As basis for this mosaic, a backscatter image with a grid size of 1.00 m x 1.00 m was used, the categorization is based on the known Wenthworth classification stated in Table 5.7 taken from Ehlers et al. (2016). The ARA mosaic shows the boundaries of different sedimentary areas divided into gravel, sand, silt, and clay depending on their grain size given in phi values. In the northwest of the investigated area, the seafloor is dominated by a clayey surface. This changes slowly into silty ground when moving to the west. In southern direction, it changes rather abruptly into more sandy sediments. Gravel occurs only in small quantities, the largest stolon is located in the southwest. In the north, the mentioned structures are clearly identifiable as they are apparently covered by coarse sand as also partly some gravel is indicated.

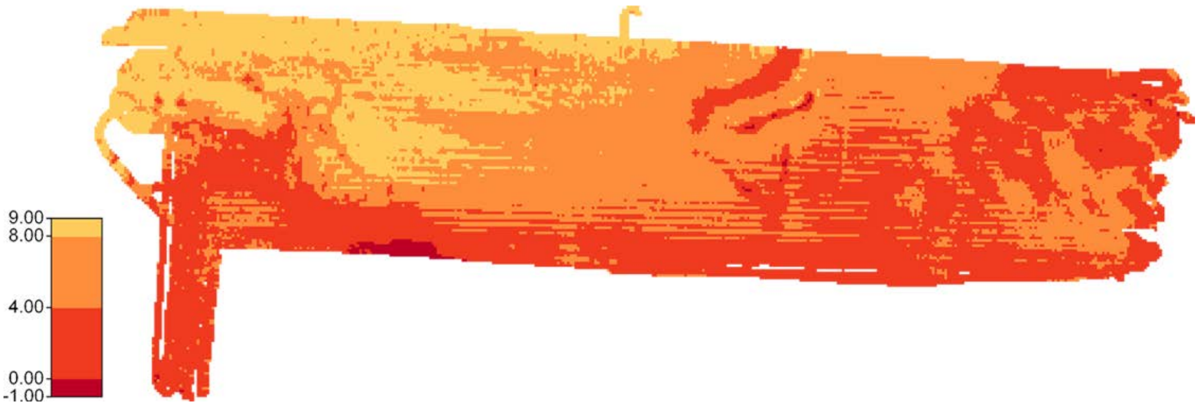

Figure 5.20: Sediment variability based on ARA executed in QPS Fledermaus Geocoder 7.3.6. Values depict the mean grain size in phi units.Yellow area: clay, light orange area: silt, dark orange area: sand, red area: gravel. Underlaying grid size: 1.00 m x 1.00 m.

[23]The mean grain size in Phi units is defined as $M\phi = -\log_2(\alpha)$, where α is the average grain diameter in mm (Lurton, 2010).

Table 5.7: Wentworth classification of the grain size. This scale modifies an earlier version by Johann Udden, and the Phi scale (logarithmic) scale was developed later by William Krumbein (Ehlers et al., 2016).

Wentworth grade	Grain size $[\phi]$	Grain size [mm]
Boulder	-8	>256
Cobble	-6	>64
Pebble	-2	>4
Granule	-1	>2
Very coarse sand	0	>1
Coarse sand	1	$>\frac{1}{2}$
Medium sand	2	$>\frac{1}{4}$
Fine sand	3	$>\frac{1}{8}$
Very fine sand	4	$>\frac{1}{16}$
Coarse silt	5	$>\frac{1}{32}$
Medium silt	6	$>\frac{1}{64}$
Fine silt	7	$>\frac{1}{128}$
Very fine silt	8	$>\frac{1}{256}$
Clay	>8	$<\frac{1}{256}$

To evaluate the classification of the ARA mosaic, randomly selected patches of each sediment type were taken after the processing. One of these exemplary sample is shown in Figure 5.21, further graphical representations can be found in Appendix B. The blue curve indicates the computed default characterization whereas the red and green lines represent the measured response curve of the swath on portside (red) and starboard (green). The better the modeled curve and the actual response fit together, the more reliable the classification result can be considered. With regard to the shown curves and by taking into consideration that no beam pattern correction could be applied, the curves fit very well except for the outer beams where the actual response is way lower than expected. However, this can be attributed to the angular difference between the model which represents 180° coverage while the survey was conducted with only 130° coverage.

The position of the sediment sample taken for ground truthing is located in the southeast and can therefore not be used for the confirmation of the conducted ARA analysis. Assuming a constant sediment spreading, it can be expected that the grab sample contains sandy soil. This assumption was confirmed as sample was composed of coarse sand with interspersed shell detritus. Besides this, some intact blunt gaper shells were detected.

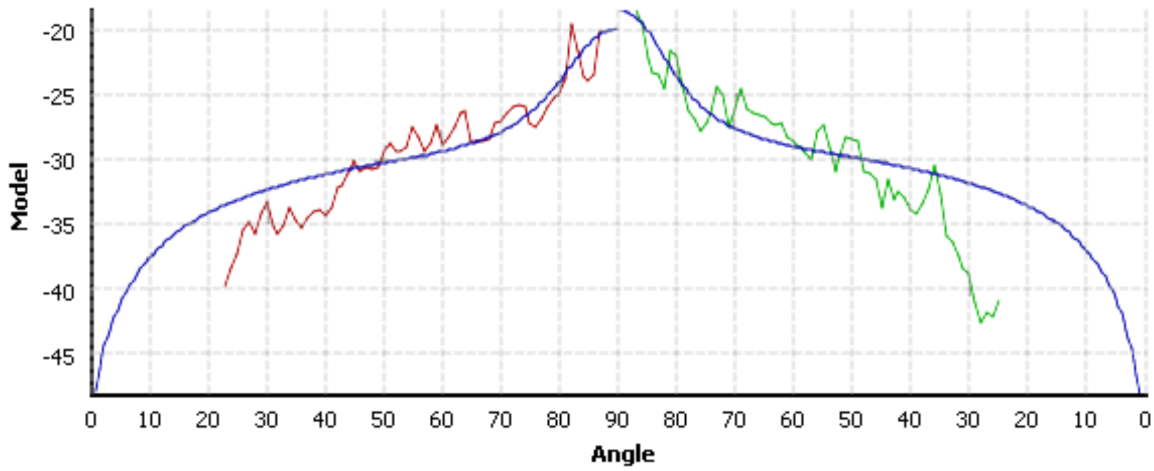

Figure 5.21: Beam pattern for sandy silt sediment generated with QPS Fledermaus Geocoder 7.3.6. Blue curve: modeled response, red/green curve: measured response.

As mentioned in the beginning, the seafloor of the survey area shows a layered structure in the upper part ranging to a maximum of 3 m below the top layer as shown in Figure 5.22. This layered structure exemplary reflects the formation process during the easing glacial period as described at the beginning of this thesis. The wavy structure of the seafloor significantly indicates the heave influence as there was obviously no heave compensation during the data acquisition. In case small ripples or features should be detected, this may lead to a serious problem, but in this case it can be tolerated.

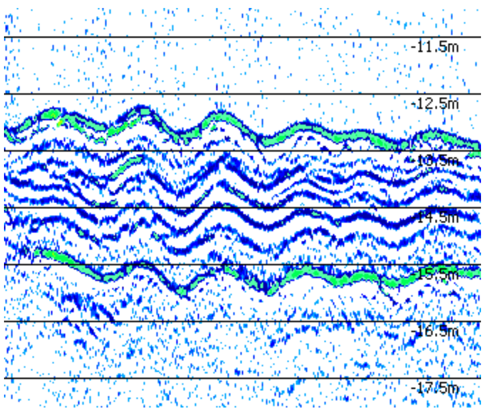

Figure 5.22: Extract of a sediment profile gathered with the SES-2000 standard.

5.4 Comparative analysis of alternative measuring methods

Traditionally, equipped vessels are used for mine hunting. With regard to the technical progress, also equipped AUS become a promising alternative for the detection and classification of suspicious objects on the seafloor using high resolution imagery data. Regarding the fact that most of the ammunition bodies were dumped 60 years ago, a burial of the objects took place due to sedimentation or other environmental impacts. Therefore, not only systems for surface detection are required but also instruments like magnetometer or low frequency SAS to detect ammunition covered by sediment (Kretschmer and Jans, 2016). Within this section, the mentioned systems should be introduced to point out their assets and drawbacks.

Interferometric SAS systems as a special form of SSS were originally developed to fulfill military requirements regarding the detection and classification of small objects located on the seafloor. Typical operating frequencies range between 100 kHz and 300 kHz. The resolution of the resulting image depends mainly on the quality of the position estimation for the sonar antenna in along-track direction (Kretschmer and Jans, 2016). In comparison to common mostly towed sonar systems, an SAS generates images with a resolution which is ten times higher due to the independent and improved along-track resolution (Frenz, 2014). A restrictive factor for the signal processing can be seen in the environmental conditions which can cause external changes of motion or the occurrence of multipath effects especially in shallow waters. Changes in the sound velocity affect the image quality and can cause artifacts. In addition, the signal-noise-ratio directly relating to the seafloor roughness can be stated as an influencing factor for the image quality (Kretschmer and Jans, 2016). The shadowing typically occurrs for SSS respectively SAS data is very important for the determination and examination of ammunition bodies. In comparison to an MBES, a sonar system produces a strong shadowing due to its shallow operation altitude which is necessary with regard to the high working frequency and the required small incident angles (Kongsberg Maritime AS, 2010). A drawback of the shadowing can be seen in the possibly occurring masking of small objects by a shadow. Notwithstanding the operation method, both a towed system and a sonar mounted on an AUV requires an accurate and reliable underwater baseline positioning system. Depending on the range, the positioning can be seen as one of the most restrictive cost factors.

The WTD71 uses the AUV HUGIN 1000MR in combination with the introduced HISAS 1030 sonar both for military and scientific purposes as stated in Frenz (2014) and Kretschmer and Jans (2016). Major emphasis is thereby put on the detection and localization of mines and mine-like objects in the seafloor. Operating within a frequency range of 120 kHz to 60 kHz, HISAS 1030 offers a resolution of 0.03 m x 0.03 m regardless of the range. A swath width of more than 200 m to each side of the sonar can be achieved which is particularly in view of the time management and the involved costs of special interest. In comparison to the MBES system which is able to generate snippet backscatter images beside the bathymetric measures, the HISAS 1030 has the possibility to use its imagery data to generate bathymetric estimates with a spatial resolution of up to 0.05 m x 0.05 m (Kongsberg Maritime AS, 2010). To be able to achieve the stated accuracy and resolution, the AUV has to be equipped with a complex and therefore cost-intensive navigation system. In terms of the cost-benefit-relation, this leads to high acquisition and maintenance costs. Otherwise, the usage of an AUV is advantageous as the vessel can be used for other tasks during the AUV operation. One important aspect at least for military operations is the possibility to utilize the AUV almost unseen. In addition and in contrast to an MBES, the sensor can be adapted to the respective conditions to increase the data quality. As an AUV is operating directly in the water column, it is affected by currents. Especially an occurring transverse flow can have a strong impact on the performance of the mounted sonar as a test conducted by the WTD71 in the North Sea has proven. Besides strong currents, also a shallow area of operation can affect the survey results due to multipath effects and inhomogeneities in the water column. However, in order to use the mounted SAS also in an environment like the investigated area of Kolberger Heide for a comprehensive survey, a constant determination of the sonar conditions containing roughness and texture of the seafloor and the water column characteristics is required. Since 2013, the HUGIN 1000MR of the WTD71 is equipped with a real time system to automatize these steps and to perform real time processing including the detection, classification, and identification of mine-like objects which leads to a more time efficient workflow. To provide an insight into the resulting images of the HISAS 1030 sonar, Figure 5.23 shows a field of poss-moored mines within the investigation area Kolberger Heide (Frenz, 2014).

As low frequency MBES or SAS for the detection buried ammunition bodies are still an object of research, only some theoretical facts according to Jans et al. (2012) and Kretschmer and Jans (2016) are given. In comparison to high frequency systems, they offer only a low angular resolution what implies an unsatisfactory object detection. Due to this low resolution, a lot of wrong detections occur which in turn leads to a complex and time consuming post-processing strategy. Parametric echosounding systems are only conditionally suitable as an alternative method as the efficiency of the generated secondary signal is very low. In addition, they need to be modified to provide three-dimensional data for the object detection.

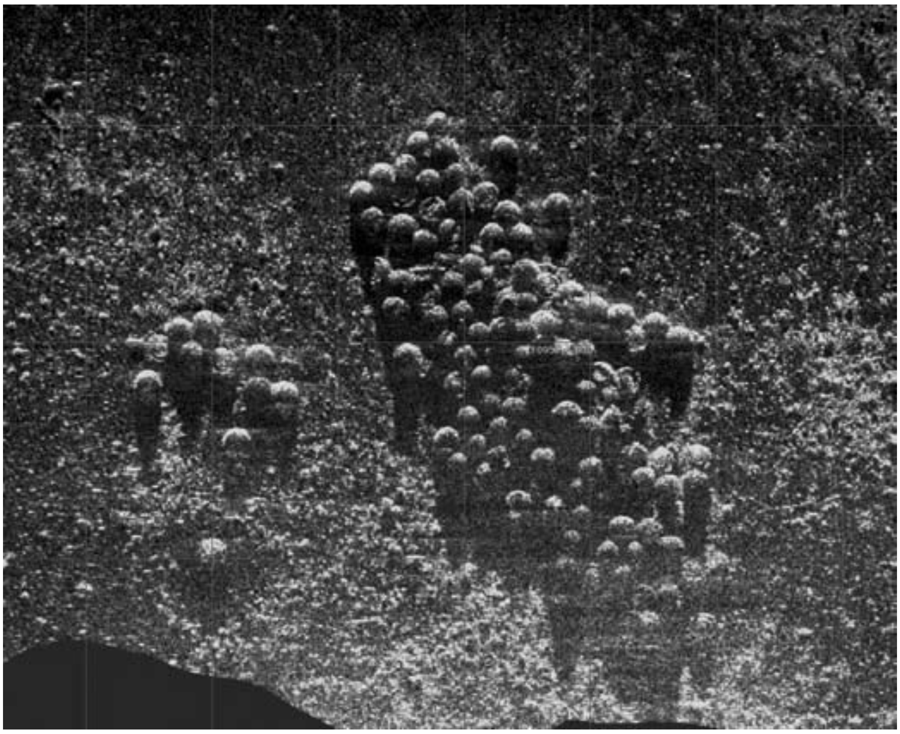

Figure 5.23: Sonar image recorded with HISAS 1030 showing a field of poss-moored mines in the dumping area Kolberger Heide (Frenz, 2014).

More promising and already applied is the use of magnetic sensors as a non-imagery system. The ferromagnetic body of the dumped ammunition causes a change in the earth's magnetic field which can be determined by a magnetometer. Due to the small range of these magnetic anomalies, the magnetometer has to be towed just above the seafloor what can cause problems if there are objects raising from the seafloor up into the water column. In addition, same as for the towed SAS and SSS systems, an appropriate underwater positioning system needs to be installed to ensure a high position accuracy. Also stated as a limitation factor is the fact, that the detected magnetic anomalies only give evidence of the occurrence and approximate size of the object, but further information like the shape of the object required for a classification cannot be provided using only the magnetic data. Even if wrong detections provoked by rocks can be excluded, other ferromagnetic objects like anchors can be unintentionally detected instead. On the current state, the mounting of a magnetometer system to an AUV is possible but due to the engine, a constant and significant influence to the recorded data is noticeable. Irrespective of the introduced influence factors, an offshore magnetometer survey is influenced by various anomalies which requires an intensive post-processing of the data. An example for successfully processed data is shown in Figure 5.24 (Kretschmer and Jans, 2016).

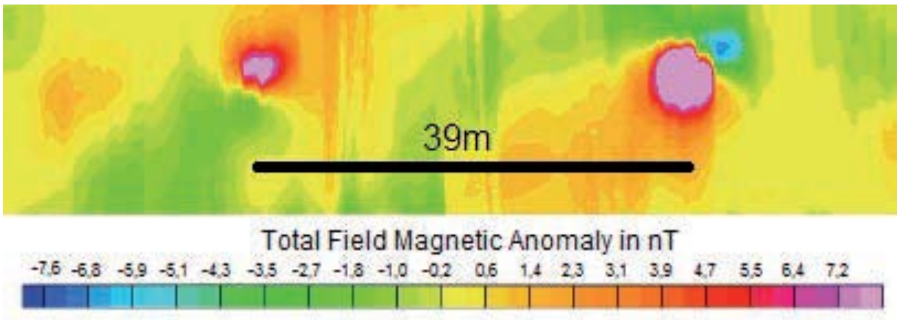

Figure 5.24: Detection of magnetic anomalies for embedded ferromagnetiic objects (Kretschmer and Jans, 2016).

With regard to the conducted base study, both the advantages and disadvantages for the usage of MBES snippet backscatter information should be briefly summarized. Besides the snippet backscatter information also bathymetric data is collected without having any additional effort. The combination of both data offers the possibility to draw conclusions about the situation of potentially sedimentation processes. The fact that the MBES system is mounted directly on the vessel enables the usage of GNSS positioning and therefore to gather data with a high position accuracy. In addition, the vessel is easier to maneuver in comparison to a towed sensor and the data can be collected with a high survey speed. A limitation can be seen in the fact that this kind of detection method is only applicable for shallow water areas. With increasing water depth also the footprint of the swath increases and therefore, less information is provided.

5.5 Plausibility of prospective sedimentation processes

As already indicated within the evaluation of the snippet backscatter images, the ammunition bodies detected in the survey area are mainly located towards the west. Taking into consideration the results of the sediment interpretation, the seafloor in this part shows sediment top layers ranging from clay and silt up to sand. Due to the small grain size of these sediments, they are particularly susceptible for transport processes caused by underwater currents.

Considering the genesis of the Baltic Sea and its present shape as described according to Spielhagen (2012), the only connection to open waters is formed by the Little and Great Belt as well as the Øresund separating Denmark and Sweden. These constrictions affect both the influx of the salty North Sea water and the outflow of the brackish Baltic Sea water. As the North Sea water has a higher density due to its higher salinity, the incoming water causes deep currents whereas the brackish water with a low salinity flows off to the North Sea in the upper water layers. As explained by Mittelstaedt (2003), a direct relation of surface water outflow and deep water influx can be formulated to describe prevailing current conditions: The stronger the outflow of the brackish water, the more powerful is the resulting influx current near the ground. To illustrate this, Figure 5.25 shows the surface and deep currents occurring in the western Baltic Sea.

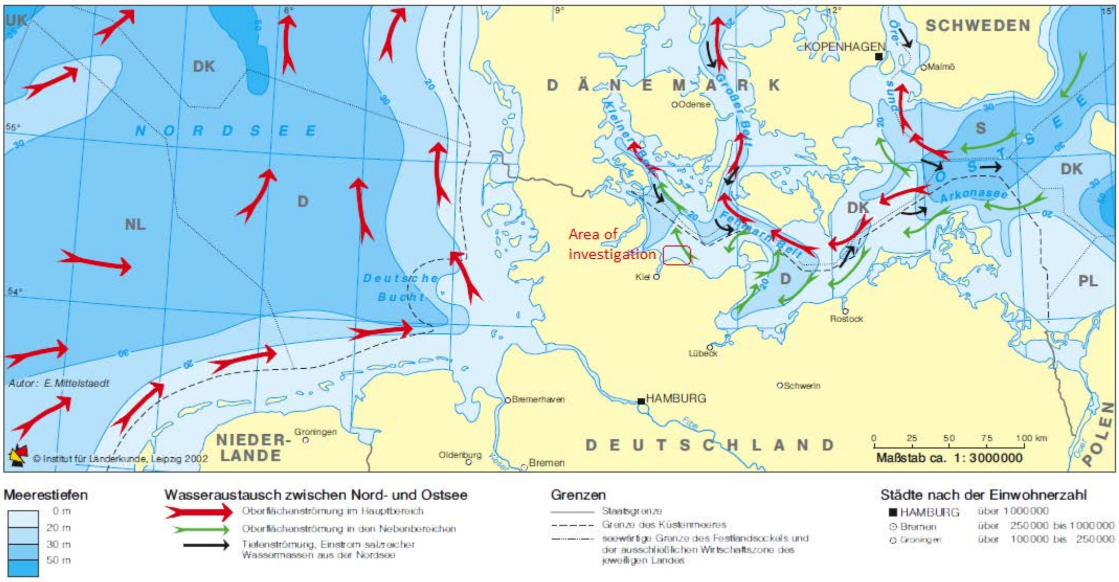

Figure 5.25: Depth distribution and mean circulation of the western Baltic Sea. Red arrows: surface currents (main area), green arrows: surface currents (marginal sector), black arrows: salt water influx (deep water currents). The full size figure can be found in Appendix A (according to Mittelstaedt, 2003).

These processes are directly effected by the prevailing weather conditions and therefore also by the ongoing climate change which is a current research subject of the BALTEX office[24] (Norddeutsches Klimabüro, Internationales BALTEX Sekretariat, 2012). According to their present state of the research, a warming coupled with stronger precipitation can be predicted for the Baltic Sea area. Combining the oceanographic background explained by Mittelstaedt (2003) and the long term changes of the weather conditions predicted by the BALTEX research, a prospective increase of both surface and deep currents can be expected. Thereby, these currents do not evenly occur as they are also effected by the seafloor morphology and the proximity to the connecting channels.

[24] The Baltic Sea Experiment (subsequently referred to BALTEX) as the international research network with its focus on the analysis and modelling of physical, chemical, and biological conditions in terms of the climate change (Norddeutsches Klimabüro, Internationales BALTEX Sekretariat, 2012).

As shown in Figure 5.25, the shallow sea area of the Kolberger Heide is mostly affected by the currents within the upper water layers with a flow direction following the coastline in northwest direction. With regard to the presented sediment arrangement, this may lead to an increased transport of sandy material towards the ammunition bodies. Over recent years, the burial of ammunition bodies caused impairments of salvage or disablement procedures as described by Böttcher et al. (2014) and Böttcher et al. (2015). This requires a high level of time and effort which in turn leads to increasing costs for the removal or rearrangement.

The performed analyses within this thesis in connection with the presented scientifically founded facts support the statements regarding the sedimentation processes. Therefore, to give detailed, area-based information according to the presence of currents effecting the dumped ammunition bodies, a monitoring with an acoustic Doppler current profiler in conjunction with periodic MBES surveys would be a sensible option. The information about the local current velocities and the sediment transport can give disclosures which can directly be checked by possible monitored changes within the morphology and objects located on the seafloor. Moreover, an investigation of possible burial processes can also be of interest with regard to the studies dealing with the release of chemical components to the environment as this affects the marine life as indicated in the beginning of this thesis.

6 Conclusion and outlook

The central issue addressed by the present thesis was the suitability of snippet backscatter information collected with a vessel-based high frequency MBES for the accurate detection of ammunition bodies of different sizes dumped in shallow coastal waters. By means of the analysis of GNSS information, a possibility to improve the current lack of position accuracy should be pointed out. The previous chapters have presented theoretical and practical background information as well as the baseline study conducted within the scope of the research cruise AL447 in October 2014 and its results.

Taking the evaluation of 20 randomly selected objects within the investigated area as a basis, it could be established that the snippet backscatter information collected with an EM 2040C MBES is quite suitable for object detection. A verification was facilitated by means of the Tactical Map maintained by the German Navy which offers besides the ammunition type also the dimensions and the charted position. In turn, the charted position serves as the starting point for the comparison of the position accuracy. In contrast to the previously used sonar technology and the associated underwater positioning, the vessel-based GNSS installation offers a significant increase. Whereas the absolute positioning offers an accuracy of 0.64 m, the application of DGNSS using SAPOS® corrections is able to provide a position accuracy up to 0.08 m. This positioning precision in combination with the feasible snippet backscatter information enables long term monitoring to be conducted by vessel-based high frequency MBES interacting with an installed GNSS positioning system.

Considering the post-processed snippet backscatter images, further improvements are preferable. It has been found that, comparing the not geographically referenced waterfall display during the data acquisition with the display of the mosaic image after post-processing of the data, a much better resolution is achieved in the images shown during the acquisition. For clarification, the contact to the appropriate manufacturer is already made, so that in a long term an improvement of this issue can be expected. Nevertheless, in comparison to other acquisition equipment like SSS, SAS or magnetometer, the MBES snippet backscatter offers a promising alternative at least from the scientific perspective. As military applications have partly different requirements to the type of execution, the vessel-based method using MBES snippet backscatter information with its positioning accuracy will have problems to gain a foothold.

The assessment of the addressed sedimentation processes is also focused by the body of experts as stated in Böttcher et al. (2015) and provides a framework for future investigations. From the hydrographic point of view, a long term monitoring using an acoustic doppler current profiler can be considered as a reasonable measure. The observed data can be used for the determination of the flow direction as well as the occurring sediment transports and thus permits conclusions concerning planned clearance strategies.

In May 2016, the cooperative project UDEMM was initiated by the GEOMAR Helmholtz Centre for Ocean Research, Kiel, the Leibniz Institute for Baltic Sea Research, Warnemünde, and the Christian Albrechts-University, Kiel. Within the scope of this three-year project, an environmental monitoring of ammunition delaboration procedures should be implemented. Using acoustic, visual, and chemical studies, future-oriented methods, techniques, and strategies for the mentioned environmental monitoring should be developed to ensure a long term benefit both for the environmental and the economic point of view. Furthermore, the body of experts "Munition im Meer" will unswervingly continue their path to inform professionals and public to raise the awareness of the issue of dumped ammunition in German coastal waters and their deep impact in economic and ecological matters.

Bibliography and references

Literature

Bauer, M., 2011: Vermessung und Ortung mit Satelliten. Globale Navigationssatellitensysteme (GNSS) und andere satellitengestützte Navigationssysteme. Sixth Edition. Wichmann: Berlin, Offenbach, 479 pp.

Blondel, P., 2009: The Handbook of Sidescan Sonar. Springer: Berlin, Heidelberg, 316 pp.

Böttcher, C., Knobloch, T., Rühl, N.-P., Sternheim, I., Wichert, I., Wöhler, J., 2011: Munitionsbelastung der deutschen Meeresgewässer - Bestandsaufnahme und Empfehlungen. German Maritime and Hydrographic Agency (Eds.), published by themselves: Hamburg, 174 pp.

Böttcher, C., Knobloch, T., Sternheim, J., Wichert, I., Wöhler, J., 2014: Munitionsbelastung der deutschen Meeresgewässer - Entwicklungen und Fortschritt (Jahr 2013). MELUR (Eds.), published by themselves: Kiel, 47 pp.

Böttcher, C., Knobloch, T., Sternheim, J., Weinberg, I., Wichert, I., Wöhler, J., 2015: Munitionsbelastung der deutschen Meeresgewässer - Entwicklungen und Fortschritt (Jahr 2014). MELUR (Eds.), published by themselves: Kiel, 72 pp.

Ehlers, J., Hughes, P.D., Gibbard, P.L., 2016: The Ice Age.Wiley-Blackwell: Chichester, 560 pp.

Frenz, U., 2014: Autonome Unterwasserfahrzeuge mit SAS-Technologie. Neue Möglichkeiten in der zivilen und militärischen Anwendung. In: Deutsche Hydrographische Gesellschaft e.V. (Eds.): Hydrographische Nachrichten. HN 97 – Februar 2014: Rostock, 11-16.

Godin, A., 1998: The Calibration of Shallow Water Multibeam Echo-Sounding Systems. M.Eng. report, Department of Geodesy and Geomatics Engineering Technical Report No. 190, University of New Brunswick, Fredericton, New Brunswick, Canada, 200 pp.

Hare, R., 1995: Depth and Position Error Budgets for Multibeam Echosounding. In: International Hydrographic Review, Monaco (Eds.), Number 77(2), published by themselves: Monaco, 37-69.

Hartl, P., Thiel, K.-H., 1984: Das NAVSTAR Global Positioning System (GPS). In:Schödlbauer, A., Welsch, W. (Eds.): Beiträge zum Geodätischen Seminar 24./25. September 1984.Schriftenreihe des Wissenschaftlichen Studiengangs Vermessungswesen in der Hochschule der Bundeswehr München. Heft 15: München, 329-359.

Herlihy, D.R., Hillard, B.F., Rulon, T.D., 1989: National Oceanic and Atmospheric Administration Sea Beam System 'Patch Test'. In: International Hydrographic Review, Monaco (Eds.), Number 66(2), published by themselves: Monaco, 119-139.

Hughes Clarke, J.E., 2003: Dynamic Motion Residuals in Swath Sonar Data: Ironing out the Creases. In: International Hydrographic Review, Monaco (Eds.), Number 4(1), published by themselves: Monaco, 6-23.

IHO, 2005: Manual on Hydrography. Publication C-13. First Edition. Published by the International Hydrographic Bureau: Monaco, 558 pp.

IHO, 2008: IHO Standards for Hydrographic Surveys. Special Publication N° 44. Fifth Edition. Published by the International Hydrographic Bureau: Monaco, 36 pp.

IHO, 2009: 4th Extraordinary International Hydrographic Conference Monaco, 2-4 June 2009. Report of Proceedings. Published by the International Hydrographic Bureau: Monaco, 406 pp.

Jackson, D.R., Winebrenner, D.P., Ishimaru, A., 1986: Application of the composite roughness model to high-frequency bottom backscattering. In: Journal of the Acoustical Society of America (Eds.). Number 79(5), published by themselves: Melville, 1410-1422.

Jans, W., Reuter, M., Behringer, S., Bohlmann, S., 2012: Probing the seafloor in order to find dumped ammunition and other hazardous materials. In: Aschenbruck, N., Martini, P., Meier, M., Tölle, J. (Eds.): Future Security. 7th Security Research Conference. Springer: Berlin, Heidelberg, 315-326.

Kretschmer, U., Jans, W., 2016: Ortung von Altmunition im Meer. Beiträge aus der Forschungsarbeit der WTD 71. In: Deutsche Hydrographische Gesellschaft e.V. (Eds.): Hydrographische Nachrichten. HN 103 – Februar/März 2016: Rostock, 12-21.

Lurton, X., 2010: An Introduction to Underwater Acoustics. Principles and Applications. Second Edition, Springer: Berlin, Heidelberg, 682 pp.

Magaard, L., 1974: Wasserstandsschwankungen und Seegang. In: Magaard, L., Rheinheimer, G. (Eds.): Meereskunde der Ostsee. Springer: Berlin, Heidelberg, 67-76.

Martinez Diaz, J.V., 2000: Analysis of Multibeam Sonar Data for the Characterization of Seafloor Habitats. Master thesis at University of New Brunswick: New Brunswick, 138 pp.

Miller, C.L., Laflamme, R.A., 1958: The digital terrain model - theory and application. In: Massachusetts Institute of Technology (Eds.): Photogrammetric Engineering, Number 117, published by themselves: Cambridge, 433-442.

Misra, P., Enge, P., 2012: Global Positioning System. Signals, Measurements, and Performance. Revised Second Edition. Ganga-Jamuna Press: Lincoln, 569 pp.

Mittelstaedt, E., 2003: Nord- und Ostsee: Gezeiten, Strömungen, Wasserschichten. In: Leibniz-Institut für Länderkunde e.V. (Eds.): Bundesrepublik Deutschland Nationalatlas. Relief, Boden, Wasser. Band 2, published by themselves: Leipzig, 118-119.

Norddeutsches Klimabüro, Internationales BALTEX Sekretariat, 2012: Ostseeküste im Klimawandel. Ein Handbuch zum Forschungsstand. Second Edition. Published by themselves, Geesthacht: 62 pp.

Ona, E., 1999: Methodology for Target Strength Measurements. ICES Coor´perative Research Report Number 235. International Council for the Exploration of the Sea: Copenhagen, 65 pp.

Open University, 1999: Waves, Tides and Shallow-Water Processes. Second Edition, Butterworth-Heinemann: Oxford, 227 pp.

Rabinovich, A.B., 2009: Seiches and Harbour Oscillations. In: Kim, Y.C. (Eds.): Handbook of Coastal and Ocean Engineering. World Scientific Publishing Company: Singapoure, 193-236.

Robl Matzen, S., 2010: Der Schwedisch-Dänische Krieg 1643-45. In:Fiebig, E.S., Schlürmann, J. (Eds.): Handbuch zur nordelbischen Militärgeschichte. Heere und Kriege in Schleswig, Holstein, Lauenburg, Eutin und Lübeck 1623-1863/67. Husum: Husum, 309-326.

Schiller, L., 2012: Vermessung der Hydrographie - Eine umfassende Definition der Disziplin samt Untergliederung. In: Arbeitskreis 3 "Messmethoden und Systeme" (Eds.): Das Meer schützen und nutzen. Beiträge zum 111. DVW-Seminar und zum 26. Hydrographentag vom 11. bis 13. Juni 2012 in Husum. Band 67/2012, Wißner: Augsburg, 21-44.

Schneider von Deimling, J., 2015: R/V ALKOR Cruise Report AL447. Controls on methane seepage in the Baltic Sea. GEOMAR Helmholtz Centre for Ocean Research: Kiel, 41 pp.

Seiß, G., 2015: Das Ostseemodell der BAW. Technische Dokumentation Stand Januar 2015. Federal Waterways Enigneering and Research Institute (Eds.), published by themselves, 37 pp.

Theuillon, G., Stephan, Y., Pacault, A., 2008: High-Resolution Geoacoustic Characterization of the Seafloor Using a Subbottom Profiler in the Gulf of Lion. In: IEEE Journal of Oceanic Engineering (Eds.), Number 33(3), published by themselves, 240-253.

Wunderlich, J., Wendt, G., Müller, S., 2005: High-resolution echo-sounding and detection of embedded archaeological objects with nonlinear sub-bottom profilers. In: Urgeles, R., Chi, W.-C. (Eds): Marine Geophysical Researches, Number 26, Springer: Netherland, 123-133.

Internet sources

BAAINBw, 2016: Portrait of WTD71. `http://www.baainbw.de/portal/a/baain/!ut/p/c4/04_SB8K8xLLM9MSSzPy8xBz9CP3I5EyrpHK9pMTEzDy9lMzUvOKSYr3ykhRzQ72C_KKSosRM_XCQtpx0_cjUPP2C3FxHAHddK6k!/` (last visit on 2016-05-02).

CARIS, 2016: HIPS and SIPS. `http://www.caris.com/products/hips-sips/` (last visit on 2016-02-23).

GEBCO, 2016: General Bathymetric Chart of the Ocean. `http://www.gebco.net/data_and_products/gridded_bathymetry_data/` (last visit on 2016-01-15).

GEOMAR, 2012: ALKOR. `http://www.geomar.de/typo3temp/pics/Alkor_Titel_fe8f858a6c.jpg` (last visit on 2016-03-17).

GEOMAR, 2013a: F.S. "ALKOR" Vorgeschichte, Bau und Ausrüstung. `http://www.geomar.de/de/zentrum/einrichtungen/wasser/f-s-alkor-alt/vorgeschichte-bau-und-ausruestung-alkor/` (Last visit on 2016-02-25).

GEOMAR, 2013b: Geschichte der Meeresforschung in Kiel.`http://www.geomar.de/zentrum/ueber-uns/geschichte/text/` (Last visit on 2016-02-25).

GEOMAR, 2014: Submarine Gas Hydrate Reservoirs. `http://www.geomar.de/en/research/fb2/fb2-mg/projects/sugar-2-phase/` (last visit on 2016-03-17).

GEOMAR, 2016: Sub-seabed CO_2 Storage: Impact on marine ecosystems. `http://www.eco2-project.eu/about-eco2.html` (last visit on 2016-03-17).

Hammerstad, E., 2000: EM Technical Note. Backscattering and Seabed Image Reflectivity. http://www.km.kongsberg.com/ks/web/nokbg0397.nsf/AllWeb/C2AE0703809C1FA5C1257B580044DD83/$file/EM_technical_note_web_BackscatteringSeabedImageReflectivity.pdf?OpenElement (last visit on 2016-03-12), 5 pp.

Leipe, T., Moros, M., Tauber, F., 2011: Die Geschichte der Ostsee. http://io-warnemuende.de/geschichte-der-ostsee-2489.html (last visit on 2016-02-26).

Lemke, W., 2005: Die kurze und wechselvolle Entwicklungsgeschichte der Ostsee. http://www.io-warnemuende.de/die-entwicklungsgeschichte-der-ostsee.html (last visti on 216-02-26).

NABU Schleswig-Holstein, 2016: Die "Kolberger Heide" in der Kieler Außenförde. Ein munitionsbelastetes, "unreines Meeresgebiet". https://schleswig-holstein.nabu.de/natur-und-landschaft/aktionen-und-projekte/munition-im-meer/miremar/07328.html (last visti on 216-02-26).

National Instruments, 2013: AC and DC Coupling. http://www.ni.com/white-paper/14753/en/ (last visit on 2016-04-08).

QPS, 2016: Howto Calibrate a Multibeam Echosounder. https://confluence.qps.nl/display/KBE/Howto+Calibrate+a+Multibeam+Echosounder (last visit on 2016-03-20).

SAPOS GeoNord, 2015: Location of SAPOS base stations. http://www.sapos.geonord.de/geopp_gnweb/gnweb.html (last visit on 2015-12-16).

Spielhagen, R., 2012: Die Entstehung der Ostsee. http://www.geomar.de/de/entdecken/artikel/article/die-entstehung-der-ostsee/ (last visit on 2016-02-26).

TenneT TSO GmbH, 2014: 57 Millionen Euro für 30 Tonnen Munition: TenneT schließt Windpark Riffgat an. http://www.tennet.eu/de/index.php?id=52&tx_ttnews[tt_news]=517 (last visit on 2016-04-04).

Technical documentation

CARIS, 1014: CARIS HIPS and SIPS 8.1 User guide, 572 pp.

Coda Octopus Ltd., 2006: Product Sheet F180 series. 2 pp.

Coda Octopus Products Ltd., 2012: MOTION INSight. User and Reference Guide. Version 1.1.0. 82 pp.

Coda Octopus Products Ltd., 2013: F180R series. User & Reference Guide. Version 4.2.0, 175 pp.

Gurtner, W., 2007: RINEX. The Receiver Independent Exchange Format. Astronomical Institute of the University of Bern: Version 3.00: 40 pp.

Innomar Technologie GmbH, 2009a: SES-2000 Narrow-Beam Parametric Sub-Bottom Profilers. User's Guide. Version 2.8, 246 pp.

Innomar Technologie GmbH, 2009b: ISE 2.9.2. Post Processing Software for the Parametric Sediment Echo Sounder SES-96 ans SES-2000. User's Guide. Software Version 2.9.2, 96 pp.

Institut für Meereskunde, 1989: Generalplan des Forschungsschiffes ALKOR. Technical drawing 000-144-001, prepared by Lasse + Pache Ingenieurtechnik GmbH, Bremen.

Interactive Visualization Systems Inc., 2011: Fledermaus Reference Manual. Version 7, 471 pp.

Kongsberg Maritime AS; 2010: HISAS 1030. High resolution interferometric synthetic aperture sonar, 11 pp.

Kongsberg Maritime AS, 2013a: Kongsberg EM 2040C Multibeam echo sounder. Product Description, 60 pp.

Kongsberg Maritime AS, 2013b: Seafloor Information System SIS. Reference manual for EM2040C. Version 4.0, 596 pp.

Kongsberg Maritime AS, 2015: Kongsberg EM Series Multibeam echo sounder. EM datagram formats,132 pp.

NovAtel Inc., 2010: GrafNav/GrafNet User Guide. Version 6, 271 pp.

Appendix A - Charts

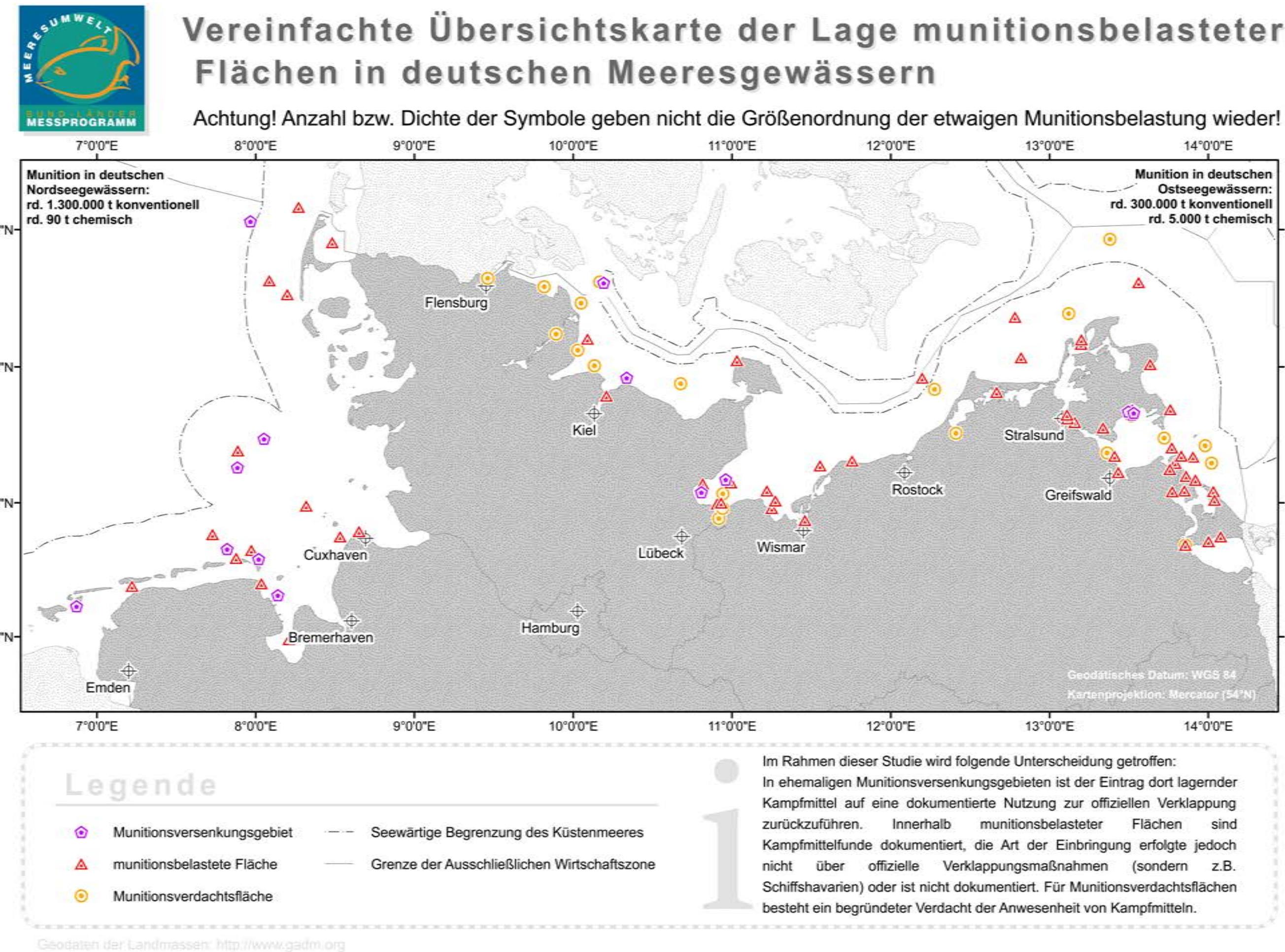

Figure A1: Simplified overview of contaminated areas in German marine waters. Magenta pentagon: ammunition dumping site, red triangle: contaminated area, yellow circle: potentially contaminated area. Continuous line: exclusive economic zone, dotdashed line: territorial sea boundary. Geographical data provided by `http://www.gadm.org` (Böttcher et al., 2011).

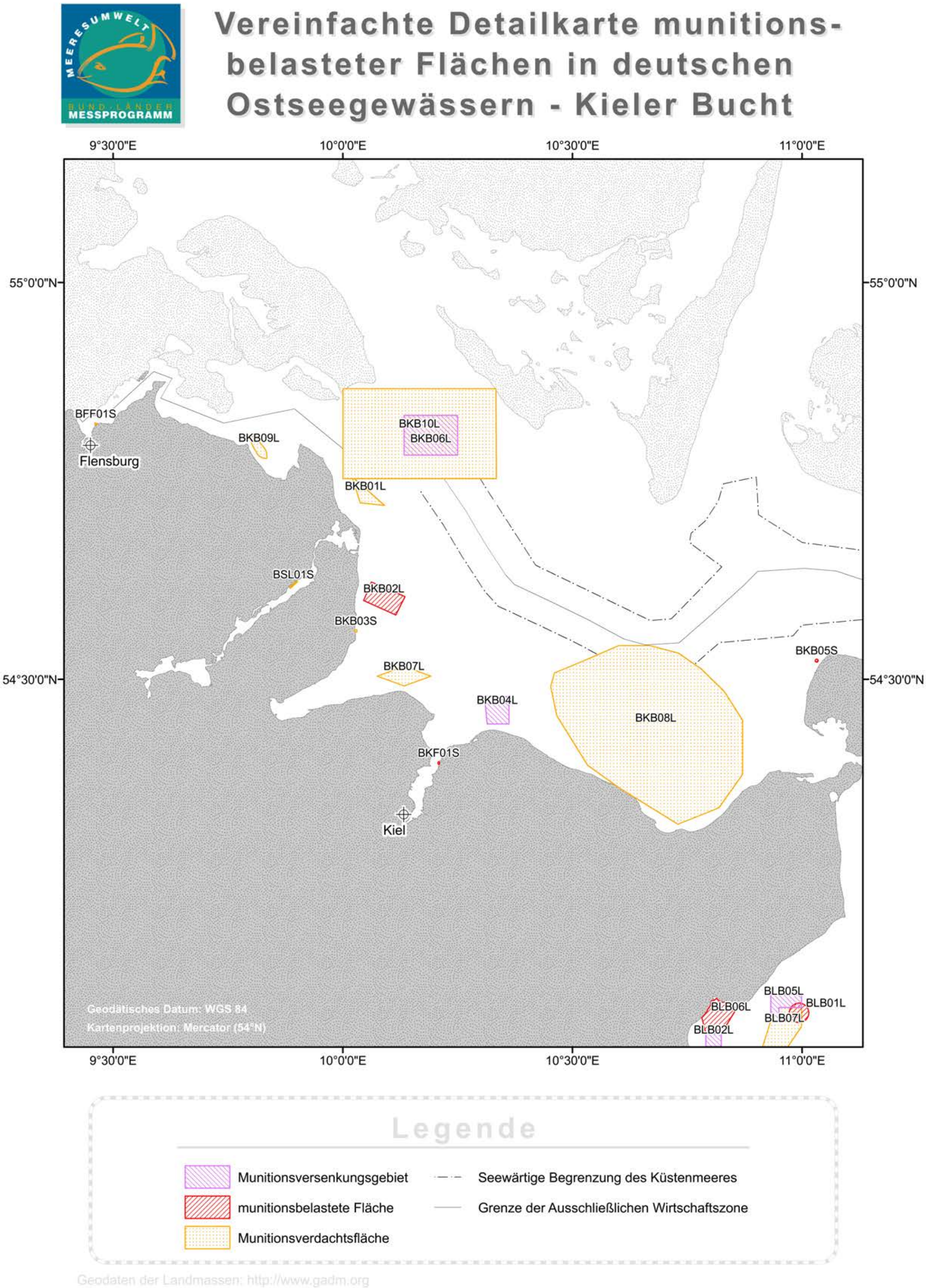

Figure A2: Simplified detail map of contaminated areas in the Kiel Bay. Magenta area: ammunition dumping site, red area: contaminated area, yellow area: potentially contaminated area. Continuous line: exclusive economic zone, dotdashed line: territorial sea boundary. Geographical data provided by `http://www.gadm.org` (Böttcher et al., 2011).

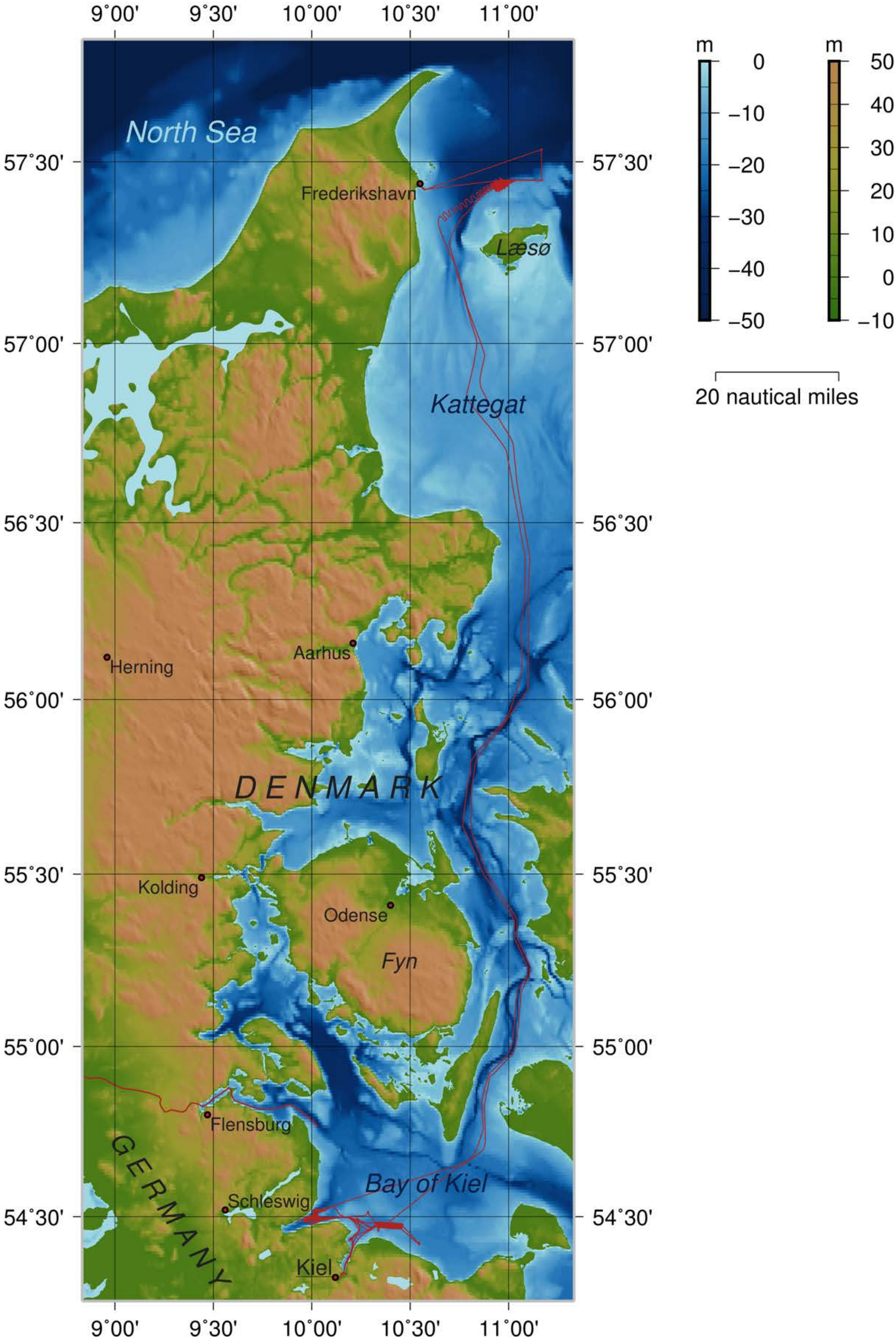

Figure A3: Shiptrack of the RV ALKOR cruise AL447. Mercator projection with global dataset GEBCO 2008 (30 arc-seconds) provided by GEBCO (2016).

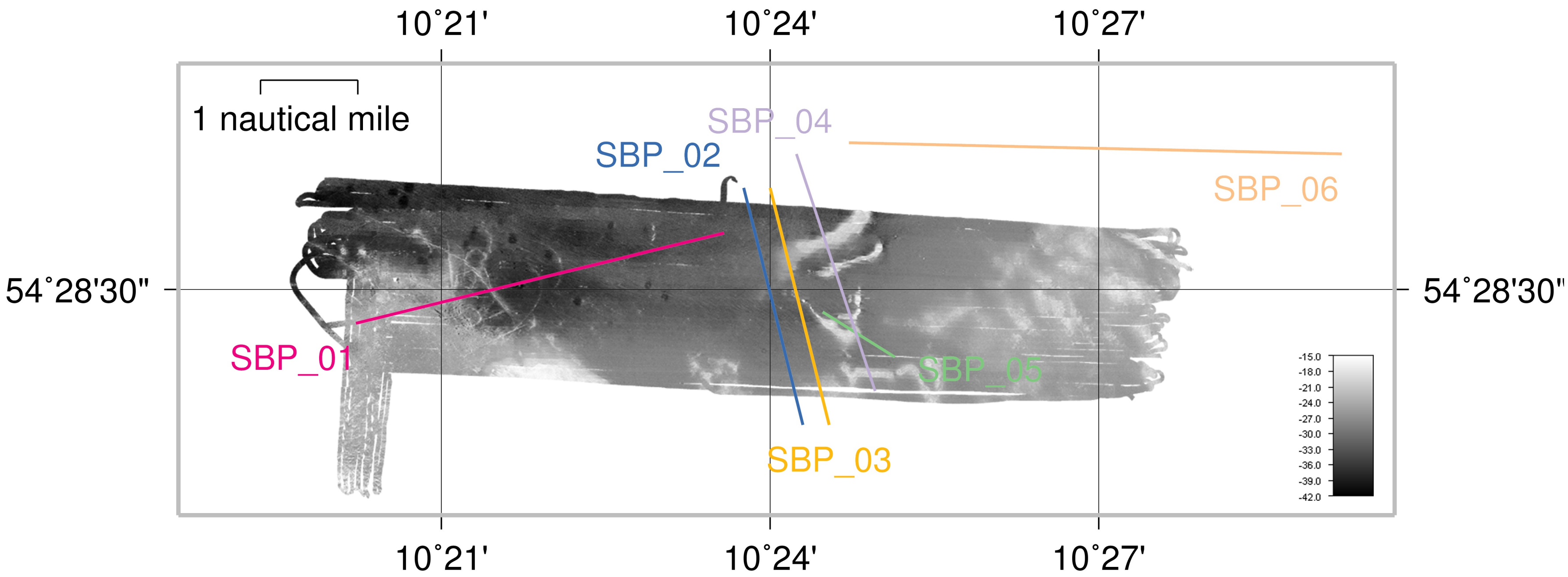

Figure A4: Location of SBP profiles from RV LiTTORINA daytrip. Background: Snippet backscatter image processed with QPS Fledermaus Geocoder (Mosaic pixel size: 0.50 m x 0.50 m). Dark colors represent low backscatter intensities, light colors indicate high backscatter intensities (Values given in dB).

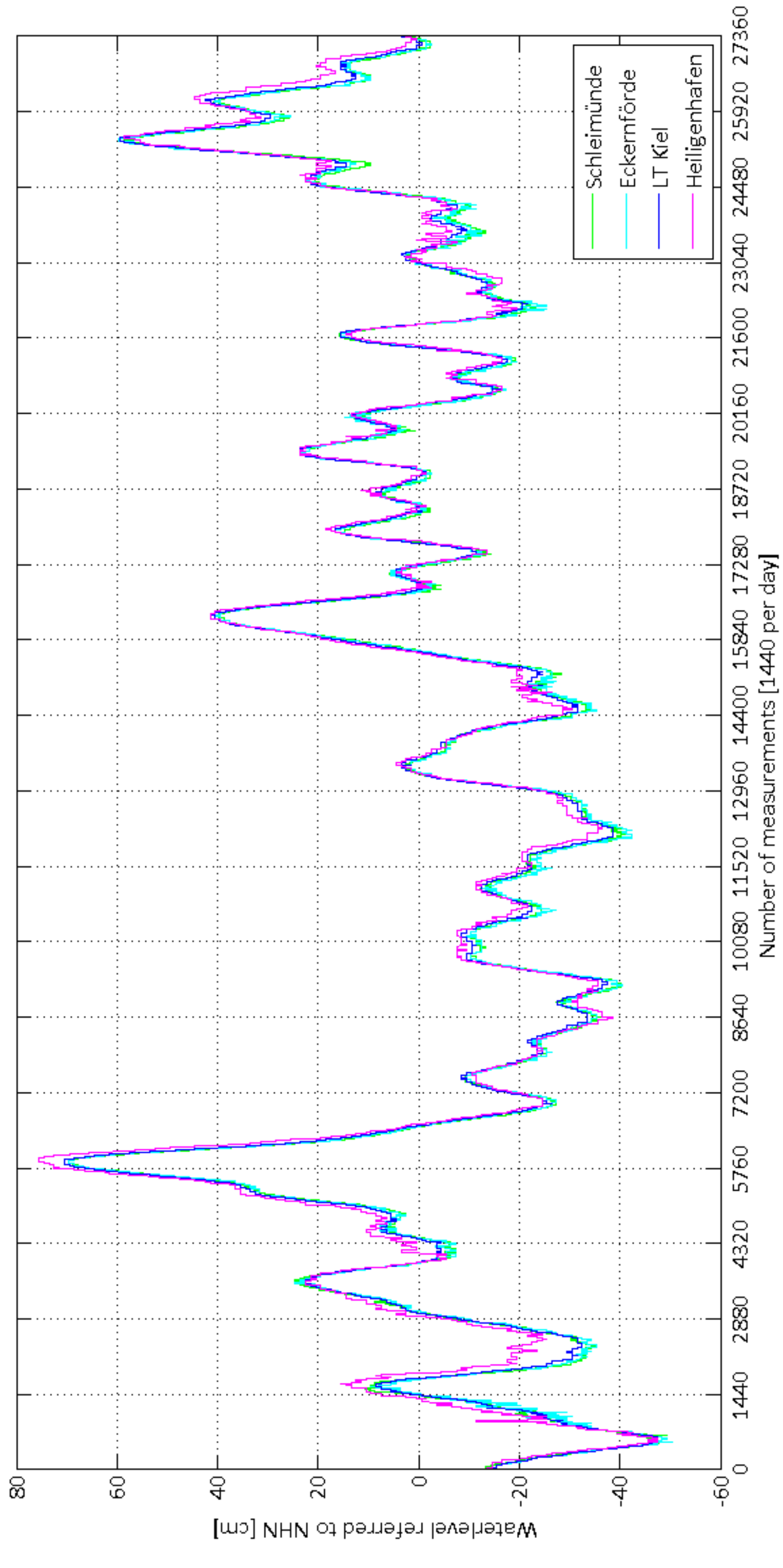

Figure A5: Water level variations logged at tide gauge stations around the dumping site. Water level referred to NHN over a time of 19 days. Data source: WSA Lübeck.

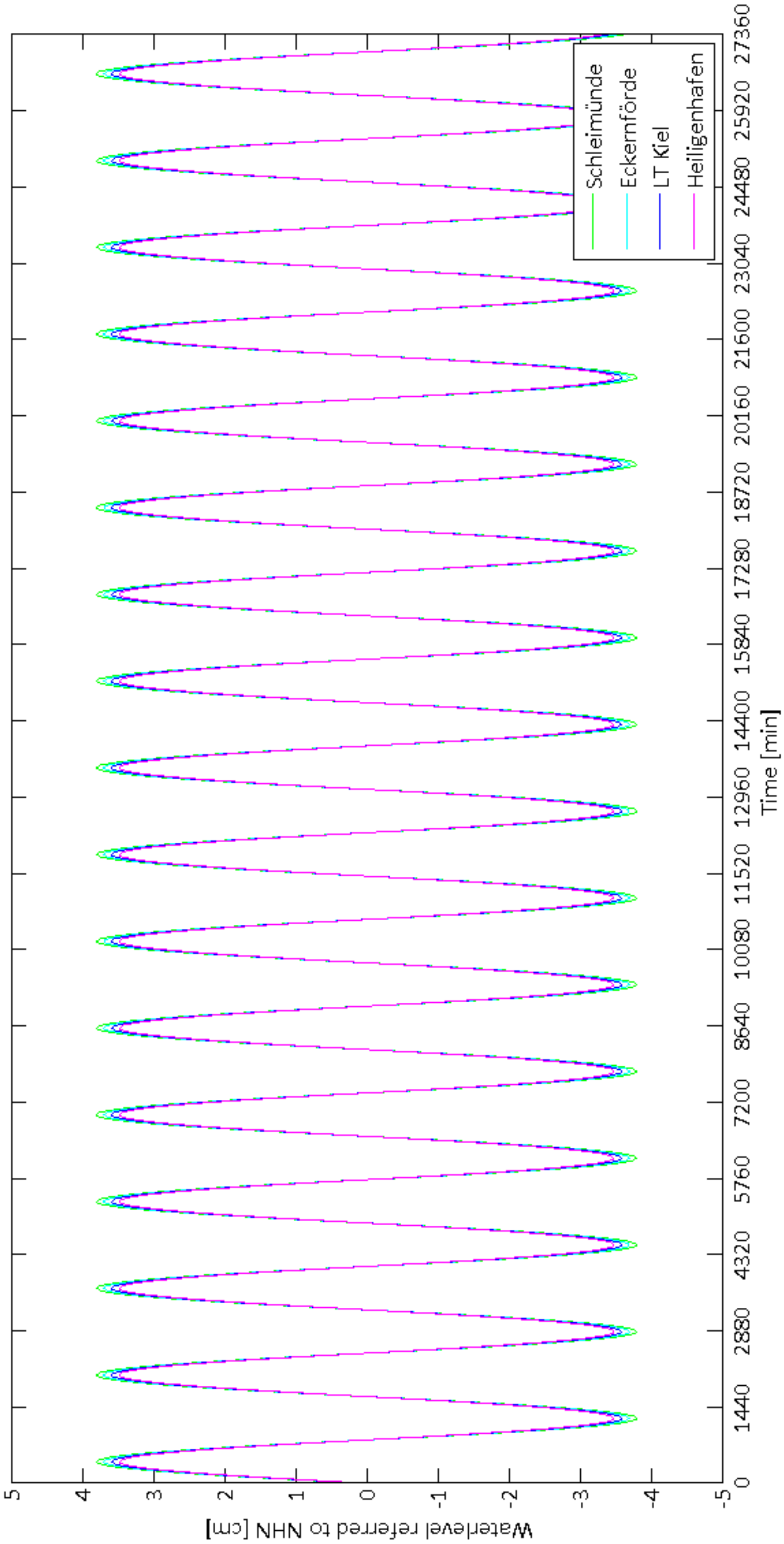

Figure A6: Frequency of a detected first order seiche. Oscillation system: Western Baltic Sea - Gulf of Finland.

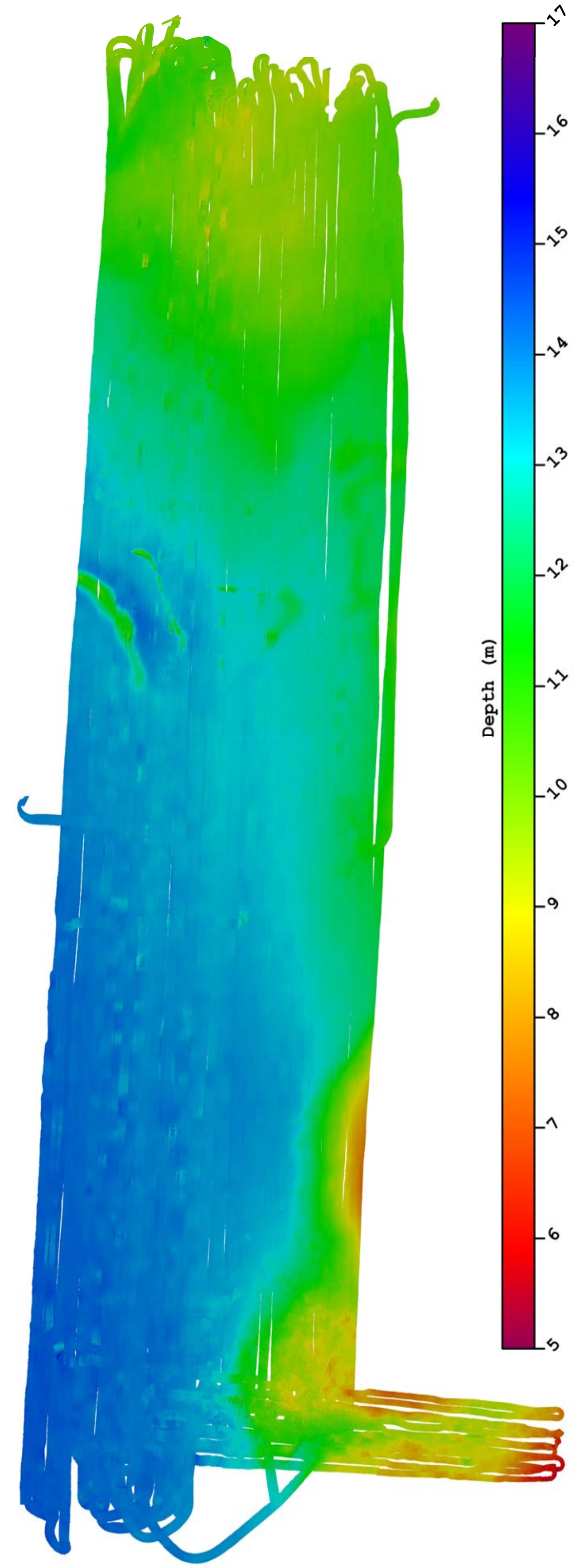

Figure A7: Bathymetric data processed with CARIS HIPS and SIPS 8.1. Grid size of 0.40 m x 0.40 m according to the horizontal TPU.

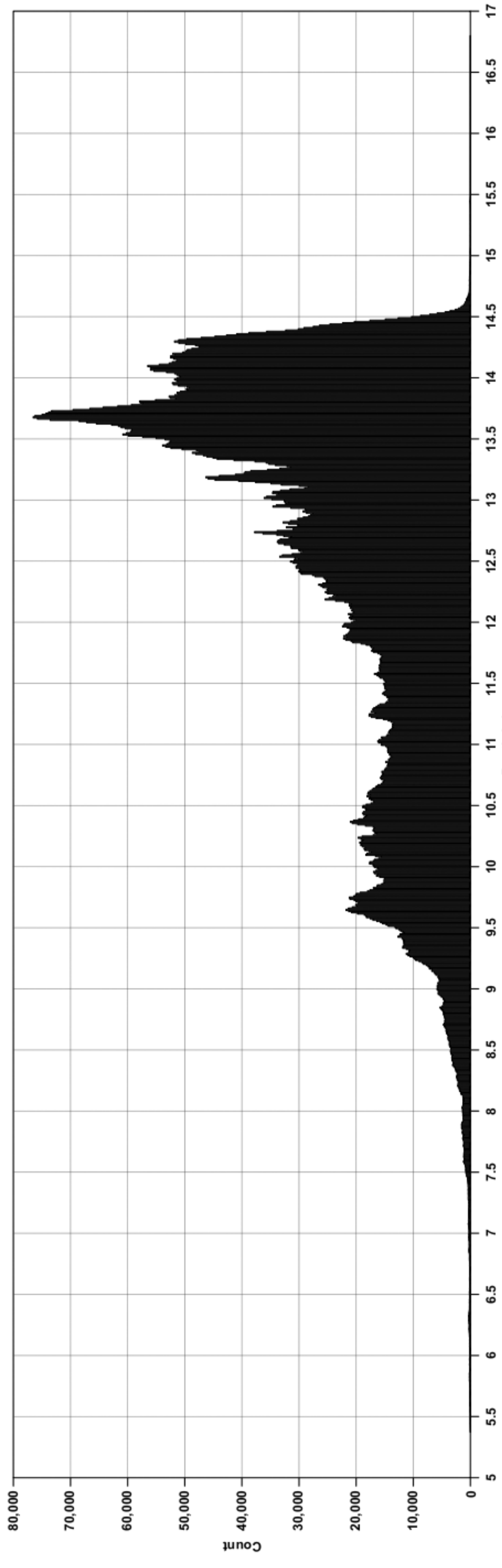

Figure A8: Histogram representing the distribution of depth values.

Figure A9: Snippet backscatter image od the survey area processed with Fledermaus Geocoder 7.3.6. Dark colors represent low backscatter intensities, light colors indicate high backscatter intensities. Values given in dB. Mosaic pixel size: 0.50 m x 0.50 m.

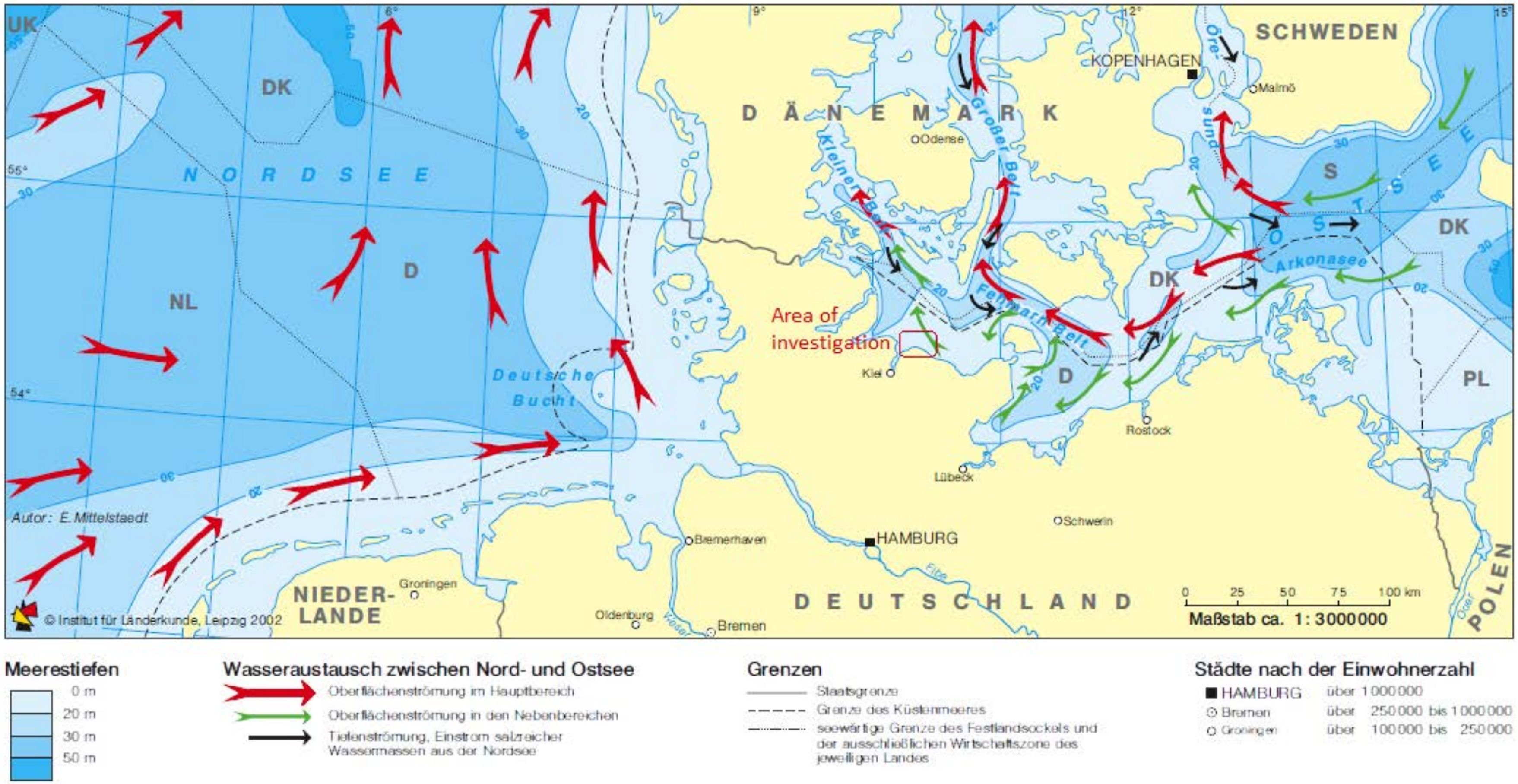

Figure A10: Depth distribution and mean circulation of the western Baltic Sea. Red arrows: surface currents (main area), green arrows: surface currents (marginal sector), black arrows: salt water influx (deep water currents) (according to Mittelstaedt, 2003).

Appendix B - Auxiliary information

```
disk loc: 0x0, length 861, opcode: 0x49
EM 3000 Installation Start Datagram # 1
2014/11/04 10453.92
Main Serial Number: 150
Second Head Serial Number: 0
WLZ=-4.000,SMH=150,STC=1,S1X=0.000,S1Y=0.410,S1Z=0.640,S1H=0.000...

disk loc: 0x361, length 760, opcode: 0x55
SVP Datagram: 2014-11-04, 10453.92
Profile Time: 2014-11-02,    70.02
Number of entries:  91
   0.00:   1459.9
   0.20:   1479.5
   0.40:   1479.6

disk loc: 0x65d, length 52, opcode: 0x52
EM Runtime Parameter Datagram # 1
2014/11/04 10454.08
EM model number: 2045
Min/max Depth:     6.0    40.0
Sounding Mode: 12
Pulselength: 50 uSec,  Xmit/Rec beamwidth:  1.3  1.3
Source of Surface Sound Speed: 0 (From real time sensor)

disk loc: 0x695, length 6460, opcode: 0x4E
Range & Angle 78 Datagram model:  2045  2014-11-04, 10453.982
Number of depths: 400, ping number   59116
Serial Number: 150
Sound velocity: 1480.10
Sampling Frequency: 56561.09
Number of transmit sectors: 1
 #   Tilt   Focus  Sig.Length  Time.Offset  Centre.F  Bandwidth
 0   3.32   19.6       73         0      300000    20000

 #   Sector /  Pointing /  Range (mSec) / Error
  1    0       62.24      47.32      0.0594
  2    0       62.13      47.04      0.0383
  3    0       62.02      46.92      0.0862

disk loc: 0x1fd5, length 8040, opcode: 0x58
XYZ88 Datagram model:  2045  2014-11-04, 10453.982  Depth Datagram # 1
Number of depths: 400, ping number   59116
Serial Number: 150
Sound velocity: 1480.00
Sampling Rate:  56561.1
Transducer depth:    4.58
 #  Across /  Along / Depth / Detection / Ref. (dB) / Quality
 1  -31.72    0.43  14.62    0x01      -43.5    0x1F (P)
 2  -31.50    0.43  14.60    0x01      -35.2    0x14 (P)
 3  -31.39    0.42  14.62    0x01      -40.6    0x2A (P)

disk loc: 0x3f41, length 10296, opcode: 0x59
EM Seabed Image 89 Datagram # 1
2014/11/04 10453.98
Serial Number: 150
total pixels: 3930
```

Figure B1: Extract of an *.all file datagram created with the CARIS HIPS and SIPS 8.1 dump utility: EM 3000 Installation Start Datagram, SVP Datagram, EM Runtime Parameter Datagram, Range & Angle Datagram, Depth Datagram, and EM Seabed Image Datagram.

```
GrafNav Forward Processing Settings
-----------------------------------
SUMREC Ver8.30.2105 NGPS32 Forward Summary
Processed by Unknown, desciption: Run (1)
Time and date is: 17:12:45, 10/31/2011
Waypoint Products Group, Copyright NovAtel Inc., 1992-2011

-------------------------------------------------------------------------
Configuration and processing settings
-------------------------------------------------------------------------

Project settings:
Master 1 : Name 0706305s_Kiel ENABLED
: Antenna SIMPLE_VERT 0.000 m
: File 0706305s_Kiel.gpb
: Position 54 21 19.76000 10 07 55.39150 114.470
Master 2 : Name 0711305s_Bungsberg ENABLED
: Antenna SIMPLE_VERT 0.000 m
: File 0711305s_Bungsberg.gpb
: Position 54 13 01.20450 10 43 06.30100 181.734
Master 3 : Name 0719305s_Westermarkelsdorf ENABLED
: Antenna SIMPLE_VERT 0.000 m
: File 0719305s_Westermarkelsdorf.gpb
: Position 54 31 38.33930 11 03 29.01670 57.623
Remote : Name Remote ENABLED
: Antenna SIMPLE_VERT 0.000 m
: File mobile.gpb
: 0 static sessions
Direction : FORWARD
Process Mode : Dual frequency carrier phase
Static Initial.: Float
Use AR : Yes, Using ARTK
Use Glonass : Yes
```

Figure B2: Configuration and processing settings for Waypoint GrafNav 8.3 forward GNSS processing.

```
GrafNav Reverse Processing Settings
-----------------------------------
SUMREC Ver8.30.2105 NGPS32 Reverse Summary
Processed by Unknown, desciption: Run (1)
Time and date is: 17:12:45, 10/31/2011
Waypoint Products Group, Copyright NovAtel Inc., 1992-2011

-------------------------------------------------------------------------
Configuration and processing settings
-------------------------------------------------------------------------

Project settings:
Master 1 : Name 0706305s_Kiel ENABLED
: Antenna SIMPLE_VERT 0.000 m
: File 0706305s_Kiel.gpb
: Position 54 21 19.76000 10 07 55.39150 114.470
Master 2 : Name 0711305s_Bungsberg ENABLED
: Antenna SIMPLE_VERT 0.000 m
: File 0711305s_Bungsberg.gpb
: Position 54 13 01.20450 10 43 06.30100 181.734
Master 3 : Name 0719305s_Westermarkelsdorf ENABLED
: Antenna SIMPLE_VERT 0.000 m
: File 0719305s_Westermarkelsdorf.gpb
: Position 54 31 38.33930 11 03 29.01670 57.623
Remote : Name Remote ENABLED
: Antenna SIMPLE_VERT 0.000 m
: File mobile.gpb
: 0 static sessions
Direction : REVERSE
Process Mode : Dual frequency carrier phase
Static Initial.: Float
Use AR : Yes, Using ARTK
Use Glonass : Yes
```

Figure B3: Configuration and processing settings for Waypoint GrafNav 8.3 reverse GNSS processing.

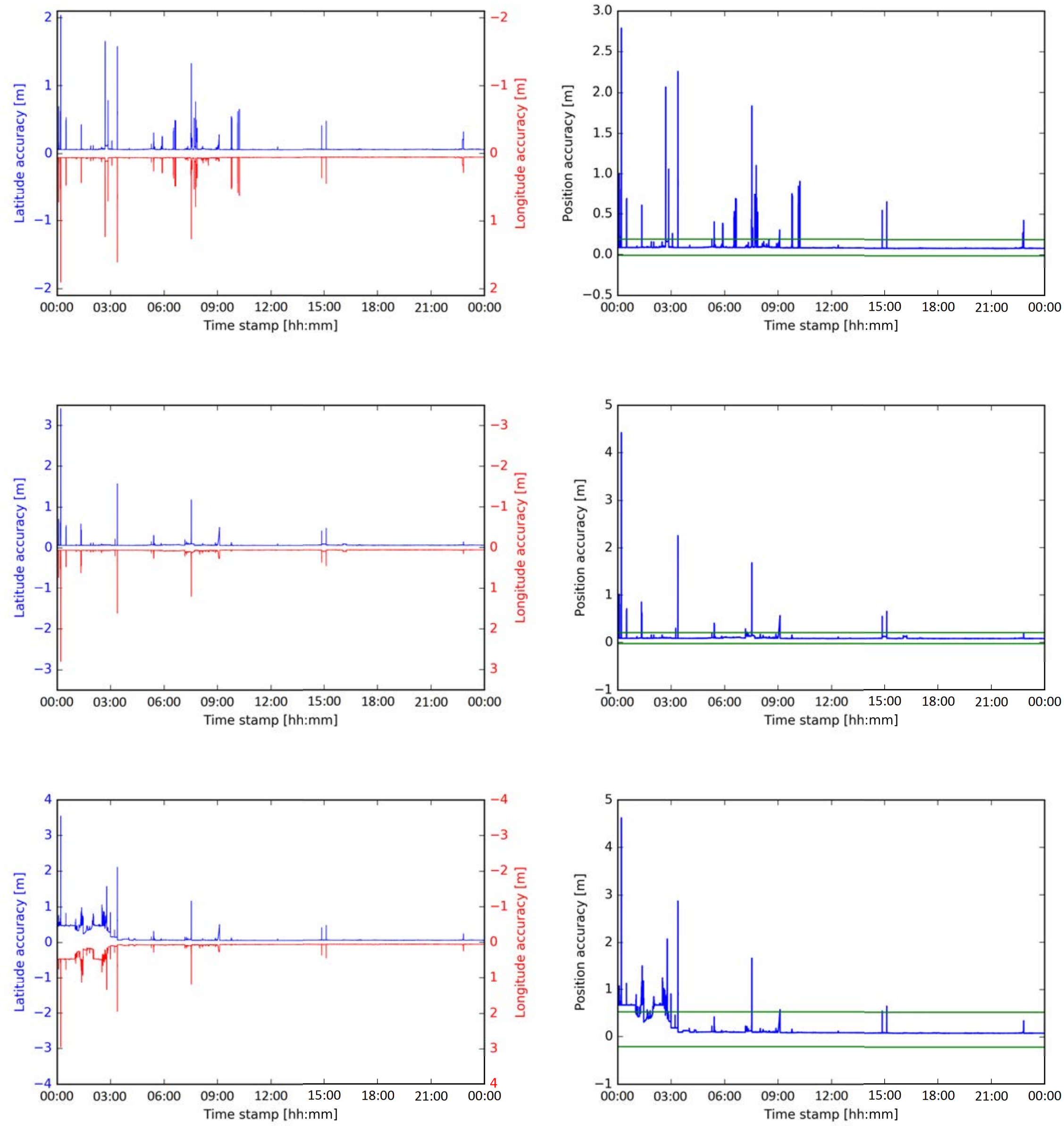

Figure B4: Position accuracy for DGNSS positioning using SAPOS base stations. Accuracy for latitude and longitude position [m] over a period of 24 hours (left) and horizontal position accuracy [m] (right). The green horizontal lines indicate the computed confidence interval. First row: Test series 3 using the SAPOS base station in Kiel, center row: Test series 4 using the SAPOS base station in Bungsberg, bottom row: Test series 5 using the SAPOS base station in Westermarkelsdorf.

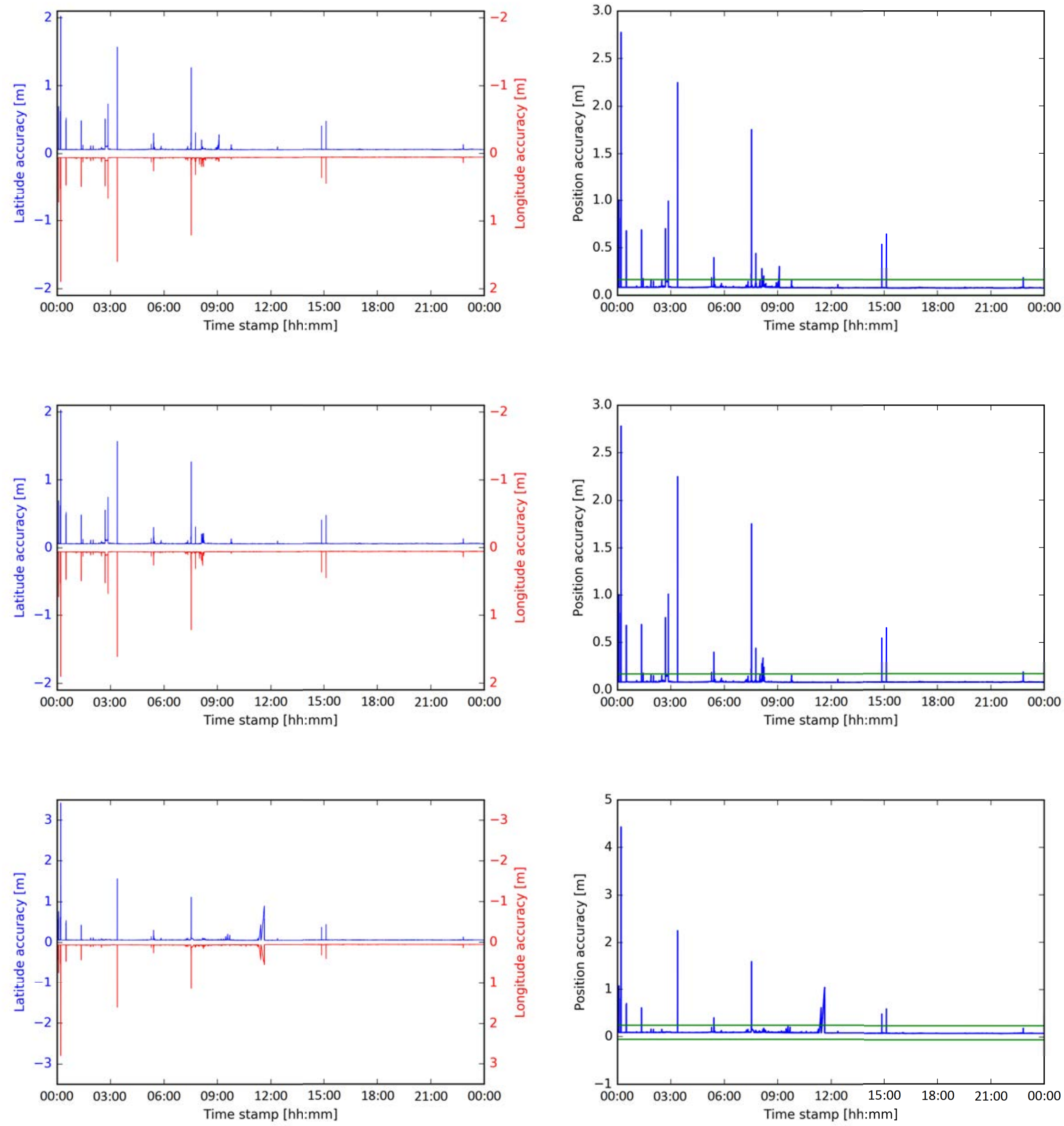

Figure B5: Position accuracy for DGNSS positioning using SAPOS base stations. Accuracy for latitude and longitude position [m] over a period of 24 hours (left) and horizontal position accuracy [m] (right). The green horizontal lines indicate the computed confidence interval. First row: Test series 6 using the SAPOS base stations in Kiel and Bungsberg, center row: Test series 7 using the SAPOS base stations in Kiel and Westermarkelsdorf, bottom row: Test series 7 using the SAPOS base stations in Bungsberg and Westermarkelsdorf.

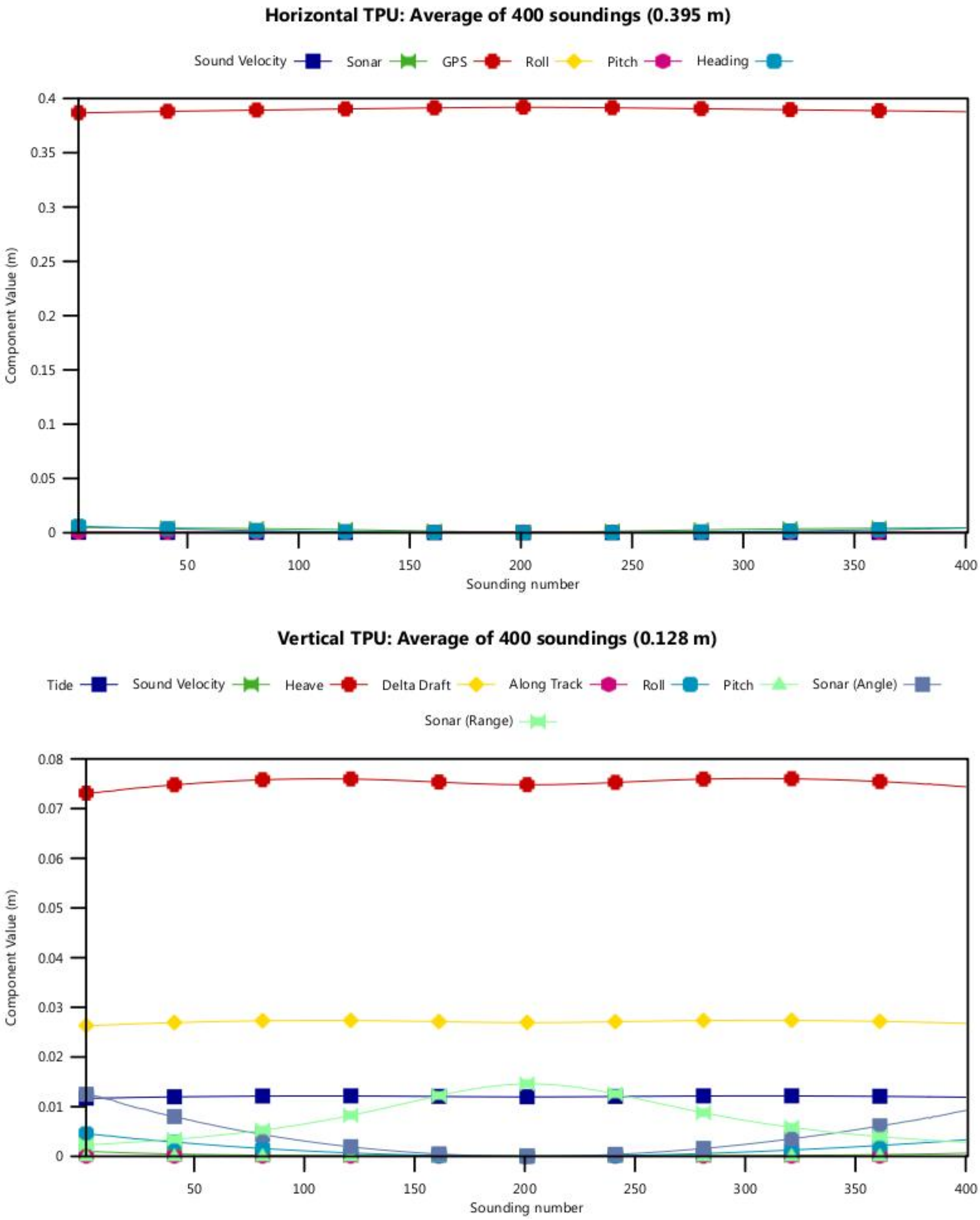

Figure B6: Component values of the horizontal TPU (top) and of the vertical TPU (bottom) for a complete swath (400 soundings) based on CARIS HIPS and SIPS 8.1.

Reference	Order	Special	1a	1b	2
Chapter 1	**Description of areas.**	Areas where under-keel clearance is critical	Areas shallower than 100 metres where under-keel clearance is less critical but *features* of concern to surface shipping may exist.	Areas shallower than 100 metres where under-keel clearance is not considered to be an issue for the type of surface shipping expected to transit the area.	Areas generally deeper than 100 metres where a general description of the sea floor is considered adequate.
Chapter 2	**Maximum allowable THU 95% *Confidence level***	2 metres	5 metres + 5% of depth	5 metres + 5% of depth	20 metres + 10% of depth
Para 3.2 and note 1	**Maximum allowable TVU 95% *Confidence level***	a = 0.25 metre b = 0.0075	a = 0.5 metre b = 0.013	a = 0.5 metre b = 0.013	a = 1.0 metre b = 0.023
Glossary and note 2	***Full Sea floor Search***	Required	Required	Not required	Not required
Para 2.1 Para 3.4 Para 3.5 and note 3	***Feature Detection***	Cubic *features* > 1 metre	Cubic *features* > 2 metres, in depths up to 40 metres; 10% of depth beyond 40 metres	Not Applicable	Not Applicable
Para 3.6 and note 4	**Recommended maximum Line Spacing**	Not defined as *full sea floor search* is required	Not defined as *full sea floor search* is required	3 x average depth or 25 metres, whichever is greater For bathymetric lidar a spot spacing of 5 x 5 metres	4 x average depth
Chapter 2 and note 5	**Positioning of fixed aids to navigation and topography significant to navigation. (95% *Confidence level*)**	2 metres	2 metres	2 metres	5 metres
Chapter 2 and note 5	**Positioning of the Coastline and topography less significant to navigation (95% *Confidence level*)**	10 metres	20 metres	20 metres	20 metres
Chapter 2 and note 5	**Positioning of the Coastline and topography less significant to navigation (95% *Confidence level*)**	10 metres	20 metres	20 metres	20 metres
Chapter 2 and note 5	**Mean position of floating aids to navigation (95% *Confidence level*)**	10 metres	10 metres	10 metres	20 metres

Figure B7: IHO minimum standards for hydrographic surveys (IHO, 2008).

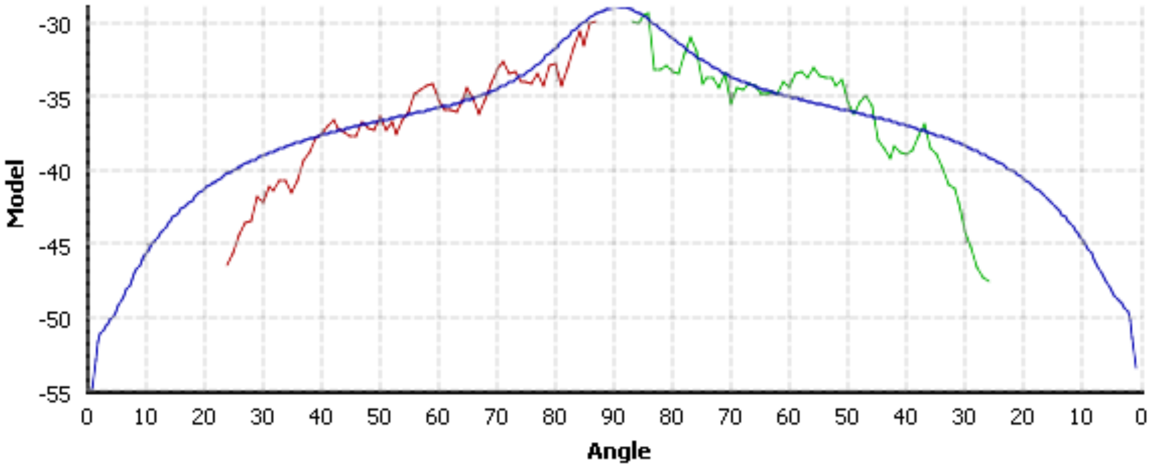

Figure B8: Beam pattern for clay sediment generated with QPS Fledermaus Geocoder 7.3.6. Blue curve: modeled response, red/green curve: measured response.

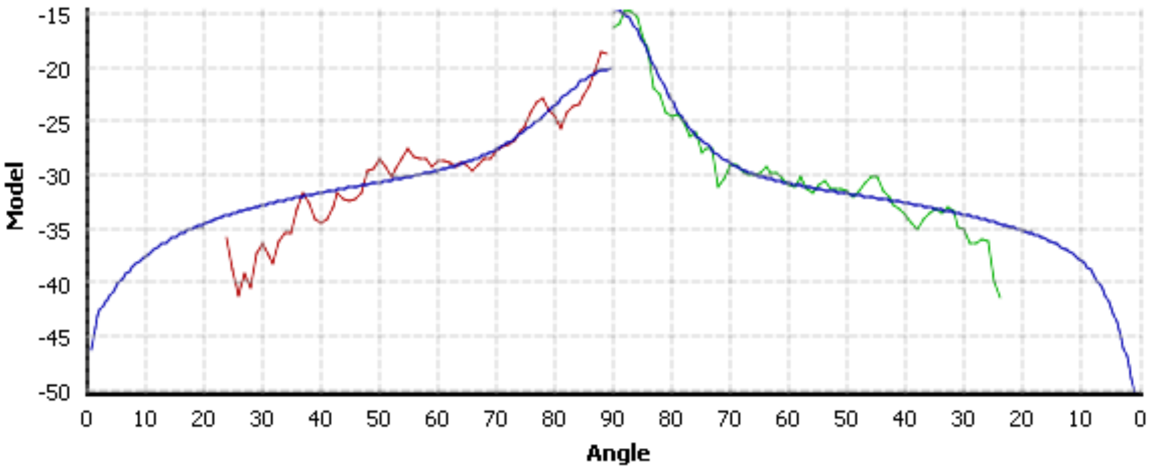

Figure B9: Beam pattern for coarse silt sediment generated with QPS Fledermaus Geocoder 7.3.6. Blue curve: modeled response, red/green curve: measured response.

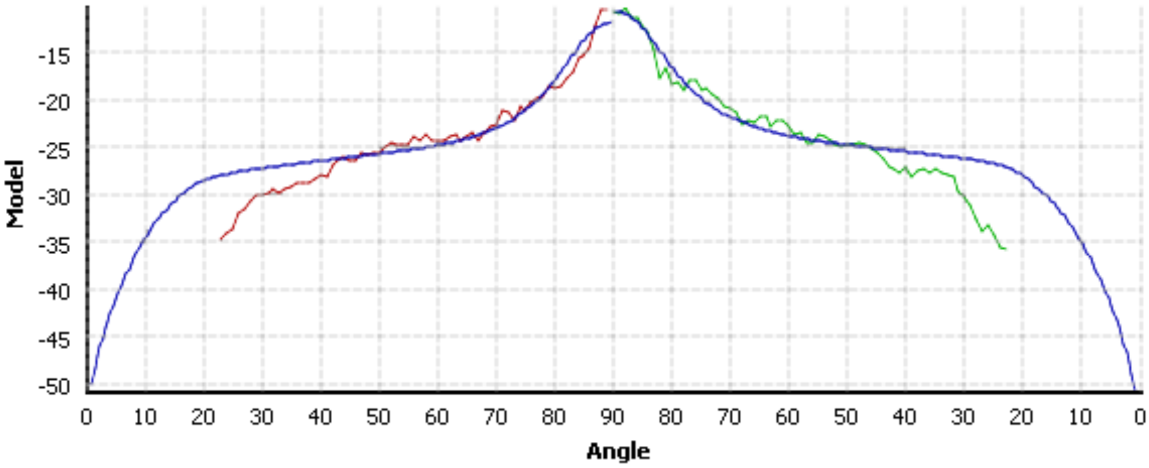

Figure B10: Beam pattern for muddy sand sediment generated with QPS Fledermaus Geocoder 7.3.6. Blue curve: modeled response, red/green curve: measured response.

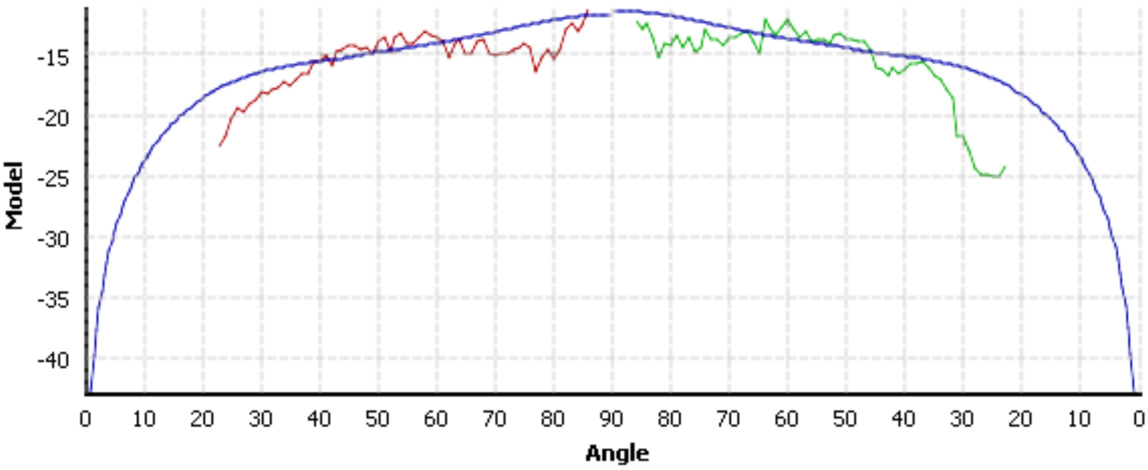

Figure B11: Beam pattern for gravel sediment generated with QPS Fledermaus Geocoder 7.3.6. Blue curve: modeled response, red/green curve: measured response.

Appendix C - Poster contribution EGU 2016, Vienna

Geophysical Research Abstracts
Vol. 18, EGU2016-9168, 2016
EGU General Assembly 2016

Hydroacoustic detection of dumped ammunition in the Ocean with multibeam snippet backscatter analyses. A case study from the 'Kolberger Heide' ammunition dump site (Baltic Sea, Germany)

Tina Kunde (1) and Jens Schneider von Deimling (2)

(1) Hafen City University, Geomatics, Hamburg, Germany (tina.kunde@hcu-hamburg.de), (2) Christian-Albrechts-University, Institute of Geosciences, Geophysics, Kiel, Germany (jschneider@geophysik.uni-kiel.de)

Dumped ammunition in the sea is a matter of great concern in terms of safe navigation and environmental threads. Because corrosion of the dumped ammunition's hull is ongoing, future contamination of the ambient water by their toxic interior is likely to occur. The location of such dump sites is approximately known from historical research and ship log book analyses. Subsequent remote sensing of ammunition dumping sites (e.g. mines) on the seafloor is preferentially performed with hydro-acoustic methods such as high resolution towed side scan or by the sophisticated synthetic aperture sonar approach with autonomous underwater vehicles. However, these are time consuming and expensive procedures, while determining the precise position of individual mines remains a challenging task. To mitigate these shortcomings we suggest using ship-born high-frequency multibeam sonar in shallow water to address the task of mine detection and precise localization on the seabed. Multibeam sonar systems have improved their potential in regard to backscatter analyses significantly over the past years and nowadays present fast and accurate tools for shallow water surveying to (1) detect mines in multibeam snippet backscatter data (2) determine their precise location with high accuracy intertial navigation systems.

A case study was performed at the prominent ammunition dumping site 'Kolberger Heide' (Baltic Sea, Germany) in the year 2014 using a modern hydro-acoustic multibeam echosounder system with 200-400 kHz (KONGSBERG EM2040c). With an average water depth of not even 20 m and the proximity to the shore line and dense waterways, this investigated area requires permanent navigational care. Previously, the study area was surveyed by the Navy with the very sophisticated HUGIN AUV equipped with a synthetic aperture sonar with best resolution by current technology. Following an evaluation of the collected data, various ammunition bodies on the sea floor could be clearly detected. Analyses of our shipborn multibeam snippet backscatter data now show the feasibility to detect the majority of such ammunition bodies by their distinct snippet backscatter anomaly and shape. By the use of SAPOS correction data, the navigation data of the appropriated multibeam echosounder was postprocessed, which leads to an absolute accuracy of the ammunition bodies of 0.1 m laterally. Thus, the multibeam dataset represents a study providing both, detection and precise positioning of individual mines on the seabed. Apart from the much greater efficiency of multibeam mapping sonar over towed sidescan, precise localization is important for future management of mines, may it be in regard to their dellaboration, or to evaluate if future sediment mass movement (sediment waves) may cover and obscure the ammunition bodies in the future.

Hydroacoustic detection of dumped ammunition in the Ocean with multibeam snippet backscatter analyses

A case study from the 'Kolberger Heide' ammunition dump site (Baltic Sea, Germany)

T. Kunde[1], Dr. J. Schneider v. Deimling[2], Prof. Dr.-Ing. H. Sternberg[1]
corresponding authors e-mail: tina.kunde@hcu-hamburg.de, jschneider@geophysik.uni-kiel.de, harald.sternberg@hcu-hamburg.de
----
[1] HafenCity Universität Hamburg, Geomatics | Hydrography, Überseeallee 16, 20457 Hamburg, Germany.
[2] Christian-Albrechts-Universität zu Kiel, Institute of Geosciences, Otto-Hahn-Platz 1, 24118 Kiel, Germany.

Introduction

- Ammunition bodies dumped in the oceans become problematic with regard to the environment and the economic development.
- Current methods require complex positioning solutions and suffer from improvable horizontal positioning accuracy.

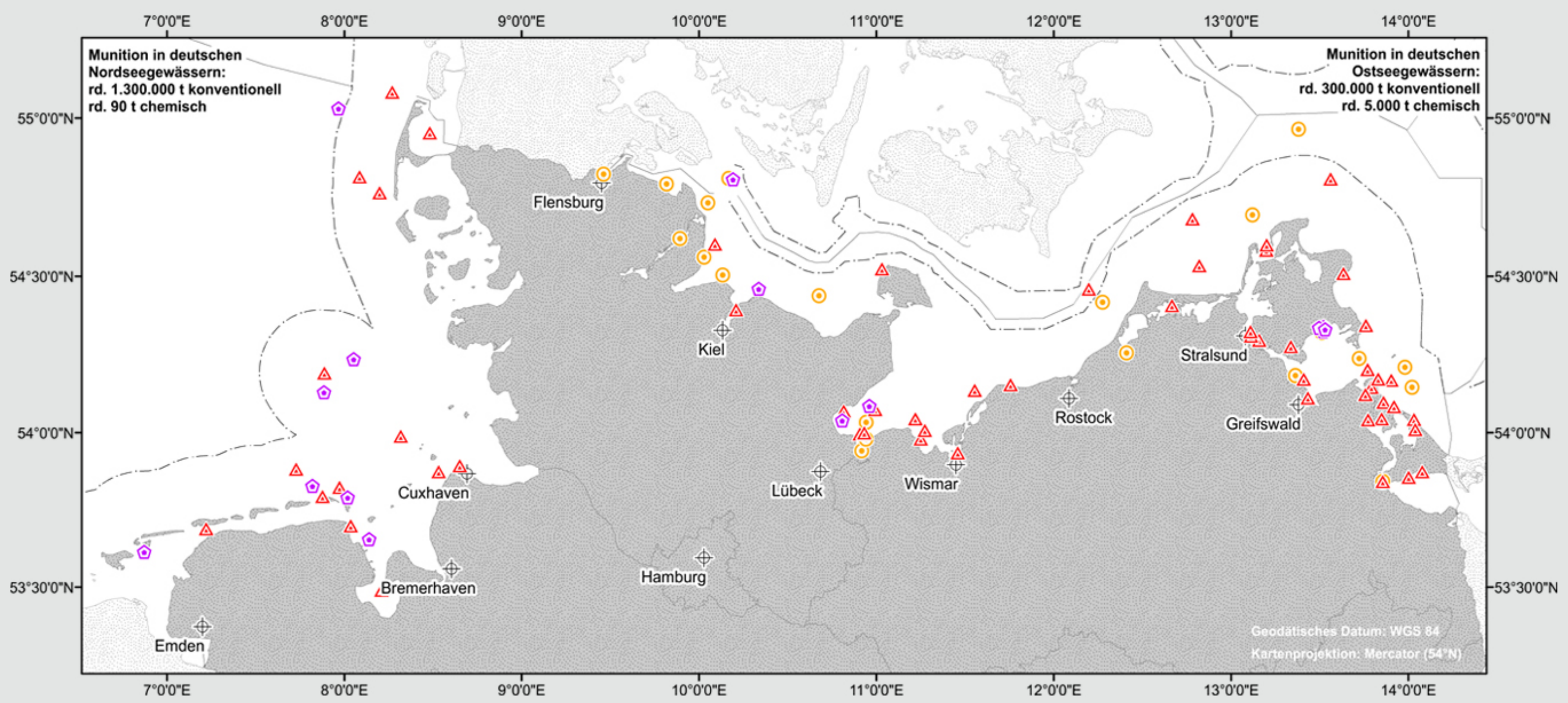

Fig. 1: Simplified overview of contaminated areas in German marine waters. Magenta pentagon: ammunition dump site, red triangle: contaminated area, yellow circle: potentially contaminated area. Continuous line: exclusive economic zone (EEZ), dotdashed line: territorial sea boundary. Geographical data provided by http://www.gadm.org (Böttcher et al., 2011: 10).

Motivation

- Pointing out a possibility to improve the lack of accuracy by using vessel-based survey equipment.
- Analysis of MBES snippet backscatter data due to their usability to detect ammunition bodies of different sizes.

Survey area

- Bay of Kiel, Baltic Sea (see Fig. 2)
- 4.5 km northeast of Schleswig-Holstein coastline
- Depth range: 5 m up to 18 m

- Conducted within the scope of cruise AL447
- Average survey speed: 4 kn

- Installed equipment:
  Kongsberg EM 2040C MBES
  Coda Octopus|NovAtel F180R INS
- MBES frequency|pulse length: 300 kHz|50 µs
- INS data rate: 100 Hz

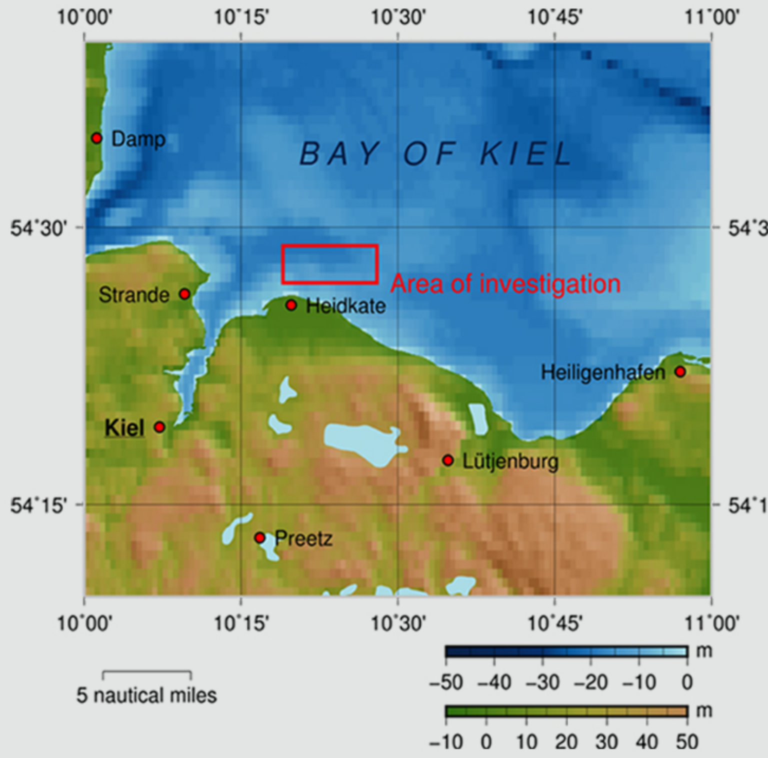

Fig. 2: Area of investigation in the Kiel Fjord. Mercator projection with global dataset GEBCO 2008 (30 arc-seconds), investigated area is highlighted in red.

Analysis of MBES snippet backscatter and INS positioning

- Utilized software: CARIS HIPS and SIPS 8.1 (Bathymetry), QPS Fledermaus Geocoder (Snippet backscatter), and Motion INSight (Positioning).
- Evaluated MBES bathymetry provides a horizontal total propagated uncertainty (TPU) of 0.40 m and vertical TPU of 0.15 m.
  → higher MBES backscatter image resolution due to snippet time series processing.

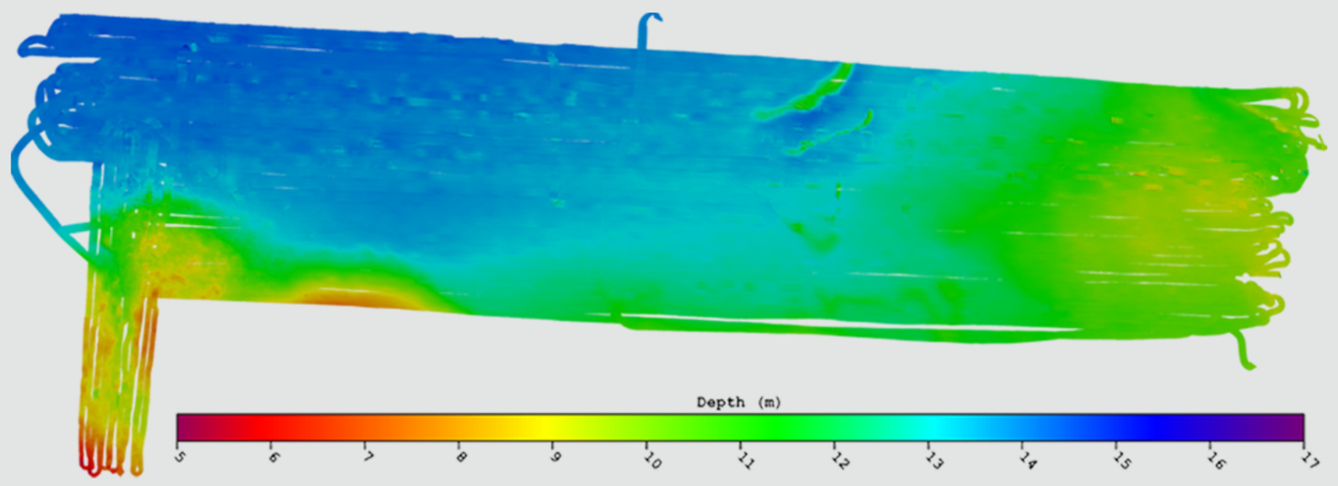

Fig. 3: Bathymetric data processed with CARIS HIPS and SIPS 8.1. Grid size: 0.40 m x 0.40 m according to the computed HzTPU.

Fig. 4: Snippet backscatter image processed with QPS Feldermaus Geocoder. Dark colors represent low backscatter intensities, light colors indicate high backscatter intensities. Values given in dB. Geographically referenced, mosaic pixel size: 0.50 m x 0.50 m.

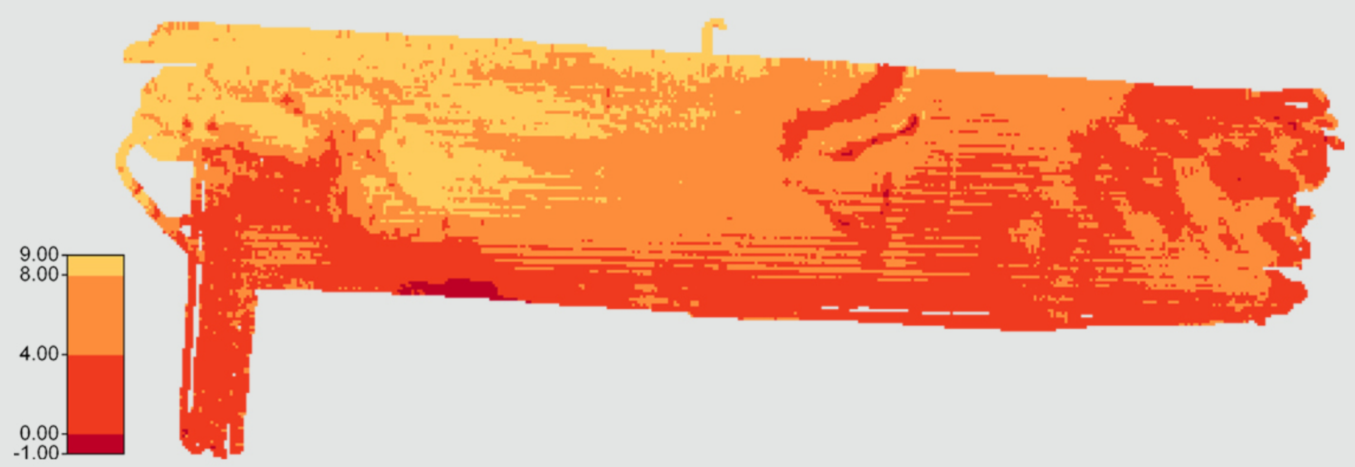

Fig. 5: Sediment variability based on angular range analysis (ARA) executed in QPS Fledermaus Geocoder. Values depict the mean grain size in phi units. Yellow area: clay, light orange area: silt, dark orange area: sand, red area: gravel. Underlaying grid size: 1.00 m x 1.00 m.

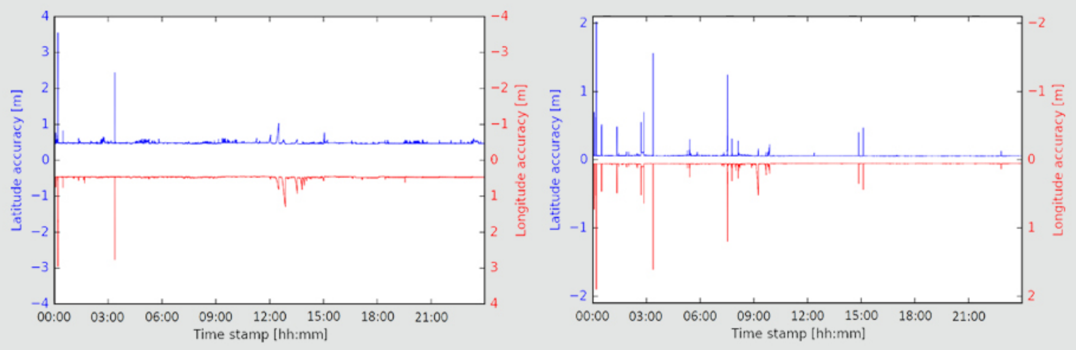

Fig. 6: Variability of position accuracy depending on the GNSS solution status. Exemplary consideration for November 02, 2014. Left: GNSS data without applied SAPOS® corrections (stand alone), latitude min. 0.45 m|max. 3.55 m, longitude min. 0.45 m|max. 2.96 m. Right: GNSS data with applied SAPOS® corrections (post-processed RTK), latitude min. 0.06 m|max. 2.02 m, longitude min. 0.05 m|max. 1.90 m.

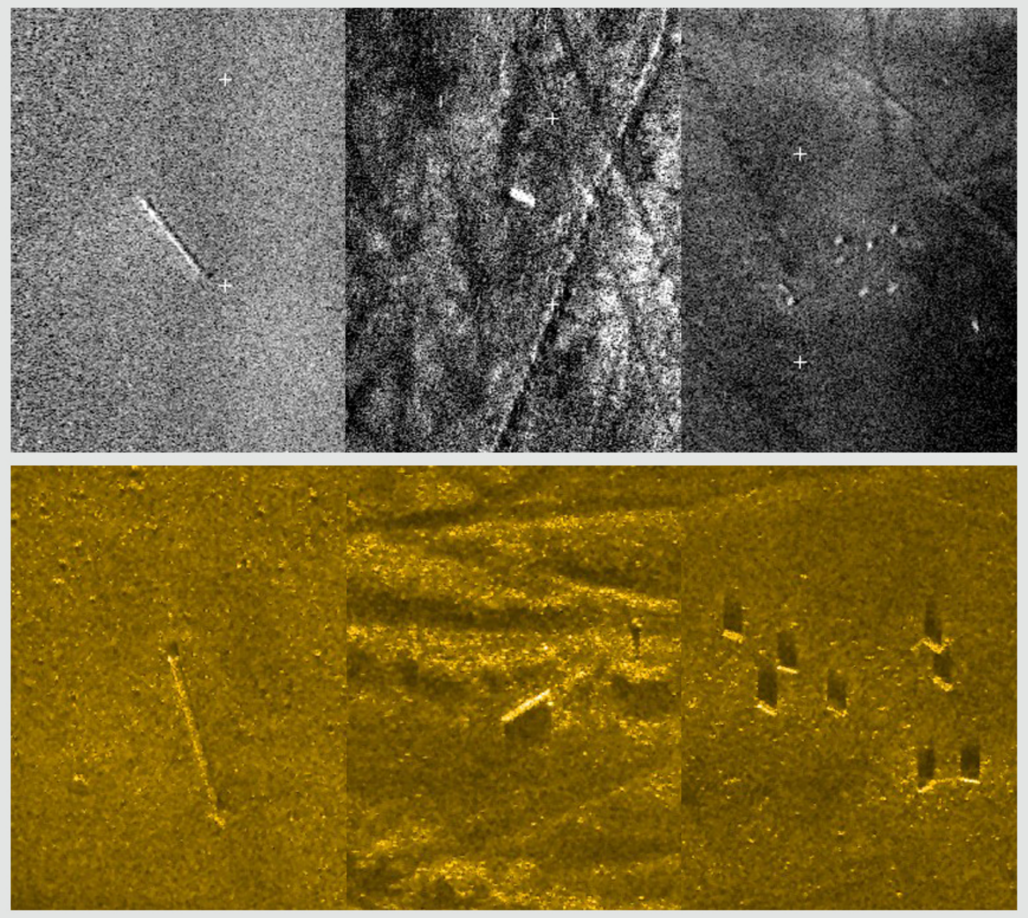

Fig. 7: Detected ammunition bodies on the seafloor. Top row: Screenshots of MBES snippet backscatter information during the data acquisition (not geographically referenced). Bottom row: Comparative sidescan sonar images taken from a database provided by the German Armed Forces. First column: Mine-like object dimensions: 6.7 m x 0.3 m. Position difference between snippet backscatter and database object: approx. 8.5 m. Second column: Poss ground mine dimensions: 2.1 m x 0.4 m. Position difference between snippet backscatter and database object approx. 22.5 m. Third column: Drums (dimensions unknown). Position difference between snippet backscatter and database object approx. 25.0 m (depending on chosen target reference).

Conclusion

- Dumped ammunition bodies of varying sizes can be localized in coastal waters using MBES snippet backscatter imagery information.
- Positioning accuracy in coastal waters is improvable up to 0.05 m using base station correction data as provided by the SAPOS® positioning service. Thus, potential transport of ammunition bodies by storm events with strong water currents can be detected by repeated MBES surveying.
- Evaluation of sediment composition can contribute to the modification of defusing strategies as burying of ammunition bodies caused by sediment transport may occur in future.
- Vessel-based survey systems are not adaptable with regard to the transducer depth, wherefore an increasing water depth will affect the imagery results.

References

Böttcher, C., Knobloch, T., Rühl, N.-P., Sternheim, J., Wichert, U., Wöhler, J., 2011: Munitionsbelastung der deutschen Meeresgewässer - Bestandsaufnahme und Empfehlungen. Sekretariat Bund/Länder-Messprogramm für die Meeresumwelt von Nord- und Ostsee (BLMP) (Hrsg.): Hamburg, 172 pp.

Schneider von Deimling, J., 2015: R/V ALKOR Cruise Report AL447. Controls on methane seepage in the Baltic Sea. GEOMAR Helmholtz Centre for Ocean Research: Kiel, 41 pp.

Dr. J. Schneider v. Deimling at ResearchGate:

Tina Kunde wurde für ihre Masterarbeit, die sie an der HafenCity Universität Hamburg verfasst hat, mit dem DHyG Student Excellence Award 2017 ausgezeichnet.

Die Arbeit zeigt auf, wie sich Munitionskörper am Meeresgrund mit Hilfe der Fächerecholot-Backscatter-Snippet-Technologie detektieren lassen. Wobei die Lage der Munitionskörper dank GNSS-Postprocessing und moderner Fächerecholottechnologie deutlich genauer als bisher angegeben werden kann.